Investigation of electronic fluctuations in semiconductor materials and devices through first-principles simulations and experiments in transistor amplifiers

Thesis by
Alexander Youngsoo Choi

In Partial Fulfillment of the Requirements for the
Degree of
Doctor of Philosophy

CALIFORNIA INSTITUTE OF TECHNOLOGY
Pasadena, California

2022
Defended December 10, 2021

© 2022

Alexander Youngsoo Choi
ORCID: 0000-0003-2006-168X

All rights reserved

ACKNOWLEDGEMENTS

First, I have to thank my advisor Professor Austin Minnich for his guidance and mentorship throughout my studies. I joined the Minnich lab in 2016, just as the group started branching out into new fields of study such as electronic noise. As a new student, I often felt intimidated by the scope of what I had to learn in order to conduct novel research in this new field. Throughout the entire learning process, Austin has been a constant source of academic support. Very few advisors are willing to commit the time to individual students that Austin did. Whenever I needed to discuss ideas, to go through derivations, or to develop my writing and presentations, his door was always open. I'm grateful for the opportunity to have worked and learned with him.

I also wish to extend my gratitude to the other members of my committee, Professors Melany Hunt, Guillaume Blanquart, and Anthony Readhead for their careful review and feedback on my research. Professors Hunt and Blanquart have been supportive and thoughtful mentors throughout my time at Caltech. I deeply admire their commitment to the promotion of diversity and inclusion at Caltech, and it was a great privilege to work with both of them on projects related to D&I during my time as a student. I must also thank Professor Readhead for generously hosting me in his lab; much of the research presented in this thesis would not have been possible without the support and resources of our collaboration.

Over the last five years, I have had the great privilege to collaborate with members of the Caltech and JPL radio astronomy community. I owe a special debt to Dr. Jacob Kooi and Dr. Sander Weinreb, who not only offered me the patient guidance of experienced engineers and academics, but also their friendship and moral support throughout my studies. Everything that I learned about being an engineer and an experimentalist, I learned from Jacob and Sandy. I am also extremely grateful to Dr. Kieran Cleary for his generosity as my host in the CRAL as well as his careful feedback on my work in group meetings and journal submissions. Special thanks are also due to Bekari Gabritchidze, who kept my spirits up with his support and friendship during our extensive time in the lab.

I am very grateful to have met and worked with many kind and talented people during my time at Caltech. I would like to thank Victoria Lee, Marcus Lee, Leah Ginsberg, Lynn Seymour, Carlos Portela, Professor Tim Colonius, Professor Melany Hunt, and

Dr. Hanna Song for all of your efforts during our time on the MCE Climate Survey committee. I would also like to thank my groupmates in the Minnich lab: Peishi Cheng, Adrian Tan, Erika Ye, Taeyong Kim, Benjamin Hatanpää, and Tomi Esho for their company and support throughout our studies. Special thanks to Peishi, Ben, and Tomi; it was a pleasure to learn and work closely with you on our various projects over the past few years.

While many people helped to make my research possible, I am especially grateful to those who made my time at Caltech enjoyable. Thank you to Leah Ginsberg, Joel Accorsi, Anna Pyzel, Peishi Cheng, Adrian Tan, Usama Choudhry, and Connor McMahan for your friendship. It's possible that we might have graduated faster had we never met, but it wouldn't have been nearly as much fun. To Rebecca, I cannot thank you enough for your love and support. It wasn't easy to pursue our graduate studies apart, but your companionship made it possible.

Finally, I reserve my deepest gratitude for my family, my siblings Christopher and Cosette, and to my mother and father, who have not only supported me throughout my life, but have also been my greatest role models.

This material is based upon work supported by the National Science Foundation under Grant No. 1911220.

ABSTRACT

Electronic noise, or stochasticity in the current, voltage, and frequency of a carrier signal is caused by microscopic fluctuations in the occupation of quantum electronic states. In the context of scientific instrumentation, understanding the physical origin of these fluctuations is of paramount importance since the associated stochasticity ultimately limits the fidelity of information transmitted through electronically processed-signals. The unifying theme of the work presented in this thesis is the study of electronic fluctuations in semiconductor materials and devices. Our interest in this topic is twofold. First, while the Nyquist law dictates the equivalence of noise and transport properties for systems in thermal equilibrium, this relationship breaks down for systems driven out of equilibrium by external forcing. Simulating non-equilibrium electronic fluctuations can therefore provide new insights into the microscopic processes that control energy and momentum relaxation which would not be available from conventional studies of transport alone. Furthermore, because noise properties are sensitive to the microscopic details of the bandstructure and scattering, *ab initio* simulations of noise observables provide a more rigorous test of the accepted theory of charge transport and carrier scattering in materials. Second, cryogenic low noise amplifiers based on high electron mobility transistors (HEMTs) are widely used in electromagnetic detector chains in applications such as radio astronomy, deep space communications, and quantum computing. The design and optimization of HEMT devices have conventionally relied upon empirical circuit-level models of fluctuations in devices. As the noise performance of modern low-noise amplifiers has saturated to levels five to ten times above the standard quantum limit, these empirical models are unable to resolve the microscopic origin of the limiting excess noise. Identifying the microscopic mechanisms underpinning noise in modern amplifiers is therefore necessary to produce better devices for scientific instrumentation. In this work, we investigate electronic noise in semiconductor materials and devices with a combination of first-principles simulations and Schottky thermometry experiments in transistor amplifiers.

First, we present our work on the development of novel parameter-free simulations of non-equilibrium noise in semiconductor materials. While the *ab initio* theory of low-field electronic transport properties such as carrier mobility is well-established, an equivalent treatment of electronic fluctuations about a non-equilibrium steady state has remained less explored. Starting from the Boltzmann Transport Equation,

we develop an *ab initio* method for hot electron noise in semiconductors. In contrast with the typical numerical methods used for electronic noise such as Monte Carlo techniques, no adjustable parameters are required in the present formalism with the electronic band structure and scattering rates calculated from first-principles. Our formalism enables a parameter-free approach to probe the microscopic transport processes that give rise to electronic noise in semiconductors. Next, we apply the developed method to compute the spectral noise power in two materials of technological interest, GaAs and Si. In our first study in GaAs, we show that despite the well-known dominance of optical phonon scattering, the spectral features in AC transport properties and noise originate from a surprising quasi-elasticity in the scattering of warm electrons with the lattice. In our second study, we apply the method to Si which possesses a more complicated multivalley conduction band. This study demonstrates that the widely-accepted one-phonon scattering approximation is insufficient to reproduce the warm electron tensor and that incorporating second-order mechanisms, such as two-phonon scattering, may be critical to obtain an accurate description of noise in such materials.

Finally, we discuss our work on developing deeper understandings of electronic noise in real devices with a focus on transistor amplifiers. While the first-principles work described above is appropriate for evaluating noise in ideal materials, in real semiconductor devices, charge carriers are influenced by mechanisms such as defect scattering, size effects, and reflections at interfaces. Owing to the complexity of these mechanisms, HEMT noise is typically treated with empirical models, where the physical noise sources are reduced to fitting parameters. Existing models of HEMT noise, such as the Pospieszalski model, are unable to resolve the mechanisms that set the noise floor of modern transistor amplifiers. In particular, the magnitude of the contribution of thermal noise from the gate at cryogenic temperatures remains unclear owing to a lack of experimental measurements of thermal resistance under these conditions. We report measurements of gate junction temperature and thermal resistance in a HEMT at cryogenic and room temperatures using a Schottky thermometry method. Based on our findings, we develop a phonon radiation model of heat transfer in the device and estimate that the thermal noise from the gate is several times larger than previously assumed. Our work suggests that self-heating results in a practical lower limit for the microwave noise figure of HEMTs at cryogenic temperatures.

PUBLISHED CONTENT AND CONTRIBUTIONS

1. **Choi[†], Alexander Y.**, Hatanpää[†], B., Cheng, P. S. & Minnich, A. J. Nonequilibrium transport and fluctuations of hot electrons in Si from first-principles. *In preparation.*

   Contributions A.Y.C. wrote the Python backend for Boltzmann Transport calculations, performed the initial set of calculations, performed data analysis, and wrote half the manuscript.

2. **Choi, Alexander Y.**, Esho, I., Gabritchidze, B., Kooi, J. & Minnich, A. J. Characterization of self-heating in cryogenic high electron mobility transistors using Schottky thermometry. *Journal of Applied Physics* **130.** https://doi.org/10.1063/5.0063331 (15 Oct. 2021).

   Contributions A.Y.C. built the experimental setup, performed all Schottky thermometry measurements, wrote the data analysis code, performed the data analysis, made the paper figures, and wrote the manuscript.

3. **Choi[†], Alexander Y.**, Cheng[†], P. S., Hatanpää, B. & Minnich, A. J. Electronic noise of warm electrons in semiconductors from first principles. *Phys. Rev. Materials* **5,** 044603. https://link.aps.org/doi/10.1103/PhysRevMaterials.5.04460 (4 Apr. 2021).

   Contributions A.Y.C. wrote the Python backend for Boltzmann Transport calculations, performed the data analysis, made the paper figures, and wrote a majority of the manuscript.

4. Esho, I., **Choi, Alexander Y.** & Minnich, A. J. Theory of drain noise in high electron mobility transistors based on real-space transfer. *In submission.* https://arxiv.org/abs/2108.03370 (2021).

   Contributions A.Y.C. contributed to discussion about the analysis and provided edits to the manuscript.

† These authors contributed equally to the work.

TABLE OF CONTENTS

Acknowledgements iii
Abstract v
Published Content and Contributions vii
Table of Contents vii
List of Illustrations ix
Chapter I: Introduction 1
1.1 *Ab initio* theory of non-equilibrium electronic fluctuations in semiconductor materials 2
1.2 Experimental characterization of thermal noise in HEMT amplifiers . 8
1.3 Outline of thesis 12
Chapter II: *Ab initio* theory of electronic fluctuations in semiconductors . . . 13
2.1 Background 14
2.2 The Boltzmann Transport Equation 18
2.3 Calculating steady-state transport observables with the BTE 19
2.4 Calculating fluctuations about a non-equilibrium steady state with the BTE 25
2.5 Numerical implementation of simulations 29
Chapter III: First-principles simulations of nonequilibrium electronic fluctuations in Gallium Arsenide and Silicon 33
3.1 Electronic transport in GaAs 34
3.2 Diffusion noise in GaAs 39
3.3 Spectral noise power in GaAs 46
3.4 Quasi-elastic scattering in GaAs 49
3.5 Hot electron phenomena in multivalley semiconductors 53
3.6 Electronic transport and fluctuations in Si 54
3.7 Summary of simulations 64
Chapter IV: Characterization of self-heating in cryogenic high electron mobility transistors using Schottky thermometry 65
4.1 Background 66
4.2 Schottky Thermometry technique 70
4.3 Sample and method specification 73
4.4 Schottky *I*-*V* measurements 75
4.5 Qualitative modeling of *I*-*V* characteristics 78
4.6 Junction temperature extraction 80
4.7 Phonon radiation resistance 82
4.8 Phonon radiation at the low noise operating point 87
Chapter V: Summary and outlook 94
5.1 Future work 95
Bibliography 98

LIST OF ILLUSTRATIONS

Number *Page*

1.1 Representative schematic of the spectral density of current fluctuations. The equilibrium spectral density (dashed line) contains only the information provided by specification of the Ohmic conductivity of the material. In contrast, the structures observed in the non-equilibrium spectrum (solid line) represent the relaxation rates of various microscopic processes such as generation and recombination, electron-phonon velocity fluctuations, intervalley fluctuations, and flicker fluctuations. The non-equilibrium spectral density provides information about the timescales and magnitudes of non-equilibrium processes not available from low-field transport quantities. Figure adapted from [35]. 6

1.2 Macroscopic electronic noise is underpinned by microscopic scattering events between electrons and impurities, phonons, and other electrons. Modeling electronic noise requires modeling microscopic scattering events. In this work, we provide special emphasis on electron-phonon interactions (EPIs). 7

1.3 Noise temperature versus frequency of various state of the art technologies [47, 55–63]. The best modern devices have noise temperatures 3-5 times the standard quantum limit. Several mechanisms have been proposed to set the practical noise floor including suppressed shot noise, excess gate leakage, and self-heating. Chapter 4 will cover our work on assessing the contribution of thermal fluctuations in the gate to the noise figure of modern HEMT amlifiers. Image credit: Iretomiwa Esho. 9

2.1 The original derivation of Nyquist's Law is a thought experiment utilizing three lumped element circuit models [6]. By combining Circuits I and II with the Second Law of Thermodynamics, Nyquist inferred that the equilibrium thermal noise power is a universal function of temperature, resistance, and frequency. By applying the classical equipartition theorem to Circuit III, Nyquist derived the specific form of the noise power for a single resistive element. 15

2.2 The scattering matrix used in this thesis is a lowest-order expansion of the electron phonon interaction in solids and therefore accounts for the simplest form of e-ph scattering, that mediated by the emission (1e) or absorption (1a) of a single phonon with momentum **q**. Higher-order perturbation expansions are needed to capture phenomena such as two-phonon (2ph), which include one emission, one absorption (1e1a), two absorption (2a) and two emission (2e) transitions. Calculations of two-phonon processes are computationally challenging owing to the larger phase space, as the intermediate states in the transition are not confined to the bandstructure. Figure adapted from Ref. [93]. 21

2.3 The central difference scheme used to approximate the momentum derivative in Eqn. 2.8 relates the local derivative to the value of the distribution in the nearest neighbor states. The dashed lines represent the distance vector **b**. The central difference approximation enables us move beyond the typical "cold-electron" approximation and treat electrons that have been heated above the lattice temperature. 23

2.4 Ratio of the non-equilibrium drift operator to the equilibrium drift operator for GaAs at 300 K. The cold-electron approximation is appropriate in the range of fields for which the ratio of the operators is much smaller than one. At even modest fields such as 800 $\mathrm{V\,cm^{-1}}$, the non-equilibrium drift operator rapidly exceeds its value in equilibrium, necessitating the warm electron-treatment applied here. 31

3.1 Conduction and valence band structure of GaAs with the $F\bar{4}3m$[216] Hermann Mauguin space group. **Inset:** Conventional cell of GaAs in the zincblende structure. Data generated with the Materials Project [144]. 35

3.2 Deviational occupation Δf_k in GaAs at 300 K under the cold (dotted lines) and warm (solid lines) electron approximations versus longitudinal wave vector k_x. Curves plotted for $\mathcal{E}$ = 100 $\mathrm{V\,cm^{-1}}$ (blue), and $\mathcal{E}$ = 800 $\mathrm{V\,cm^{-1}}$ (orange). The dashed black line is a guide to the eye. At the lower field, the two approximations result in nearly identical distribution functions. At the higher field, the cold-electron approximation fails to capture the assymetrical development of the distribution function. 36

3.3 Normalized longitudinal (||) DC mobility versus electric field of the cold (dashed blue line) and warm electrons (solid red line). The heating of the electrons leads to a decreased mobility. The trend of the normalized mobility agrees well with experiments: Figure 1, Ref. [146] (Upward black triangles) and Figure 4, Ref. [147] (Downward black triangles). 37
3.4 Real part of the longitudinal small-signal AC mobility versus frequency for equilibrium (dashed black line), $\mathcal{E}$ = 100 V cm^{-1} (dash-dot blue line), and $\mathcal{E}$ = 800 V cm^{-1} (solid orange line) under the warm electron approximation. The AC mobility exhibits spectral features at frequencies that are characteristic of the inverse momentum and energy relaxation times (see Section 3.3). 38
3.5 Spectral density of longitudinal current density fluctuations (solid red line) normalized to the Nyquist value versus electric field along with Davydov spectral densities calculated using an acoustic deformation potential (ADP) (dash-dot blue line) and Fröhlich (dashed yellow line). At equilibrium, the noise agrees with Nyquist-Johnson noise (dotted black line). The *ab initio* calculation predicts a steeper decrease in current PSD with field compared to the approximations. The symbols correspond to experimental measurements (Figure 11, Ref. [149]). 39
3.6 Relaxation time versus energy above conduction band minimum for GaAs at 300 K using ADP (dash-dot blue line), Fröhlich potential (dashed yellow line), and computed (red circles). The energy of the zone-center LO phonon is shown for reference (dashed black line). The qualitative agreement between the Fröhlich and computed first-principles relaxation times is an indication of the dominance of the LO phonon mode in GaAs at room temperature. 40
3.7 Effective electron gas temperature versus electric field for ADP (dash-dot blue line), Fröhlich (dashed yellow line), and computed (solid red line). The magnitude of electron heating is similar among the various calculations, indicating that heating alone cannot be responsible for the disparity in the power spectral density. 41

3.8 Kernel density estimate of the state-wise contribution to the (a) longitudinal and (b) transverse current spectral density as a function of the group velocity at equilibrium (blue volumes) and at 500 $\mathrm{V\,cm^{-1}}$ (red volumes). The noise contribution of each state is determined by the occupation and the magnitude of the induced fluctuation. The drift velocity in either the longitudinal or transverse directions are shown as dashed lines. 45

3.9 Computed power spectral density (PSD) of longitudinal ($\|$, dashed orange line) and transverse ($\perp$, dashed-dotted blue line) current density fluctuations versus frequency at $\mathcal{E} = 800\ \mathrm{V\,cm^{-1}}$, along with the Nyquist-Johnson prediction for $\mathcal{E} = 0$ (solid black line). In contrast to equilibrium, the non-equilibrium spectral densities exhibit an energy-dependent time scale that manifests as anisotropy between the longitudinal and transverse PSDs. 46

3.10 Spectral density of energy fluctuations versus frequency at equilibrium (solid black line), $\mathcal{E} = 800\ \mathrm{V\,cm^{-1}}$ (dashed orange line). The time scale for electron temperature fluctuations sets the upper frequency limit for the convective mechanism. 47

3.11 Probability histograms of longitudinal momentum loss $R_{\mathbf{k}}$ (blue bars) and energy loss $R_{\epsilon_{\mathbf{k}}}$ (yellow bars) normalized by the thermal averages at 800 $\mathrm{V\,cm^{-1}}$. The dashed lines represent the average transfer per scattering event. At this field, the average fractional dissipation of longitudinal momentum is $\sim 3\times$ larger than that for energy. 49

3.12 Deviational occupation $\Delta f_{\mathbf{k}}$ in GaAs at 300 K versus energy calculated under the RTA (dashed black line), hot Maxwell-Boltzmann (dashed-dotted grey line), and *ab initio* warm electron approximation (solid orange line) at 800 $\mathrm{V\,cm^{-1}}$. The dashed black line is added as a guide to the eye. Neither the RTA nor the Maxwell-Boltzmann capture the hot electron tail. 50

3.13 Valley structure of the conduction band minima of (a) GaAs and (b) Si plotted in Cartesian momentm space coordinates. Color indicates state energy above the conduction band minimum. While GaAs is characterized by a single spherical band at the Γ point, Si possesses six equivalent ellipsoidal bands in the ⟨100⟩. When Si is heated by an electric field, the redistribution of electrons among the six valleys causes anisotropy in macroscopic observables such as the electrical conductivity and power spectral density. 53

3.14 Population of individual valleys for Si versus electric field. When field is applied in the ⟨111⟩ direction, valleys are equivalent and population in each remains constant with field. In contrast, for the inequivalent ⟨100⟩ case, two cold valleys longitudinal to ⟨100⟩ form with increased population, and four hot valleys with decreased population from equilibrium. 55

3.15 Equivalent electron temperature calculated for each valley type for electric field applied in the ⟨100⟩ (solid lines) and ⟨111⟩ (dashed black line). When the field is applied along the high symmetry direction, all valleys remain equivalent and heat at a rate proportional to the inverse of the mean effective mass. On the other hand, when the field is applied along ⟨100⟩ heating in the four transversely oriented valleys at ⟨010⟩ and ⟨001⟩ is more efficient due to the lower effective mass while the heating in the two heavy longitudinally oriented valleys is less efficient. 56

3.16 Drift velocity versus electric field for the cases of the field applied in both the ⟨111⟩ and ⟨100⟩ directions. Election redistribution into the cold valleys with lower mobility causes a lower drift velocity at high fields in the ⟨100⟩ case. The symbols correspond to experimental measurements (Figure 6(a), Ref. [161]). 57

3.17 Computed (black solid line) current non-parallelism ratio tan ϵ versus electric field strength at $\theta = 23°$. The simulated non-parallelism is in excellent agreement with reported measurements of Ref. [164] in n-Si (red triangles), indicating accurate calculation of anisotropy in the bandstructure. **Inset**: A common experimental technique to quantify the anisotropy of the conductivity is to sweep the orientation of the electric field θ with respect to ⟨100⟩ in the (110) plane and to measure the non-parallelism angle ϵ. 59

3.18 Simulated longitudinal mobility as a function of electric field strength along the ⟨100⟩ (solid blue line) and ⟨111⟩ (solid red line) axes along with the fitted warm-electron model of Eqn. 3.11 for β. The β component of the warm electron tensor describes the rate at which the mobility changes with the applied field, and is a macroscopic descriptor of the energy exchange between charge carriers and the lattice. 60
3.19 Simulated anisotropy of β (black solid line) as a function of the field orientation in the (110) plane θ. Although the widely accepted 1-phonon scattering theory in n-Si is capable of reasonable qualitative fitting of the velocity-field curve shown in Fig. 3.16, the simulated β at all orientations is about twice as large as that reported in measurements [166] (red triangles), suggesting that the present theory is not accurately describing energy relaxation in Si. 61
3.20 Simulated longitudinal current density fluctuations in Si at 300 K along the ⟨100⟩ (solid blue line) and ⟨100⟩ (solid orange line) axes, normalized to the Nyquist value as a function of electric field. The symbols correspond to experimental measurements (Figure 4, Ref. [167]). 62
4.1 Representative energy band diagrams of n-channel metal oxide semiconductor field effect transistor (MOSFET) and high electron mobility tranistor (HEMT). In a n-MOSFET, when sufficiently high bias applied to the metal gate, holes are forced away from the interface and a thin inversion layer of electrons serves as the conducting channel of the device. In contrast, in HEMTs, the conducting channel is formed from the 2DEG produced at the heterojucntion of two semiconductors, one wide and the other narrow bandgap. 67
4.2 Pospieszalski FET noise model. The extrinsic parasitic elements (blue) such as the gate, source, and drain pad resistances as well as the various capacitances are typically removed via a de-embedding procedure. Noise in the intrinsic device (black) is disaggregated into a thermal source added at the gate input and a hot electron source added at the channel output. 69

4.3 Extracted base temperature dependence (solid lines) for (a) the ideality factor and (b) the saturation current of a typical HEMT gate Schottky diode from cryogenic to room temperature. The fitted model shows excellent agreement with the measured ideality factor and saturation current (markers) across the entire temperature range. The uncertainty of the extracted quantities is sufficiently small that error bars are not visible. 71

4.4 Microscope images of probe station instrumentation. (a) Stage of the cryogenic probe station used for DC and S Par measurements of the cryogenic HEMTs. (1) Brass mounting chuck (2) Lakeshore heater resistor (3) Lakeshore temperature sensor (4) CPW to coaxial gate probe (5) CPW to coaxial drain probe (6) coaxial thermal strap. (b) Magnified view of HEMT chip during probing. (7) gate pad (8) drain pad (9) common source pads. Scalebars correspond to 10 mm (left) and 100 μm (right). 73

4.5 Schematic of cryogenic probe station setup for Schottky thermometry measurements. (1) WR-10 style coplanar-waveguide probes (2) internal SMA coaxial transmission lines (3) direct current transmission lines (4) external SMA coaxial transmission lines. Figure adapted from Ref. [199]. 74

4.6 Measured forward I-V characteristics of the HEMT at different base temperatures (colored symbols). We fit the temperature-dependence of the Schottky parameters for $I \lesssim 100$ μA for which $T_j \approx T$ and the diode characteristics are log-linear. The DC resistance is combined with S-parameter measurements to extract the junction temperature at the 0.5-9 mA biases for which self-heating occurs. Uncertainties in the measurements are sufficiently small that error bars are not visible. 75

4.7 Small-signal reflection coefficient extracted from S-parameters at different bias points (colored markers) and $T = 20$ K from 1-10 GHz. The small-signal resistance is extracted by taking the real part of the input impedance. 76

4.8 Small signal resistance extracted from S-parameters at different bias points (colored markers) and $T = 20$ K from 1-10 GHz. At low bias and high frequencies, the effect of the parasitic gate-source capacitance becomes apparent and the resistance drops off. To avoid this effect, the resistance is extracted only below 1 GHz where the capacitance is negligible. Uncertaintities in the measurement are sufficiently small that error bars are not visible. 77
4.9 Measured I-V characteristics at **(a)** 300 K and **(b)** 20 K (red markers) compared to the ideal diode (black dashed line), cold diode (blue dashed dotted line), and linear-heating model (orange solid line). The cold-diode model captures the data well at low biases under 1 mA. A calculation assuming constant thermal resistance explains the high-bias measurements above 1 mA at 300 K but not at 20 K, implying the dominance of a different heat transfer mechanism at cryogenic temperatures. See text for additional details. The curves for cold diode model and linear heating model coincide with the ideal diode model below 0.5 mA and are omitted for clarity. 79
4.10 Junction temperature rise, $T_j - T$, versus dissipated power density at base temperatures 20 K (red circles), 40 K (yellow triangles), 60 K (blue triangles), and 300 K (black squares). The temperature rise is approximately linear with power at room temperature but nonlinear at cryogenic temperatures. Dashed black lines are added as guides to the eye. 80
4.11 Interpolated junction temperature, T_j versus base temperatures, T at various power densities (colored lines). As the device is cooled, the junction temperature begins to plateau due to self-heating. 81

4.12 Thermal resistance of the junction versus power density at base temperatures of 20 K (red circles), 40 K (yellow triangles), 60 K (blue triangles), and 300 K (black squares). At room temperature, the thermal resistance is nearly independent of power and thus junction temperature. At cryogenic temperatures, the thermal resistance increases nonlinearly as the power and junction temperature decrease. While diffusion theory is not able to explain these trends, the features of the measurement are qualitatively consistent with the predictions of a simple model assuming the thermal resistance is dominated by phonon radiation through the interface (computed at 20 K, red solid line). Dashed black lines are added as guides to the eye. 84

4.13 Equivalent thermal circuit model of the cryogenic HEMT at the low noise operating point. Under the phonon blackbody regime, the source, gate, and channel are linked by radiation space resistances. Under the appropriate approximations, this circuit can be solved for the gate and channel temperatures as a function of channel dissipation and substrate temperature. 88

4.14 For a given substrate temperature and channel dissipation, the radiation circuit is solved for the gate and channel temperatures, here plotted as temperature increase relative to the substrate. At high substrate temperatures > 50 K, the temperature rise at all biases is a small fraction of the substrate temperature. However at liquid helium temperatures, the temperature rise at even small biases may be several times the substrate temperature. For typical HEMT parameters, the temperature rise in the gate is approximately 2/3 of that in the channel. 89

4.15 The simulated gate temperature under low noise bias conditions for the typical HEMT geometry. At high temperatures > 50 K, decreasing the substrate temperature by 1 K produces almost an equivalent decrease in the gate thermal noise. However as the substrate temperature continues to decrease, the gate becomes thermally decoupled from the substrate. At liquid helium temperatures, the thermal noise from the gate may be several times larger than that predicted by the substrate temperature. 90

4.16 The simulated dependence of the Pospieszalski minimum noise temperature T_{min} on the gate temperature of the amplifier at substrate temperature 100 mK. Linear transistor model available from OMMIC D007IH PDK. Small-signal transistor elements obtained from [198]. Improvements in thermal management will be necessary to reduce the contribution of the gate to the minimum noise temperature of the transistor. 92

Chapter 1

INTRODUCTION

Information in an electronic signal is contained in variables such as current, voltage, or frequency. The processing and detection of arbitrarily small electronic signals is limited by the loss-of-information induced by electronic noise, observed as irregular and spontaneous deviations in the current, voltage, or frequency of the carrier signal. In the context of scientific instrumentation, noise is of paramount interest because it sets the practically achievable lower limit for accuracy of any electronically processed measurement [1]. The unifying theme of the work presented in this thesis is the study of electronic fluctuations in semiconductor materials and devices. Our interest in this topic is guided by two observations.

First, while fluctuations of an equilibrium system are completely specified by the temperature and conductivity, this description is insufficient in hot electron systems, in which charge carriers are driven from equilibrium by external forces. When perturbed by forces such as an electric field, electrons heat to high energy states and access new scattering mechanisms unavailable in equilibrium. Fluctuations about this non-equilibrium state are uniquely sensitive to the material-specific band-structure and the momentum and energy relaxation induced by various scattering mechanisms. Consequently, studying hot electron noise characteristics such as the current spectral density can provide new insights into charge transport and offers a more rigorous test of the underlying physical theory than conventional studies of low-field transport coefficients.

Second, we note that the design and optimization of important weak-sensing devices, such as the transistor amplifiers commonly used in electromagnetic detectors, is dominated by simple circuit models of electronic noise. Despite the remarkable progress driven by empirical optimization in the past three decades, the noise performance of these devices has saturated to a level five to ten times above the quantum limit [2]. The development of more physically-motivated models for device noise is needed to stimulate progress and improve weak-sensing scientific instrumentation. In this thesis, we seek to contribute to a deeper fundamental and practical understanding of electronic noise through both simulations of fluctuations in semiconductors and experimental characterization of thermal noise in transistor amplifiers.

1.1 *Ab initio* theory of non-equilibrium electronic fluctuations in semiconductor materials

The transport and fluctuation properties of a given semiconductor material can be calculated with knowledge of the electronic bandstructure and the interactions of charge carriers with phonons, impurities, and other electrons. At a microscopic level, individual electronic states are characterized by state properties such as energy, group velocity, and the scattering rates with other states. If the distribution of electrons, subject to external influence, is known, averaging these state quantities over the distribution yields useful physical quantities such as the carrier temperature, optical absorption, and electrical conductivity [3].

For systems in thermal equilibrium, the Fermi-Dirac distribution f_λ describes the occupation of charge carriers in a given state λ. The Fermi-Dirac distribution only specifies the mean occupation of the electronic state. At finite temperatures, the instantaneous occupation of a given state spontaneously fluctuates around the average value specified by Fermi-Dirac. Microscopically, these fluctuations arise because of the stochastic nature of the scattering. In equilibrium, detailed balance requires that the mean flux of particles into every quantum state is zero. However, the flux of particles into or out of a quantum state is a Poissonian process and is characterized by a variance. Therefore, the instantaneous net flux into a quantum state is in general non-zero due to instantaneous imbalance between the incoming and outgoing fluxes [4]. Consequently, the occupancy of quantum states fluctuates under both equilibrium and non-equilibrium conditions. These occupation fluctuations are the microscopic underpinning for what we observe macroscopically as electronic noise — the stochastic variation of the current or voltage in an electronic signal.

A non-random characteristic of these fluctuations is the power spectral density (PSD) of current fluctuations, which, by the Wiener-Khintchine Theorem, is related to the single-sided Fourier transform of the autocorrelation of the current fluctuations [5]. For systems in thermal equilibrium, simple analytical expressions relate the current PSD to the small-signal response of the system to external perturbations. In a system of charge carriers, the prototypical example is the Nyquist Law, which states that the spectral density of thermal current fluctuations at equilibrium is proportional to the small signal conductivity of the material and the temperature [6]. The Nyquist law is a specific application of the more general fluctuation dissipation theorems, first outlined by Callen and Welton [7] and subsequently expanded by Kubo [8, 9] and Lax [10] that provide the analytical link between the spectral noise power and

the admittance of the system. Other famous realizations of fluctuation dissipation theorems include the theory of Brownian motion [11] and Kirchoff's law of thermal radiation [12]. Conceptually, these theorems reflect a naturally intuitive concept: particles in an equilibrium system that are excited by either nonrandom perturbations or spontaneous fluctuations relax to equilibrium via the same kinetic mechanisms, and consequently it is sensible that the response in both cases should be related.

Outside of equilibrium, the fluctuation dissipation theorems are no longer valid, and the noise spectral density is no longer specified by the low-field conductivity and temperature [13]. On one hand, this fact makes the calculation of non-equilibrium noise difficult, since the noise power spectral density and the linear transport properties must be solved for separately. On the other hand, it means that simulating noise characteristics such as the current PSD can provide new insights into the microscopic processes that set energy and momentum relaxation in materials, which could not be obtained from the study of low-field transport alone.

Electron-phonon interactions from first-principles

One topic of particular interest is the study of how charge carriers in a semiconductor interact with the lattice. Electron-phonon interactions (EPIs) underpin many important phenomena such as the temperature dependence of carrier mobility, the optical absorbance of indirect-gap semiconductors, and the formation of Cooper pairs in conventional superconductors [14]. Early computational studies of EPIs relied heavily on semi-empirical descriptions of the interaction [15–17]. Deformation potential theory, first developed in systems with isotropic bandstructures by Shockley and Bardeen [18] and later generalized to anisotropic systems by Herring and Vogt [19] provided a reasonable fit to empirical data but could not predict the behavior of either novel materials or materials under conditions which had not been experimentally tested. Despite these limitations, the simplicity of the semi-empirical approach and the lack of more sophisticated alternatives left deformation potential theory as the dominant means of calculating EPIs for nearly two decades.

The development of truly predictive simulations of EPIs began with the advent of *ab initio* methods to calculate electronic wavefunctions, lattice dynamical properties, and electron-phonon (e-ph) matrix elements. These methods are known as *ab initio* because they can be executed without the use of *ad-hoc* parameters and in principle require only the specification of atomic identities and locations [20]. A major breakthrough in such first-principles methods was the development of Kohn-Sham

density functional theory (DFT) [21]. Under this method, the numerically intractable many-body Schrödinger equation for a coupled electronic system is simplified via a mean-field approach to a set of Kohn-Sham equations of polynomial complexity [22]. With the appropriate selection of exchange-correlation functional, the Kohn-Sham equations can provide a description of the ground-state electronic system in the form of electronic wavefunctions and charge density [23]. In parallel to developments in DFT, methods to calculate lattice vibrations from first-principles were formalized. Density functional perturbation theory (DFPT), first developed by Baroni and coauthors in 1987 [24], provided a method to calculate phonon dispersions and perturbation potentials of the phonons on the electronic system.

Individually, DFT and DFPT can provide descriptions of the ground-state electronic and equilibrium lattice properties of the system. However, when combined, the methods can also be used to calculate perturbed-system dynamics such as transport and fluctuations [14]. The basis of such calculations is the Fermi Golden Rule (FGR), which specifies the transition rates between the Kohn-Sham electronic eigenstates mediated by phonons in terms of the DFPT perturbation potentials [25]. Practically, the FGR provides a framework to calculate electronic scattering rates [26]. These transition rates can then be used to computationally simulate linear response charge transport and fluctuations properties in the electronic system.

In principle, if the scattering interactions between electronic states are specified, it is possible to trace the trajectories of each charge carrier in the system as is done in molecular dynamics. In practice, such an approach is not computationally feasible due to the large number of free carriers in even the most lightly doped semiconductors. Consequently the dynamics of charge carriers in semiconductors are usually described statistically, through the probability distribution function. As mentioned previously, charge carriers in an equilibrium state are distributed according to Fermi-Dirac statistics. The Boltzmann Transport Equation (BTE) is a framework that describes the statistics of *perturbed systems* through the non-equilibrium distribution function [27]. The BTE is an integro-differential equation that describes the evolution of the particle distribution function in time, position, and momenta in response to external perturbations such as a temperature gradient or an electric field and internal transitions described by the FGR [3]. Once solved, moments of the calculated distribution function can be performed over the Brillouin zone to give macroscopic properties such as particle number, drift velocity, and mean energy, and their variation in space and time.

In recent years, spurred by the development and distribution of first-principles electronic structure codes [28–30], various studies have developed methodologies to use the BTE with *ab initio* inputs from DFT and DFPT as a powerful tool for studying charge transport phenomena in semiconductor materials. These computational studies supplement experimental characterization in two important ways. First, while most experimental observables represent moments of the distribution function over the Brillouin zone, *ab initio* simulations give access to the microscopic properties and mechanisms that are difficult to access experimentally. The perspective obtained from first-principles descriptions of charge transport has significantly enhanced our understanding of the microscopic interactions that determine linear transport properties. Second, if reasonable agreement with experimental observables is obtained, these studies provide evidence that the implemented theory is an accurate characterization of the material. On the other hand, discrepancies with measurements can be used to identify missing mechanisms, which are subsequently incorporated into the first-principles simulation, iteratively contributing to a new accepted level of theory in the material. In well-studied materials such as GaAs and Si, the culmination of years of study have enabled predictive calculations of quantities such as the phonon-limited electrical conductivity [31, 32], Hall mobility [33], and electron mean free paths [34].

While the *ab initio* theory of low-field electronic transport properties in semiconductors is well-established, an equivalent treatment of hot electronic fluctuations in semiconductors is lacking. While existing low-field transport theory fully specifies the electronic noise in equilibrium systems via the Nyquist Law, for systems perturbed out of equilibrium, the Nyquist Law is invalid and the spectral noise power is no longer specified by the conductivity and temperature [13]. Consequently, simulating the hot electron noise power spectral density can provide new information about the timescales and magnitudes of non-equilibrium processes that would not be available from the calculation of mean transport quantities alone.

Physical interpretation of spectral noise power

As an example, consider Fig. 1.1, which is a pedagogical illustration of the spectral density of current fluctuations in a semiconductor material. When the system is in an equilibrium state, although there is no bulk current flow, stochastic thermal fluctuations in electron occupation manifest as electronic velocity fluctuations. In the figure, the velocity fluctuations appear as the Lorentzian structure observed in the equilibrium PSD, characterized by a single pole roll-off. The Nyquist Law specifies

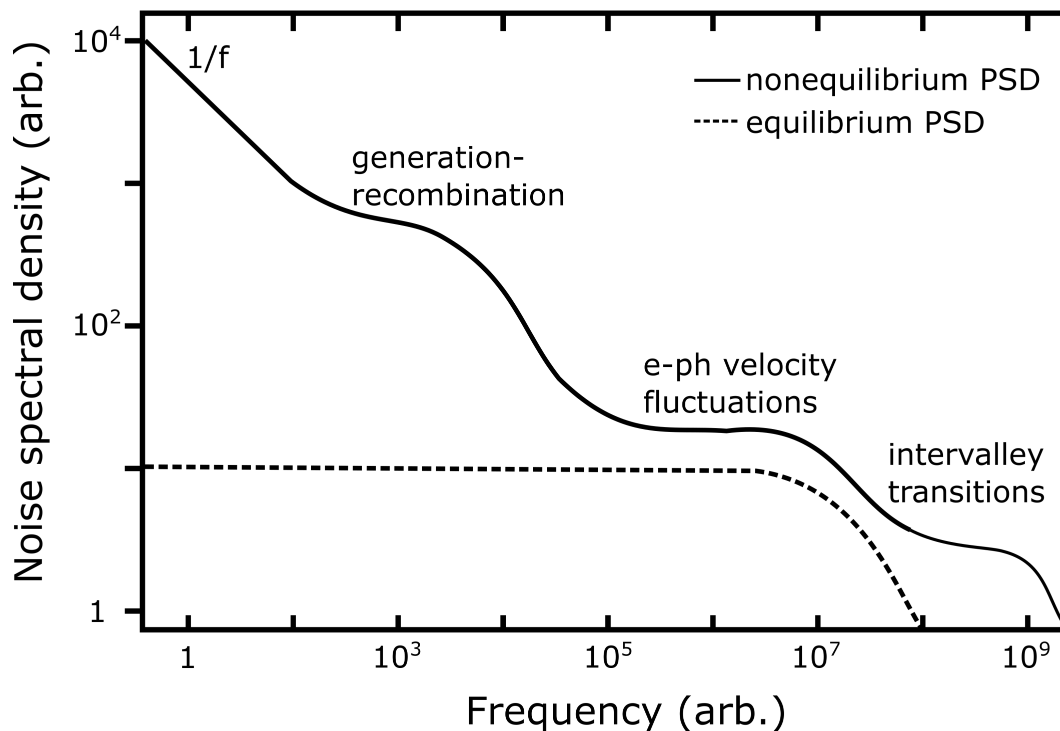

Figure 1.1: Representative schematic of the spectral density of current fluctuations. The equilibrium spectral density (dashed line) contains only the information provided by specification of the Ohmic conductivity of the material. In contrast, the structures observed in the non-equilibrium spectrum (solid line) represent the relaxation rates of various microscopic processes such as generation and recombination, electron-phonon velocity fluctuations, intervalley fluctuations, and flicker fluctuations. The non-equilibrium spectral density provides information about the timescales and magnitudes of non-equilibrium processes not available from low-field transport quantities. Figure adapted from [35].

that the spectral noise power is characterized by the same momentum relaxation time associated with the linear electrical mobility [36].

In contrast, outside of equilibrium, the PSD contains new spectral features associated with non-equilibrium random processes. As seen in Fig. 1.1, each distinct feature corresponds to a new noise mechanism such as $1/f$ [37], electronic transitions between inequivalent valleys [36], generation and recombination (G&R) processes [5], or hot electron-phonon mediated velocity fluctuations [38].

As can be seen in the figure, certain noise mechanisms only appear in the spectral density under non-equilibrium conditions. For example, the stochastic exchange of electrons between the conduction and valence bands via generation and recombination causes resistance fluctuations as the conductivity depends on the number of free

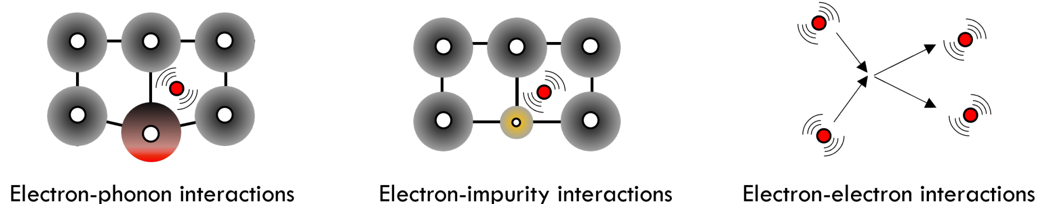

Figure 1.2: Macroscopic electronic noise is underpinned by microscopic scatttering events between electrons and impurities, phonons, and other electrons. Modeling electronic noise requires modeling microscopic scattering events. In this work, we provide special emphasis on electron-phonon interactions (EPIs).

electrons. When the system is in equilibrium, there is no current flow and consequently the G&R and fluctuations are not observed in the equilibrium current PSD. In contrast, when voltage is applied across the semiconductor, these fluctuations in resistance translate into current fluctuations which increase the noise spectral density relative to equilibrium. In addition to the magnitude, the generation and recombination noise is characterized by a timescale that corresponds to the relaxation rate of the G&R process. This example illustrates the value of fluctuation spectroscopy, where underlying microscopic processes are studied through their influence on the noise characteristics of a material. The timescales and relative magnitudes of each of these processes can be extracted quantitatively from the shape of the spectral density, allowing one to directly assess the contribution of different noise sources in a given frequency range. Because the nonequilibrium spectral density contains information about processes that are not observed in equilibrium, accurately simulating hot electron noise is a more rigorous test of the underlying theory of charge transport than the calculation of low-field transport quantities such as the linear conductivity.

In this thesis, we outline a Boltzmann Transport Equation framework for the first *ab initio* simulations of electronic noise in semiconductors. As seen in Fig. 1.1, many microscopic mechanisms may contribute to the hot electron noise spectrum of real materials. In many semiconductor materials, the relaxation time associated with e-ph scattering is on the order of hundreds of femtoseconds and consequently phonon-mediated fluctuations are typically dominant in microwave semiconductor devices [38]. In our work, we provide special focus on the non-equilibrium velocity fluctuations induced by one phonon-mediated scattering [39]. Our work represents an important contribution to the *ab initio* study of electron-phonon interactions. While conventional e-ph *ab initio* simulations are restricted to the "cold" regime,

where carriers are only lightly perturbed from equilibrium, we have extended the theory to enable simulation of hot carrier phenomena, where the electron temperature can greatly exceed the lattice temperature. The magnitude and spectral characteristics of the hot electron noise depends on the unique details of the bandstructure and the kinetic processes that set the rates of momentum and energy exchange with the lattice in the material. As a demonstration of our method, we compute the spectral noise power of electrons in two semiconductors of technological interest, GaAs and Si.

1.2 Experimental characterization of thermal noise in HEMT amplifiers

In the previous section, we discussed how studying electronic fluctuations can provide useful insight into fundamental microscopic processes in materials. A second objective of this thesis is to develop better understanding of how these fluctuations impact the development of real semiconductor devices, especially those used in weak-sensing applications. At present, *ab initio* methods are capable of simulating fluctuations in simple systems such as atomically pure, spatially homogeneous, semiconductor bars. These materials-level simulations will contribute to improved understanding of fundamental mechanisms that determine noise properties of commonly used materials. Furthermore, as recent examples in the transport community illustrate [40–42], the continued development of *ab initio* calculations may lead to experimental realization of new materials with novel noise properties.

On the other hand, simulating fluctuations in semiconductor devices is far more challenging since charge and heat carriers in real devices are influenced by complex mechanisms such as defect scattering [43], size effects [44], and reflections at interfaces [45]. Owing to these challenges, the design and optimization of many important semiconductor devices has been guided by simple equivalent circuit-level models of electronic noise such as the Pospieszalski model [46]. These models are limited in their ability to identify the microscopic sources of excess noise, as will be discussed in detail below.

In this thesis, we focus on the noise performance of semiconductor devices based on high electron mobility transistors or HEMTs. Microwave low noise amplifiers (LNAs) based on HEMTs are a cornerstone of high precision measurements across diverse fields in science and engineering such as radio astronomy [47, 48] and quantum computing [49–53]. In these sensitive measurements, a cryogenic microwave amplifier is often the first stage of the signal processing chain, and consequently

its noise performance sets the noise floor of the entire apparatus since the noise contributions of subsequent stages are reduced by the gain of the first stage. The noise performance of an amplifier is characterized by its noise temperature; the ultimate lower limit is set by quantum mechanics and is around 0.3 K at 6 GHz [54], a common frequency for microwave signal processing.

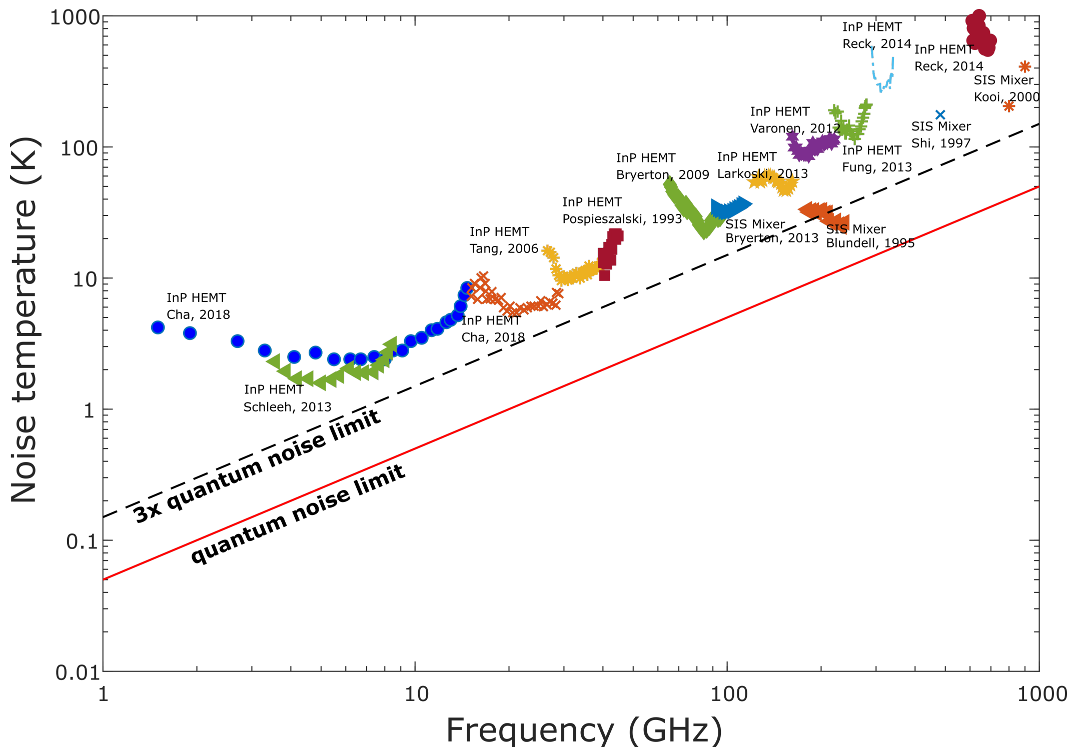

Figure 1.3: Noise temperature versus frequency of various state of the art technologies [47, 55–63]. The best modern devices have noise temperatures 3-5 times the standard quantum limit. Several mechanisms have been proposed to set the practical noise floor including suppressed shot noise, excess gate leakage, and self-heating. Chapter 4 will cover our work on assessing the contribution of thermal fluctuations in the gate to the noise figure of modern HEMT amlifiers. Image credit: Iretomiwa Esho.

After decades of development in device fabrication techniques [64–66] as well as optimization based on microwave circuit design [55, 60, 67–69], HEMT LNAs have achieved cryogenic noise temperatures approximately 5-10 times the quantum limit over frequencies from 1-100 GHz, as can be seen in Fig. 1.3. Despite this progress, applications drive the development of amplifiers with ever-lower noise figures [70]. Consequently, identifying the origins of excess noise in HEMTs is of great practical interest, as such understanding will enable the design of better devices.

Conventionally, the problem of minimizing noise in transistor amplifiers has been

approached through the development of equivalent circuit models. The Pospeiszalski FET model is the prototypical example for HEMTs [46]. Under this model, the noise of the intrinsic HEMT is decomposed into two sources, an input source added at the HEMT gate and an output source in the HEMT drain. The noise sources are parameterized by equivalent noise temperatures T_g and T_d, respectively. Physically, the drain source is often interpreted as related to hot electron fluctuations in the channel, while the gate noise is assumed to be a purely thermal source at the ambient temperature $T_g = T$ [71]. According to the Pospieszalski model, for a constant drain current, as the temperature of the device is reduced, the thermal noise contributed by the gate should scale as $\sqrt{T}$.

Although the measured HEMT noise does decrease with base temperature over a range of temperatures as predicted, at cryogenic temperatures below 50 K the noise temperature is observed to plateau to values several times larger than expected [72–75]. As the Pospieszlaski model relies on the simple fitting of empirical data, it cannot provide any physical guidance on the mechanisms setting this saturation. Consequently, at present, the precise origin of excess HEMT noise is an open question. The observed noise temperature plateau has been attributed to a variety of mechanisms including drain shot noise [76], gate leakage current [55], and self-heating [72, 77]. In recent years, the self-heating mechanism has garnered particular interest. The typical operating conditions of cryogenic HEMTs require milliwatts of dissipation through the channel. Recent computational studies asserts that under these conditions, the thermal resistance of the intrinsic device is substantially larger than that predicted by diffusion theory, and consequently there may be significant local heating in devices operated cryogenically [72]. The concomitant thermal noise could be responsible for the observed noise plateau.

Predicting the temperature of the active gate region of HEMT devices is therefore critical in quantifying the noise floor of modern devices. The small size ($L_g \sim 100$ nm) and buried structure of HEMTs present unique challenges to conventional thermometery techniques such as IR microscopy [78, 79], micro-Raman spectroscopy [80–82], or liquid crystal thermography [83]. In particular, IR microscopy cannot capture the temperature rise of buried layers in the HEMT structure, Raman spectroscopy typically uses spot-sizes that are much larger than the sub-micron gate lengths, and liquid crystal thermography requires the preparation of special samples. In light of these difficulties, we employ a method utilizing the diode characteristics of the HEMT to obtain the first *in situ* measurements of the gate temperature and

thermal resistance as a function of the base temperature and bias. The measurements indicate that at liquid helium temperatures the thermal noise from the HEMT gate may be several times larger than predicted by ambient conditions. We conclude that without improvements in thermal management, self-heating results in a practical lower limit for microwave noise figure of HEMTs at cryogenic temperatures.

1.3 Outline of thesis

In this thesis, we seek to expand upon the knowledge of electronic fluctuations in semiconductor materials and devices through both simulations and experiments.

In Chapter 2, we present a novel framework for the first parameter-free calculation of electronic fluctuations about a non-equilibrium steady state. Prior to this work, first-principles simulations of semiconductors have primarily focused on near-equilibrium transport coefficients. This chapter builds upon the previous transport theory, providing special emphasis on our extension of the typical "cold electron" treatment to enable the simulation of carriers heated by an electric field. We conclude this chapter with critical details about the numerical implementation of the *ab initio* technique.

In Chapter 3, we demonstrate the utility of our approach by simulating fluctuations in GaAs and silicon. In our first study, we apply the method to the direct computation of the AC mobility and spectral noise power of warm electrons in GaAs using first-principles electronic bandstructure and electron-phonon matrix elements calculated from electronic structure codes. We demonstrate that the spectral features in AC transport properties and noise originate from the disparate time scales of momentum and energy relaxation, despite the dominance of optical phonon scattering. We then demonstrate the method in the more complicated case of hot electron fluctuations in multivalley semiconductors, using silicon as an example material. This application demonstrates that the accepted level of scattering theory, namely one phonon-mediated scattering, cannot capture the warm electron tensor and that incorporating additional mechanisms such as two-phonon scattering will be critical to obtain an accurate description of noise in such materials.

In Chapter 4, we describe the Schottky diode method for the extraction of HEMT gate temperature under cryogenic conditions and bias. In particular we demonstrate evidence that phonon radiation is the dominant mechanism of heat transport in cryogenic HEMTs rather than other mechanisms such as bulk diffusion. Under the radiation regime supported by the measurements, we simulate the expected noise performance of a typical device operating at liquid helium temperatures and evaluate the thermal contribution of the gate in this limit.

Finally, Chapter 5 summarizes key findings from the above work and identifies areas of potential future interest.

Chapter 2

AB INITIO THEORY OF ELECTRONIC FLUCTUATIONS IN SEMICONDUCTORS

This chapter has been adapted, in part, from:

1. **Choi†, Alexander Y.**, Cheng†, P. S., Hatanpää, B. & Minnich, A. J. Electronic noise of warm electrons in semiconductors from first principles. *Phys. Rev. Materials* **5,** 044603. https://link.aps.org/doi/10.1103/PhysRevMaterials.5.04460 (4 Apr. 2021).

   Contributions A.Y.C. wrote the Python backend for Boltzmann Transport calculations, performed the data analysis, made the paper figures, and wrote a majority of the manuscript.

First-principles simulations are important tools in the study of charge transport and carrier dynamics in semiconductor materials. The objective of many *ab initio* studies is to first build a basic model of the relevant physics in a given material, and then to iterate on this model by comparing simulated observables to measurements. In this strategy, more sophisticated mechanisms are incorporated consecutively until the refined model of the physical processes in the material can reproduce all desired observables. There are two principle advantages of performing *ab initio* simulations in parallel to experiments. First, the computation provides access to microscopic variables that would be difficult to access with measurements alone. As such, these studies may contribute insights into the hidden microscopic mechanisms that underpin observed phenomena in materials. Second, simulations that accurately reproduce experimentally measured observables provide verification that the underlying physical model is an accurate representation of the transport processes in the material. Therefore first-principles studies often set the standard for the accepted level of theory of charge transport, bandstructure, and scattering in a given material.

In this chapter, we describe a method for the *ab initio* computation of electronic noise in semiconductors using the Boltzmann Transport Equation (BTE). We begin by discussing the historical treatment of fluctuations that has culminated in our efforts. Next, we outline our use of the BTE and derive transport quantities such as the AC and DC electrical conductivities. Special emphasis is given to how our technique moves beyond the "cold electron" approximation typical in previous *ab initio* works.

Finally, we obtain an expression for the current fluctuation autocorrelation function in terms of the solution to the BTE and use the Wiener-Khintchine Theorem to obtain the noise power spectral density. To conclude this chapter, details critical to the numerical implementation of the method are provided.

2.1 Background

Charge transport in semiconductors is a topic of fundamental and practical interest with a well-established theoretical foundation [84, 85]. In many cases, a sufficient understanding of the relevant physics at both low and high fields can be achieved using the Boltzmann equation with semi-empirical scattering rates [3, 26, 86, 87]. Unfortunately, in many other cases, these semiempirical descriptions can fail to capture the complexity of real materials and often rely upon fitting parameters of ambiguous physical interpretation. Under these circumstances, a more precise description of the electronic transitions induced by phonons and other perturbations is required. Such a description is now possible owing to advances in electronic structure codes that enable the *ab initio* computation of the transition matrix elements given by Fermi's golden rule performed in conjunction with the numerical solution of the Boltzmann equation describing carrier dynamics [14, 25, 88, 89]. While method development is ongoing, these calculations are now routine for various semiconductors including Si [31, 90, 91], GaAs [34, 92, 93], phosphorene [88], and others [32, 94–97].

In contrast to transport, an equivalent treatment of fluctuations from a non-equilibrium steady-state is lacking, despite the experimental accessibility of electronic noise [38, 98] and its importance in applications [99]. One system of theoretical and practical interest is the nondegenerate free electron gas. In equilibrium, closed-form analytical relationships link the Ohmic conductivity, free-electron diffusion, and power spectral density of fluctuations. In particular, the Price relationship links the free-electron diffusion and the spectral noise power [13] while the Nyquist Law, which is a specific realization of the more general fluctuation-dissipation theorems, relates the spectral noise power to the linear electrical conductivity of the material [5, 6, 100].

Nyquist Law of thermal fluctuations from an equilibrium state

Nyquist's original formulation of the law is the result of a simple thought experiment based on lumped-element circuit models as shown in Fig. 2.1 [6]. In Circuit I, Nyquist considered two identical resistors in thermal equilibrium and connected

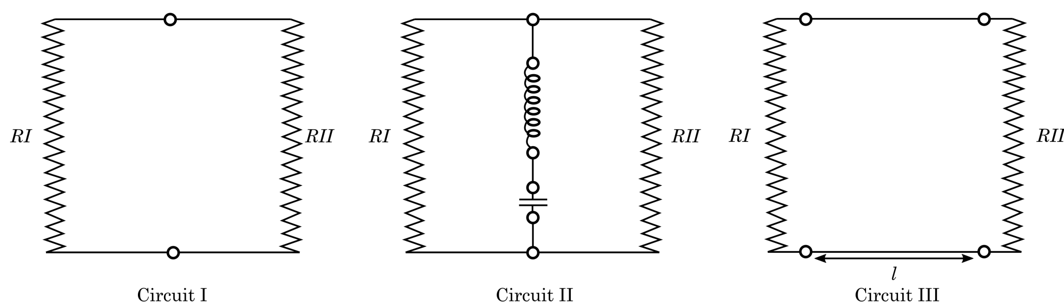

Figure 2.1: The original derivation of Nyquist's Law is a thought experiment utilizing three lumped element circuit models [6]. By combining Circuits I and II with the Second Law of Thermodynamics, Nyquist inferred that the equilibrium thermal noise power is a universal function of temperature, resistance, and frequency. By applying the classical equipartition theorem to Circuit III, Nyquist derived the specific form of the noise power for a single resistive element.

via lossless transmission lines. In such a case, because the resistors are in thermal equilibrium, the emitted noise power from each resistor is identical to that received through absorption from the other resistor. Nyquist then considered Circuit II, in which a resonant circuit is introduced between the conductors such that the power transmitted in a given frequency band is attenuated more than any other band. In such a case, the addition of the circuit would create a mismatch between the power received by the two resistors and one would heat the other. Since this situation would violate the Second Law of Thermodynamics, the power exchanged between the resistors must be equivalent in every frequency band. From Circuits I and II, Nyquist concluded that the electromotive force due to thermal agitation in the conductors is a universal function of temperature, frequency, and resistance alone.

Finally, to determine the form of the universal function, Nyquist considered the network shown in Circuit III. At a specified temperature T, each resistor generates a noise voltage that propagates down the transmission lines of length l. If the transmission line is characterized by an impedance equivalent to the resistance R, the power emitted from each resistor is completely absorbed by the other and standing waves form along the transmission lines with frequencies $f_m = mv(2l)^{-1}$, where $m = 1, 2, 3...$ and v is the propagation velocity in the line. In a given frequency interval Δf, the number of vibrational modes can be expressed as $n = v^{-1}2l\Delta f$. Under the classical equipartition theorem, each degree of freedom contributes energy $E = 1/2k_BT$, where k_B is the Boltzmann constant. Accounting for both the magnetic and electrical degrees of freedom, the noise power contributed by the two resistors can be expressed as $P = 2Ent^{-1} = 2k_BT\Delta f$, where $t = v^{-1}l$.

From simple circuit analysis, the instantaneous current in Circuit III I, can be expressed in terms of the noise voltage on a single resistor $i_n = v_n/2R$. The power contributed by the single resistor is therefore $P_n = \overline{v_n^2}/4R$. Combining this expression with that of the total noise power, the spectral noise power of a single resistive element is expressed as [101]:

$$S_v = \overline{v_n^2}\Delta f^{-1} = 4k_B T R. \tag{2.1}$$

This expression, commonly referred to as the Nyquist Law, specifies the spectral density of thermal fluctuations in a conductor as the simple product of the resistance and the temperature.

Fluctuations from a non-equilibrium steady state

Outside of equilibrium, Eqn. 2.1 no longer applies and kinetic coefficients such as the spectral noise power must be computed with another approach. The theoretical description of fluctuations about a non-equilibrium steady-state has a long history. While the Nyquist and Einstein relationships are not valid outside of equilibrium, for a certain class of systems, the link between transport and fluctuations persists. In 1935, Leontovich used kinetic theory to examine velocity fluctuations of a non-equilibrium gas [102]. Around 20 years later, studying the motion of forced gaseous ions, Wannier established the definition of a diffusion coefficient for transport about a non-equilibrium but steady state [103]. Hashitsume considered a microscopic description of occupancy fluctuations about a steady distribution using the Fokker-Planck equation with a random source term [104]. In analogy with earlier works on fluctuational Maxwell equations, Kadomotsev introduced Langevin sources into the Boltzmann equation [105]. Shortly thereafter, Price derived that for spatially homogeneous fluctuations, a fluctuation-diffusion relation links Wannier's diffusion coefficient to the spectral density of current fluctuations even outside of equilibrium [36]. For this reason, the non-equilibrium noise at frequencies small compared to scattering rates is known as diffusion noise. In the same year, Lax formulated preceding theory into a general kinetic theory of fluctuations for a Markovian system [106]. Throughout the 1960s, Gantsevich and co-workers applied Lax's kinetic theory to dilute gases for which the evolution of the one-particle distribution function is governed by the linear Boltzmann Equation [107]. Their technique, termed the "method of moments," demonstrated how to compute the spectral density of current fluctuations using only the solutions of the linear Boltzmann equation. Concurrently

with Gantsevich, starting from Kadomotsev's Boltzmann-Langevin equation, Kogan and Shul'man developed a Langevin treatment of the current density fluctuations [108]. Lax, van Vliet, and Kogan and Shul'man independently confirmed that the method of moments and the Langevin approach are equivalent [109–111].

As computational resources became increasingly available, numerical implementations of the methods described above permitted computations of electronic noise for both warm ($\Delta T/T_0 \ll 1$) and hot ($\Delta T/T_0 \sim 1$) electrons, where ΔT is the steady-state temperature rise of the electrons and T_0 is the lattice temperature. Due to the lack of knowledge of the precise transition rates between electronic states, these studies employed simplified band structures and parameterized models for scattering such as deformation potential theory for acoustic phonon scattering [112, 113]. For example, Stanton and Wilkins obtained the Green's function of the Boltzmann equation under the single-mode relaxation time approximation, demonstrating qualitative agreement with experiment in GaAs for one [114] and two [115] valley systems. Numerous Monte Carlo simulations reported calculations of current spectral densities in Si [112, 116–120], GaAs [117, 121, 122], and other semiconductors [123–126]. These works employed various approximations such as Debye acoustic phonons, dispersionless optical phonons, and spherical approximations for electron conduction bands. With empirical knowledge of band structure parameters such as effective mass and approximate relaxation times, reasonable agreement with experiments was reported [112, 116–121, 123, 127, 128]. More recently, these methods have been extended to heterostructures and have provided insight into the design of low noise devices [129–131]. While such semi-empirical studies with parameterized models can provide an adequate description of the physics of interest in certain cases, they suffer from restrictions not found in *ab initio* studies. The principle limitation is that it can be difficult to dis-entangle the precise balance of competing noise mechanisms in the high-dimensional parameter spaces common in MC, as the parameters that drive the models are often chosen on an *ad hoc* basis to provide the best match to experimental results. Consequently such studies are not predictive and are necessarily restricted to materials for which mature empirical models of the dominant scattering mechanisms are available. It is therefore natural to consider how advances in the *ab initio* calculation of mean transport quantities [14, 25] can be applied to the non-equilibrium steady state.

In this chapter, we present an *ab initio* theory of electronic noise for non-degenerate semiconductor materials. The formalism provides the spectral noise power and both DC and AC transport quantities without any adjustable parameters. Our method provides a parameter-free view of the microscopic transport processes responsible for electronic fluctuations in semiconductors and will advance fundamental studies of carrier transport and applications of low noise semiconductor devices.

2.2 The Boltzmann Transport Equation

A hierarchy of transport models is available for the simulation of carrier dynamics in materials. At the atomistic extreme are molecular dynamics (MD) methods, in which the positions and momenta of individual charge carriers are simulated over time under a governing equation such as the many-body Schrödinger equation. On the other hand, at the macroscopic extreme are continuum models such as the drift-diffusion equations, which treat the bulk motion of carriers hydrodynamically rather than the individual carriers themselves. Selecting the appropriate model often constitutes a trade-off between the resolution of MD models and the computational simplicity of hydrodynamic treatments. In the present study, we use the Boltzmann Transport Equation as a mesoscopic intermediate between these extremes.

The BTE is a framework that describes the behavior of non-equilibrium particle ensembles under external forcing [27]. In particular, the BTE tracks the evolution of the non-equilibrium distribution function in time, space, and momenta. Because the BTE simulates the statistics of a representative particle through its probability distribution function rather than tracing the motion of each carrier in the population, it can be used to model practical systems at carrier numbers that would be computationally infeasible for MD methods. Simultaneously, the BTE provides resolution at the level of the charge carrier, and quantifies the influence of microscopic quantities such as the mean free paths and scattering rates which are inaccessible to hydrodynamic methods. These qualities inform our choice of the BTE as the appropriate governing equation to model electronic fluctuations in semiconductors.

The BTE is typically expressed as an integro-differential equation in space, time, and momenta. A rigorous derivation of the BTE is beyond the scope of this thesis but is available in the literature [132, 133]. For electrons in a semiconductor, the BTE can be written:

$$\frac{\partial f(\mathbf{x},\mathbf{k},t)}{\partial t} + \mathbf{v}\cdot\nabla_{\mathbf{x}} f(\mathbf{x},\mathbf{k},t) + \frac{\mathbf{F}}{\hbar}\cdot\nabla_{\mathbf{k}} f(\mathbf{x},\mathbf{k},t) = \mathcal{I}[f] \tag{2.2}$$

where f is the non-equilibrium particle distribution function, $\mathbf{x}$ is the position vector, $\mathbf{k}$ is the crystal wavevector, and t is time. The left-hand side of the BTE describes the kinematic evolution of the distribution function over time under spatial gradients $\nabla_{\mathbf{x}}$ and external body forces $\mathbf{F}$. In addition to kinematics, scattering events and collisions may also introduce changes to the distribution function. The influence of these events is captured in the right-hand side of the BTE in the collision term $\mathcal{I}[f]$. Although in general, the BTE is difficult to solve due to its high-dimensionality, under the appropriate approximations, it can be a powerful tool for simulating transport and fluctuations in semiconductor systems. In the next section, we derive closed form expressions for transport and fluctuation observables in non-degenerate, spatially homogeneous semiconductors in terms of solutions to the BTE.

2.3 Calculating steady-state transport observables with the BTE

We begin by reviewing the *ab initio* treatment of steady-state transport using the BTE and set the notation to be used henceforth. Consider a non-degenerate, spatially homogeneous electron gas subject to an external electric field $\mathcal{E}$. The system is governed by the following Boltzmann equation:

$$\frac{\partial f_{m\mathbf{k}}}{\partial t} + \sum_{\gamma} \frac{e\mathcal{E}_{\gamma}}{\hbar} \frac{\partial f_{m\mathbf{k}}}{\partial_{k_{\gamma}}} = \mathcal{I}[f_{m\mathbf{k}}]. \tag{2.3}$$

Here, we have neglected the time and spatial derivatives of Eqn. 2.2 and shifted the explicit dependence on band and wavevector to an index $m\mathbf{k}$. $f_{m\mathbf{k}}$ is the distribution function that describes the occupancy of the electron state with wave vector $\mathbf{k}$ and band index m, e is the fundamental charge, $\hbar$ is the reduced Planck constant, and $\gamma = x, y, z$ indexes the crystal axes. In the steady case, the transient term vanishes, and we denote the solution of the resulting equation as $f^s_{m\mathbf{k}}$. The collision integral, $\mathcal{I}$, describes the scattering rates between electronic Bloch states $m\mathbf{k}$ and $m'\mathbf{k}'$. In general, the collision integral is a nonlinear functional of the distribution function given by Fermi's Golden Rule [84].

In many problems, a good approximation is that the Boltzmann equation can be linearized about an equilibrium distribution as $f^s_{m\mathbf{k}} \equiv f^0_{m\mathbf{k}} + \Delta f_{m\mathbf{k}}$, where $\Delta f_{m\mathbf{k}}$ is the change in occupation due to the electric field $\mathcal{E}$ relative to the equilibrium distribution $f^0_{m\mathbf{k}}$. Under the non-degenerate assumption, $f^0_{m\mathbf{k}}$ is well approximated by the Maxwell-Boltzmann distribution. With this substitution and retaining only

terms linear in $\Delta f_{m\mathbf{k}}$, the Boltzmann equation becomes [86]:

$$\sum_{\gamma}\left[\frac{e\mathcal{E}_{\gamma}}{\hbar}\frac{\partial\Delta f_{m\mathbf{k}}}{\partial_{k_{\gamma}}}\right]+\sum_{m'\mathbf{k}'}\Theta_{m\mathbf{k}m'\mathbf{k}'}\Delta f_{m'\mathbf{k}'}=-\sum_{\gamma}\frac{e\mathcal{E}_{\gamma}}{\hbar}\frac{\partial f^{0}_{m\mathbf{k}}}{\partial_{k_{\gamma}}} \tag{2.4}$$

where $\Theta_{m\mathbf{k}m'\mathbf{k}'}$ is the linearized collision integral.

$$\Theta_{m\mathbf{k}m'\mathbf{k}'}=\frac{2\pi}{\mathcal{N}\hbar}\sum_{m'\nu\mathbf{q}}|g_{m\mathbf{k},m'\mathbf{k+q}}|^{2}\Big[\delta(\epsilon_{m\mathbf{k}}-\hbar\omega_{\nu\mathbf{q}}-\epsilon_{m'\mathbf{k+q}})H_{em}+\delta(\epsilon_{m\mathbf{k}}+\hbar\omega_{\nu\mathbf{q}}-\epsilon_{m'\mathbf{k+q}})H_{abs}\Big] \tag{2.5}$$

Here, $g_{m\mathbf{k},m'\mathbf{k}'}$ is the electron-phonon matrix element coupling electron state $m\mathbf{k}$ to another electron state $m'\mathbf{k}'=m'\mathbf{k}+\mathbf{q}$ via emission or absorption of a phonon with wave vector $\mathbf{q}$, polarization ν, and occupancy $N_{\nu\mathbf{q}}$ given by the Bose distribution. $\mathcal{N}$ is the total number of $\mathbf{q}$-points. The linearized emission and absorption weights are:

$$\begin{aligned}H_{ems}&=\Delta f_{\mathbf{k}}(N_{\mathbf{q}}+1-f^{0}_{\mathbf{k+q}})-\Delta f_{\mathbf{k+q}}(N_{\mathbf{q}}+f^{0}_{m\mathbf{k}})\\ H_{abs}&=\Delta f_{\mathbf{k}}(N_{\mathbf{q}}+f^{0}_{m\mathbf{k}})-\Delta f_{\mathbf{k+q}}(N_{\mathbf{q}}+1-f^{0}_{\mathbf{k+q}}).\end{aligned} \tag{2.6}$$

The δ-functions of Eqn. 2.5 are representative of the requirement for the conservation of energy associated with the transition. The conservation of crystal momentum is implicit in the sum over q phonon wavevector, as only modes conserving momentum are calculated. Note that in Eqn. 2.4, we have moved the collision integral to the left-hand side and defined Eqn. 2.5 without the usual minus sign to simplify the following expressions.

Warm electron scattering via one-phonon processes

As discussed in Ch. 1, in this thesis, we focus on the simulation of electronic fluctuations induced by phonon-mediated scattering. The scattering matrix presented above is calculated from the lowest-order terms in the perturbation expansion of the electron-phonon interaction [25]. As formulated, $\Theta_{m\mathbf{k}m'\mathbf{k}'}$ represents the scattering events mediated by a *single* phonon emission or absorption event, and is therefore termed the 1ph scattering matrix. Although expansion to the leading order is often sufficient to obtain reasonable approximation of the physics, and in many well-studied materials such as Si [90], MoS_2 [31], and GaN [94], 1ph scattering

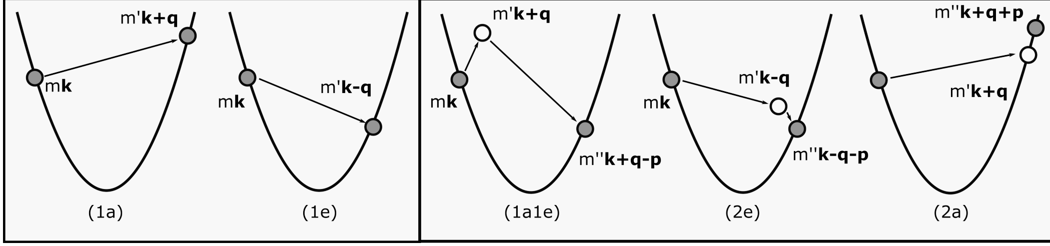

Figure 2.2: The scattering matrix used in this thesis is a lowest-order expansion of the electron phonon interaction in solids and therefore accounts for the simplest form of e-ph scattering, that mediated by the emission (1e) or absorption (1a) of a single phonon with momentum $\mathbf{q}$. Higher-order perturbation expansions are needed to capture phenomena such as two-phonon (2ph), which include one emission, one absorption (1e1a), two absorption (2a) and two emission (2e) transitions. Calculations of two-phonon processes are computationally challenging owing to the larger phase space, as the intermediate states in the transition are not confined to the bandstructure. Figure adapted from Ref. [93].

is conventionally understood to dominate charge transport processes On the other hand, next-to-leading order effects such as two-phonon scattering are known to be important in certain classes of materials such as polar semiconductors [39]. The first-principles calculation of these higher-order processes is non-trivial. For example, in the calculation of two-phonon mediated-processes, the number of Feynmann diagrams expands to include the emission-absorption (1e1a), emission-emission (2e), and absorption-absorption transitions (2a) depicted in Fig. 2.2. The phase space associated with two-phonon scattering is much larger than that of one-phonon processes, as the intermediate scattering state is not confined to the bandstructure shell. To account for these new processes, one must perform computationally expensive Brillouin zone sums over two sets of crystal momenta corresponding to each phonon (for more detail see the Results section of [93]). Owing to these challenges, in the present study, we restrict ourselves to the investigation of fluctuations induced by the 1ph scattering captured by $\Theta_{m\mathbf{k}m'\mathbf{k}'}$.

As a further simplification, one may restrict the electric field to values where $\Delta f_{m\mathbf{k}} \ll f^0_{m\mathbf{k}}$ so that the linearization of Eqn. 2.4 is valid. However, in the typical *ab initio* treatment of transport, the electric field is further assumed to be small enough such that $\partial f_{m\mathbf{k}}/\partial_{k_\gamma} \approx \partial f^0_{m\mathbf{k}}/\partial_{k_\gamma}$, allowing $\Delta f_{m\mathbf{k}}$ to be obtained by an iterative method with only knowledge of $\Theta_{m\mathbf{k}m'\mathbf{k}'}$ and the equilibrium distribution $f^0_{m\mathbf{k}}$ [25]. In the present problem, the field is sufficiently large such that $\partial \Delta f_{m\mathbf{k}}/\partial_{k_\gamma} \sim \partial f^0_{m\mathbf{k}}/\partial_{k_\gamma}$ and the neglected derivative term, $\partial \Delta f_{m\mathbf{k}}/\partial_{k_\gamma}$, must be included. This approximation was originally denoted as the ‘warm electron’ approximation since the excess energy

of the electrons over the thermal value can be non-zero while remaining small on that scale [87]. Section 4.2 contains more information about the numerical evaluation of the non-equilibrium drift operator in GaAs.

To treat the drift term numerically, we employ a finite difference approximation:

$$\sum_{\gamma} \frac{e\mathcal{E}_\gamma}{\hbar} \frac{\partial \Delta f^s_{m\mathbf{k}}}{\partial_{k_\gamma}} \approx \sum_{\gamma} \frac{e\mathcal{E}_\gamma}{\hbar} \sum_{m'\mathbf{k}'} D_{m\mathbf{k}m'\mathbf{k}',\gamma}\, \Delta f_{m'\mathbf{k}'} \tag{2.7}$$

where the momentum-space derivative is approximated using a nearest-neighbor central-difference scheme [134, 135]. Under this scheme, the momentum term can be approximated to first order as:

$$\sum_{m'\mathbf{k}'} D_{m\mathbf{k}m'\mathbf{k}',\gamma}\, \Delta f_{m'\mathbf{k}'} = \sum_{\mathbf{b}} (\Delta f_{m\mathbf{k}+\mathbf{b}} - \Delta f_{m\mathbf{k}}) w_b \mathbf{b} \tag{2.8}$$

where $\mathbf{b}$ is the distance vector linking the reference point to nearest neighbors and w_b is a weighting factor that obeys:

$$w_b \sum_i b^i_\alpha b^i_\beta = \delta_{\alpha\beta} \tag{2.9}$$

where α and β represent crystal axes of the system. A representation of the nearest neighbors linked in the finite difference scheme is shown in Fig. 2.3.

With these definitions, the steady Boltzmann equation becomes:

$$\sum_{m'\mathbf{k}'} \Lambda_{m\mathbf{k}m'\mathbf{k}'} \Delta f_{m'\mathbf{k}'} \equiv \sum_{\gamma} \sum_{m'\mathbf{k}'} \left[\frac{e\mathcal{E}_\gamma}{\hbar} D_{m\mathbf{k}m'\mathbf{k}',\gamma} + \Theta_{m\mathbf{k}m'\mathbf{k}'} \right] \Delta f_{m'\mathbf{k}'} = \sum_{\gamma} \frac{e\mathcal{E}_\gamma}{k_B T} v_{m\mathbf{k},\gamma} f^0_{m\mathbf{k}}. \tag{2.10}$$

Here, we have analytically expanded the gradient of the equilibrium Boltzmann distribution on the right-hand side as:

$$\frac{\partial f^0_{m\mathbf{k}}}{\partial_{k_\gamma}} = -\frac{\hbar v_{m\mathbf{k},\gamma}}{k_B T} f^0_{m\mathbf{k}} \tag{2.11}$$

where $v_{m\mathbf{k}}$ is the group velocity and $k_B T$ is the thermal energy. $\Lambda_{m\mathbf{k}m'\mathbf{k}'}$ is defined as the relaxation operator that combines the drift and scattering operators.

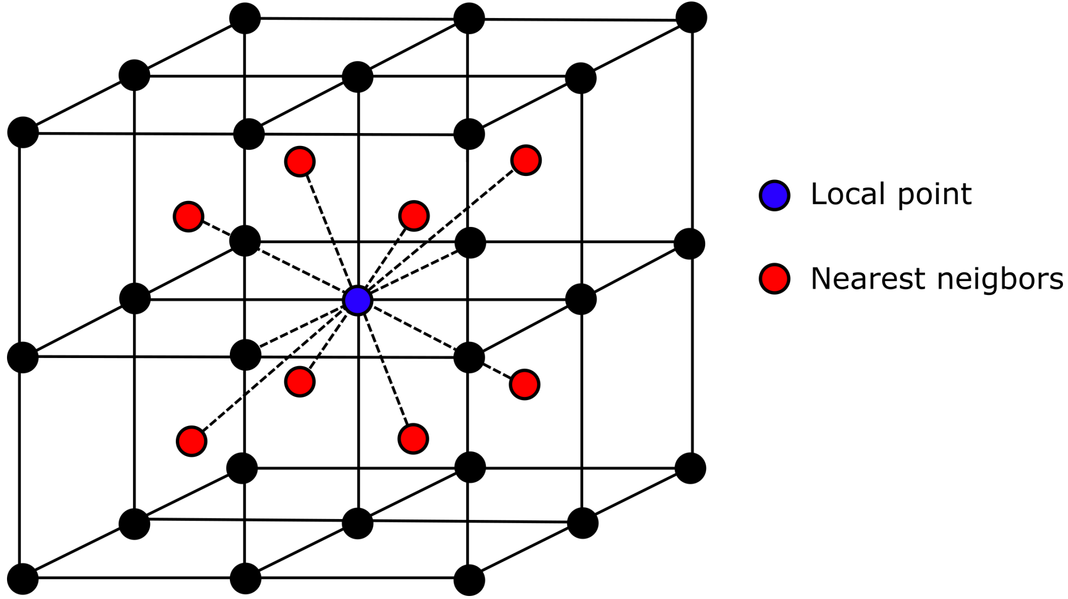

Figure 2.3: The central difference scheme used to approximate the momentum derivative in Eqn. 2.8 relates the local derivative to the value of the distribution in the nearest neighbor states. The dashed lines represent the distance vector **b**. The central difference approximation enables us move beyond the typical "cold-electron" approximation and treat electrons that have been heated above the lattice temperature.

Equation 2.10 shows that the steady Boltzmann equation is now a system of linear equations. The solution, $\Delta f_{m\mathbf{k}}$, can be written symbolically using the inverse relaxation operator:

$$\Delta f_{m\mathbf{k}} = \sum_{m'\mathbf{k}'} \Lambda^{-1}_{m\mathbf{k}m'\mathbf{k}'} \sum_{\gamma} \left(\frac{e\mathcal{E}_\gamma}{k_B T}\right) v_{m'\mathbf{k}',\gamma} f^0_{m'\mathbf{k}'}. \tag{2.12}$$

Once the solution vector is calculated, transport properties such as the electrical conductivity can be defined using the steady distribution. In particular, the linear DC conductivity $\sigma^{lin}_{\alpha\beta}$ can be expressed as:

$$\sigma^{lin}_{\alpha\beta} = \frac{2e^2}{k_B T \mathcal{V}_0} \sum_{m\mathbf{k}} v_{m\mathbf{k},\alpha} \sum_{m'\mathbf{k}'} (\Theta^{-1}_{m\mathbf{k}m'\mathbf{k}'} v_{m'\mathbf{k}',\beta} f^0_{m'\mathbf{k}'}) \tag{2.13}$$

where the factor of 2 accounts for spin degeneracy and $\mathcal{V}_0$ is the product of the unit cell volume and the number of cells, or the supercell volume. The field is applied along the β axis and the resulting current is measured along the α axis. The conductivity of Eqn. 2.13 is typically calculated in the cold electron

approximation for which $\partial \Delta f_{m\mathbf{k}}/\partial_{k_\gamma} \ll \partial f^0_{m\mathbf{k}}/\partial_{k_\gamma}$. This cold electron conductivity is thus independent of the electric field and is only a valid description of transport for small perturbations from equilibrium such that the above approximation is valid.

For sufficiently large fields that $\partial \Delta f_{m\mathbf{k}}/\partial_{k_\gamma} \sim \partial f^0_{m\mathbf{k}}/\partial_{k_\gamma}$, the DC conductivity depends on the electric field and is defined with the relaxation operator:

$$\sigma_{\alpha\beta}(\mathcal{E}) = \frac{2e^2}{k_B T \mathcal{V}_0} \sum_{m\mathbf{k}} v_{m\mathbf{k},\alpha} \sum_{m'\mathbf{k}'} \Lambda^{-1}_{m\mathbf{k}m'\mathbf{k}'} \, v_{m'\mathbf{k}',\beta} \, f^0_{m'\mathbf{k}'} \tag{2.14}$$

Another important transport quantity, the AC small-signal conductivity $\sigma^{\omega}_{\alpha\beta}$, describes the linear response of the system about a non-equilibrium steady-state to a transient electric field [38]. With the steady distribution $f^s_{m\mathbf{k}}$ being set by a DC field $\mathcal{E}$ as described above, an AC field perturbation along crystal axis γ, $\delta\mathcal{E}_\gamma(t) = \delta\mathcal{E}_\gamma e^{i\omega t}$, induces a fluctuation of the steady distribution $\delta f_{m\mathbf{k}}(t) = \delta f_{m\mathbf{k}}(\omega) e^{i\omega t}$. The response of the system to such a fluctuation is governed by the Fourier transformed Boltzmann equation:

$$\sum_{m'\mathbf{k}'} (i\omega\,\mathbb{I} + \Lambda)_{m\mathbf{k}m'\mathbf{k}'} \, \delta f_{m'\mathbf{k}'} = -\sum_{\gamma} \frac{e\delta\mathcal{E}_\gamma}{\hbar} \frac{\partial f^s_{m\mathbf{k}}}{\partial_{k_\gamma}}. \tag{2.15}$$

Here, $\mathbb{I}$ is the identity matrix and ω is the angular frequency. The fluctuation in the distribution function induces a current fluctuation about the DC value, given as:

$$\delta j_\alpha = \frac{2e}{\mathcal{V}_0} \sum_{m\mathbf{k}} v_{m\mathbf{k},\,\alpha} \, \delta f_{m\mathbf{k}}. \tag{2.16}$$

The small-signal AC conductivity is defined as the linear coefficient relating the current density variation to the perturbation, $\sigma^{\omega}_{\alpha\beta} \equiv \delta j_\alpha / \delta\mathcal{E}_\beta$. An explicit expression for AC conductivity can be obtained by combining the above expressions:

$$\sigma^{\omega}_{\alpha\beta} = \frac{2e}{\mathcal{V}_0 \delta\mathcal{E}_\beta} \sum_{m\mathbf{k}} v_{m\mathbf{k},\alpha} \sum_{m'\mathbf{k}'} (i\omega\,\mathbb{I} + \Lambda)^{-1}_{m\mathbf{k}m'\mathbf{k}'} \left[\sum_{\gamma} -\frac{e\delta\mathcal{E}_\gamma}{\hbar} \frac{\partial f^s_{m'\mathbf{k}'}}{\partial_{k'_\gamma}} \right]. \tag{2.17}$$

At equilibrium the steady distribution reduces to the equilibrium distribution $f^s_{m\mathbf{k}} = f^0_{m\mathbf{k}}$, the kinetic operator reduces to the scattering operator, $\Lambda_{m\mathbf{k}m'\mathbf{k}'} = \Theta_{m\mathbf{k}m'\mathbf{k}'}$. By examining Eq. 2.13 and Eq. 2.17, we see that at equilibrium the zero-frequency differential conductivity is equal to the linear DC conductivity $\sigma^{\omega=0}_{\alpha\beta}(\mathcal{E} = 0) = \sigma^{lin}_{\alpha\beta}$.

2.4 Calculating fluctuations about a non-equilibrium steady state with the BTE

The previous section demonstrates how the BTE can be used to compute the transport quantities that characterize the bulk linear response of the system to the perturbations induced by an electric field. In this section, we now extend this treatment to consider fluctuations about a non-equilibrium steady state induced by the stochastic nature of charge carrier scattering. Suppose that the steady state distribution $f^s_{m\mathbf{k}}$ is known. Just as in equilibrium, fluctuations in the instantaneous occupation of the quantum states occur. Microscopically, these fluctuations arise because of the stochastic nature of the scattering described by $\Theta_{m\mathbf{k}m'\mathbf{k}'}$. At steady state, detailed balance requires that the mean flux of particles into every quantum state is zero. However, the flux of particles into or out of a quantum state is a Poissonian process and is characterized by a variance. Therefore, the instantaneous net flux into a quantum state is in general non-zero due to instantaneous imbalance between the incoming and outgoing fluxes [4]. Consequently, the occupancy of quantum states fluctuates under both equilibrium and non-equilibrium conditions.

In the macroscopic limit at which fluctuations are observed in the laboratory, these distribution function fluctuations appear as instantaneous current fluctuations, or equivalently, as electronic noise. A non-random characteristic of these fluctuations is the spectral density of current density fluctuations, which represents the squared sum of the deviation's Fourier components over an infinitesimal frequency range. The Wiener-Khintchine Theorem relates the power spectral density to the single-sided Fourier transform of the autocorrelation of the current density fluctuations [38]:

$$S_{j_\alpha j_\beta}(\omega) \equiv (\delta j_\alpha \delta j_\beta)_\omega = 2\int_{-\infty}^{\infty} \overline{\delta j_\alpha(t)\delta j_\beta} e^{-i\omega t} dt \tag{2.18}$$

where the overbar indicates ensemble average over all microscopic states in the system.

Just as the macroscopic transport variables can be calculated in terms of the mean occupation functions, one can express the fluctuations in the same macroscopic quantities to microscopic fluctuations in the distribution function. Following Ref. [4], we now consider random fluctuations about the non-equilibrium steady state, $\delta f_{m\mathbf{k}}(t) = f_{m\mathbf{k}}(t) - f^s_{m\mathbf{k}}$. In contrast to the fluctuations associated with the small signal conductivity described in Eqn. 2.17, these fluctuations are induced by

the stochastic nature of scattering rather than an external perturbation. The corresponding current density fluctuations can be expressed in terms of the fluctuation in the distribution function as in Eqn. 2.16.

It follows that the ensemble average of the correlation function of instantaneous current fluctuations along axes α and β, $\overline{\delta j_\alpha(t)\delta j_\beta}$, can be expressed in terms of the correlation function of the occupancy fluctuations, $\overline{\delta f_{m\mathbf{k}}(t)\delta f_{m_1\mathbf{k}_1}}$:

$$\overline{\delta j_\alpha(t)\delta j_\beta} = \left(\frac{2e}{\mathcal{V}_0}\right)^2 \sum_{m\mathbf{k}} \sum_{m_1\mathbf{k}_1} v_{m\mathbf{k},\alpha}\, v_{m_1\mathbf{k}_1,\beta}\, \overline{\delta f_{m\mathbf{k}}(t)\delta f_{m_1\mathbf{k}_1}}. \tag{2.19}$$

Equation 2.19 shows that computing the spectral density of current density fluctuations requires calculating the correlations of single-particle occupancy fluctuations $\overline{\delta f_{m\mathbf{k}}(t)\delta f_{m_1\mathbf{k}_1}}$. This function is known as the time-displaced, two-particle correlation function [4]. Through a quantum statistical mechanical treatment, Gantsevich and coauthors have demonstrated that the time-displaced, two-particle correlation function obeys the same Boltzmann equation as the fluctuation itself [107]:

$$\frac{\partial}{\partial t}\overline{\delta f_{m\mathbf{k}}(t)\delta f_{m_1\mathbf{k}_1}} + \sum_{m'\mathbf{k}'} \Lambda_{m\mathbf{k}m'\mathbf{k}'}\, \overline{\delta f_{m'\mathbf{k}'}(t)\delta f_{m_1\mathbf{k}_1}} = 0. \tag{2.20}$$

This result is surprising initially, but a simple physical interpretation helps to make matters clear. The correlation $\overline{\delta f_{m\mathbf{k}}(t)\delta f_{m_1\mathbf{k}_1}}$ is a smooth function of time that describes the average time evolution of a fluctuation $\delta f_{m\mathbf{k}_1}$. The system does not distinguish between stochastic fluctuations and deviations from equilibrium induced by macroscopic external perturbations. Therefore, it should not be surprising that the regression to a steady state is governed by the Boltzmann Equation in both cases. The importance of this result cannot be overstated. We have seen previously that quantifying the noise of the system requires calculating the correlation of occupancy fluctuations. Equation 2.20 indicates that the simulation of fluctuations can be performed with only the information needed to describe the relaxation of the carriers to a steady state [106]. The physical intuition behind this argument is essentially an extension of Onsager's regression hypothesis to non-equilibrium systems (in particular, see Sec. 1 of Ref. [4]).

Solving Eqn. 2.20 requires the specification of an initial condition, $\overline{\delta f_{m'\mathbf{k}'}\delta f_{m_1\mathbf{k}_1}}$, which is known as the one-time, two-particle correlation function. For a non-degenerate system with a fixed number of particles N, this requirement was identified

by Fowler [136] and Lax [106] as the standard problem of distributing indistinguishable balls into labeled boxes, and can therefore be described using the multinomial distribution. For correlations between states labeled by band and wavevector, the condition is expressed:

$$\overline{\delta f_{m\mathbf{k}}\delta f_{m_1\mathbf{k}_1}} = f_{m\mathbf{k}}\delta_{\mathbf{k}\mathbf{k}_1}\delta_{mm_1} - \frac{f_{m\mathbf{k}}f_{m_1\mathbf{k}_1}}{N} \tag{2.21}$$

where the second term on the right-hand side indicates that a correlation exists between occupancies due to the fixed particle number. It should be noted that in the degenerate limit, two-particle collisions among charge carriers introduce additional correlation between the states. In principle, this correlation can be accounted for through an additional term in Eqn. 2.21 (see Ch. 3 in [38]), but is beyond the scope of present work. For the non-degenerate systems of present interest, one cam combine the initial condition for the correlation, Eqns. 2.18, 2.19, and 2.20, to express the spectral density of current fluctuations explicitly in terms of solutions to the Boltzmann equation. For a single band, we drop the band index to get:

$$(\delta j_\alpha \delta j_\beta)_\omega = \left(\frac{2e}{\mathcal{V}_0}\right)^2 \sum_{\mathbf{k},\mathbf{k}_1} v_{\mathbf{k},\alpha}\, v_{\mathbf{k}_1,\beta}\, (\delta f_{\mathbf{k}}\delta f_{\mathbf{k}_1})_\omega. \tag{2.22}$$

As with the current density, the spectral density of distribution function fluctuations is related to its analagous correlation function by Fourier transform:

$$(\delta f_{\mathbf{k}}\delta f_{\mathbf{k}_1})_\omega = \int_{-\infty}^{\infty} \overline{\delta f_{\mathbf{k}}(t)\delta f_{\mathbf{k}_1}}\, \mathrm{e}^{-i\omega t}\, dt. \tag{2.23}$$

Constraining the solution to times $t > 0$ and employing the familiar stationarity property of the correlation $\overline{\delta f_{m\mathbf{k}}(-t)\delta f_{\mathbf{k}_1}} \equiv \overline{\delta f_{m\mathbf{k}}(t_1 - t)\delta f_{\mathbf{k}_1}(t)} = \overline{\delta f_{\mathbf{k}_1}(t)\delta f_{m\mathbf{k}}}$, it follows that the spectral density can be expressed as:

$$(\delta f_{\mathbf{k}}\delta f_{\mathbf{k}_1})_\omega = 2\Re\left[\sum_{\mathbf{k}'}(i\omega\,\mathbb{I} + \Lambda)^{-1}_{\mathbf{k}\mathbf{k}'}\, \overline{\delta f_{\mathbf{k}'}\,\delta f_{\mathbf{k}_1}}\right]. \tag{2.24}$$

Combining Eqns. 2.21, 2.22, and 2.24, we obtain the following expression:

$$S_{j_\alpha j_\beta}(\omega) = 2\left(\frac{2e}{\mathcal{V}_0}\right)^2 \Re\left[\sum_{\mathbf{k}} v_{\mathbf{k},\alpha} \sum_{\mathbf{k}'} (i\omega\,\mathbb{I} + \Lambda)^{-1}_{\mathbf{k}\mathbf{k}'} \sum_{\mathbf{k}_1} v_{\mathbf{k}_1,\beta}\left(f^s_{\mathbf{k}'}\delta_{\mathbf{k}'\mathbf{k}_1} - \frac{f^s_{\mathbf{k}'}f^s_{\mathbf{k}_1}}{N}\right)\right]. \tag{2.25}$$

In practice, the numerical evaluation of Eqn. 2.25 is simplified by performing the integral over the initial momentum state $\mathbf{k}_1$ analytically.

$$S_{j_\alpha j_\beta}(\omega) = 2\left(\frac{2e}{\mathcal{V}_0}\right)^2 \Re\left[\sum_{\mathbf{k}} v_{\mathbf{k},\alpha} \sum_{\mathbf{k}'} (i\omega\,\mathbb{I} + \Lambda)^{-1}_{\mathbf{k}\mathbf{k}'} \left(f^s_{\mathbf{k}'}(v_{\mathbf{k}',\beta} - V_\beta)\right)\right] \tag{2.26}$$

Here, V_β is the drift velocity along the β axis defined as:

$$V_\beta = \frac{1}{N}\sum_{\mathbf{k}} v_{\mathbf{k},\beta} f^s_{\mathbf{k}} \tag{2.27}$$

where $N = \sum_{\mathbf{k}} f_{\mathbf{k}}$ is the total particle number.

From Eqn. 2.26, it follows that calculating the spectral density of the current fluctuations requires solving the inhomogeneous Boltzmann equation twice. First, the steady occupation function must be obtained using Eqn. 2.12. Then, the Boltzmann equation is solved again with inhomogeneous term $f^s_{\mathbf{k}}(v_{\mathbf{k},\beta} - V_\beta)$ with $f^s_{m\mathbf{k}} \equiv f^0_{m\mathbf{k}} + \Delta f_{m\mathbf{k}}$. The appropriate Brillouin zone integrations are then performed to calculate the power spectral density.

Recovering Nyquist Law from the BTE

As a check of the above derivation, consider an equilibrium system for which $\mathcal{E}_\gamma = 0$ and $V_\gamma = 0$. The equation is simplified as $f^s_{\mathbf{k}} = f^0_{\mathbf{k}}$ and $\Lambda_{\mathbf{k}\mathbf{k}'} = \Theta_{\mathbf{k}\mathbf{k}'}$. Then, we have:

$$S_{j_\alpha j_\beta}(\mathcal{E}=0) = 2\left(\frac{2e}{\mathcal{V}_0}\right)^2 \Re\left[\sum_{\mathbf{k}} v_{\mathbf{k},\alpha} \sum_{\mathbf{k}'} (i\omega\,\mathbb{I} + \Theta)^{-1}_{\mathbf{k}\mathbf{k}'} f^0_{\mathbf{k}'} v_{\mathbf{k}',\beta}\right]. \tag{2.28}$$

With the same simplifications, the equilibrium AC conductivity from Eqn. 2.17 is:

$$\sigma^\omega_{\alpha\beta}(\mathcal{E}=0) = \frac{2e^2}{\hbar\mathcal{V}_0}\sum_{\mathbf{k}} v_{\mathbf{k},\alpha}(i\omega\,\mathbb{I} + \Theta)^{-1}_{\mathbf{k}\mathbf{k}'}\left[-\frac{\partial f^0_{\mathbf{k}'}}{\partial_{k'_\beta}}\right]. \tag{2.29}$$

Combining the above expressions, we obtain the familiar Nyquist relationship [6]:

$$S_{j_\alpha j_\beta}(\mathcal{E}=0) = 4\frac{k_B T_0}{\mathcal{V}_0}\Re[\sigma^\omega_{\alpha\beta}(\mathcal{E}=0)]. \tag{2.30}$$

This relationship is formally valid only in equilibrium, but remains approximately true in the 'cold' electron regime for which $\partial f^s_{m\mathbf{k}}/\partial_{\mathbf{k}} \approx \partial f^0_{m\mathbf{k}}/\partial_{\mathbf{k}}$ and $\Delta f_{m\mathbf{k}} \ll f^0_{m\mathbf{k}}$ such that $\Lambda_{\mathbf{k}\mathbf{k}'} \approx \Theta_{\mathbf{k}\mathbf{k}'}$ and $f^s_{m\mathbf{k}} \approx f^0_{m\mathbf{k}}$.

The theory presented above represents a method for the first *ab initio* calculation of the power spectral density of current fluctuations in semiconductors. Our technique moves beyond the "cold electron" approximation typical in previous *ab initio* works by incorporating a finite difference approximation for the drift operator in the Boltzmann Transport Equation, thus permitting the simulation of warm and hot electrons. Briefly, this method is an appropriate description of fluctuations about the nonequilibrium steady state under the same conditions for which the semiclassical Boltzmann Equation is valid. These conditions can be summarized in two points [27]. First, it is assumed that collision times are sufficiently brief such that they may be considered instantaneous compared to any relevant time scale in the system. Second, it is assumed that collisions are sufficiently infrequent such that they may be considered statistically independent of each other. For the non-degenerate carrier gas systems of present interest, these dilute gas assumptions are valid and the above method is suitable. To conclude this chapter, we describe details critical to the numerical implementation of the theory.

2.5 Numerical implementation of simulations

We now describe the implementation details to compute the spectral noise power and other quantities using the theory from Ch. 2. In particular, in the next chapter, we provide the results of these computations in GaAs and Si. The inputs to the Boltzmann equation are the electronic structure and electron-phonon matrix elements $g_{m\mathbf{k},m'\mathbf{k+q}}$ calculated using electronic structure packages. First, the electronic structure and electron-phonon matrix elements for both GaAs and Si are computed on a coarse $8 \times 8 \times 8$ grid using density functional theory (DFT) and density functional perturbation theory (DFPT), respectively, with Quantum Espresso (QE) [29, 137]. These quantities are then interpolated to finer grids using Wannier interpolation with Perturbo [30]. Perturbo includes corrections for polar materials that are necessary in GaAs [138].

The electronic structure calculations using QE employ simulation parameters that are routine in the literature as in Ref. [92, 139]. Briefly, in GaAs use a plane wave cutoff of 72 Ryd and a relaxed lattice parameter of 5.556 Å while in Si we use a cutoff of 40 Ryd and a relaxed lattice parameter of 5.43 AA. We set the Fermi level to obtain a carrier concentration of 10^{15} cm^{-3} in GaAs and $10^{1}6$ cm^{-3} in Si corresponding to a non-degenerate electron gases. We consider only conduction band electronic states within an energy cutoff above the conduction band minimum (CBM) of 335 meV in GaAs and 300 meV in Si. These energy windows are larger

than the window used in typical electron transport calculations since the present calculations allow the electric field to heat the electrons, leading to occupation at higher energy states. Further increasing the energy window by 50 meV had negligible effect on the observables of interest like spectral noise power.

In PERTURBO, we use a grid of $200 \times 200 \times 200$ in GaAs and $100 \times 100 \times 100$ in Si for the Wannier interpolated electronic structures and electron-phonon matrix elements. The transition rates of Eqn. 2.5 are calculated at 300 K. For warm electrons in GaAs, we consider convergence by determining the change in the spectral noise power at the maximum electric field for which the $\Delta f_{m\mathbf{k}} \ll f^0_{m\mathbf{k}}$ assumption is satisfied. Numerical experimentation shows that this condition is satisfied for $\mathcal{E} \lesssim 800\ \mathrm{V\,cm^{-1}}$. The spectral noise power at $800\ \mathrm{V\,cm^{-1}}$ using the $200 \times 200 \times 200$ grid differs by less than 1% from the value obtained on a grid with twice the number of grid points. The delta function in the electron-phonon matrix elements is approximated with a Gaussian with a 10 meV broadening parameter in GaAs [92] and 5 meV in Si [30]. Decreasing the broadening to 6 meV in GaAs changed the spectral noise power at $800\ \mathrm{V\,cm^{-1}}$ by less than 3%.

While PERTURBO performs the Wannier interpolation for the electron-phonon interaction on fine grids [135], it does not explicitly construct the collision matrix of Eqn. 2.5. Instead, the mobility is computed using an iterative scheme under the cold-electron approximation [25]. We found that this iterative method was numerically unstable for the warm electron case. We instead solved the linear system using the Generalized Minimal Residual (GMRES) algorithm as implemented in the Scientific Python library [140]. The matrix was constructed by modifying PERTURBO to output the elements of Eqn. 2.5.

As described earlier in Ch. 2, the cold electron approximation that is typical in previous works presumes that $\partial \Delta f_{m\mathbf{k}}/\partial \mathbf{k} = \partial f^0_{m\mathbf{k}}/\partial \mathbf{k}$. Numerical analysis in GaAs, as shown in Fig. 2.4 has revealed that in the field range of present interest, the momentum-space derivative of the deviational occupation, $\partial \Delta f_{m\mathbf{k}}/\partial \mathbf{k}$, is large compared to $\partial f^0_{m\mathbf{k}}/\partial \mathbf{k}$. Consequently, as described in Sec. 2.4, the derivative term corresponding to particle drift in an electric field $\mathcal{E}$ is approximated by a finite difference matrix. In this treatment, boundary conditions must be applied to points that do not have a full set of first-nearest neighbors. To do so, we assume that these points have zero occupation by removing the contributions of these states to the finite difference matrix. The energy window is selected to be sufficiently large such that these boundary states indeed have negligible population, which ensures that

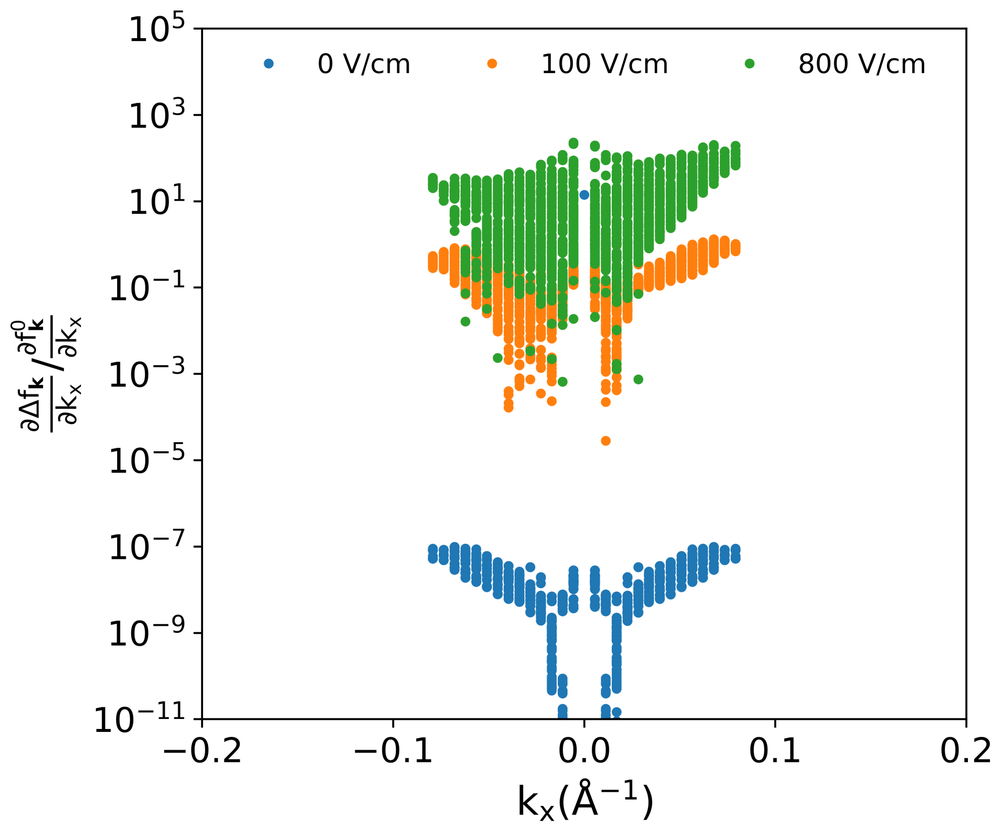

Figure 2.4: Ratio of the non-equilibrium drift operator to the equilibrium drift operator for GaAs at 300 K. The cold-electron approximation is appropriate in the range of fields for which the ratio of the operators is much smaller than one. At even modest fields such as 800 V cm^{-1}, the non-equilibrium drift operator rapidly exceeds its value in equilibrium, necessitating the warm electron-treatment applied here.

scattering induced by the collision matrix $\Theta_{m\mathbf{k}m'\mathbf{k}'}$ for these states can be neglected.

With the collision and drift matrices computed, we then construct the relaxation operator $\Lambda_{m\mathbf{k}m'\mathbf{k}'}$, Eqn. 2.10. The steady-state distribution is obtained by solving the resulting linear system given by Eqn. 2.12. We then solve Eqn. 2.26 with the inhomogenous term constructed from the previously computed steady-state distribution as input. For this second Boltzmann equation, we include an $i\omega$ term on the diagonal of the linear system which corresponds to the Fourier transformed time derivative. Finally, the spectral density is computed as a Brillouin zone integration over the distribution that solves the second Boltzmann equation. The calculation of the AC mobility proceeds in a similar way as for the steady distribution except with the addition of the $i\omega$ term.

Owing to computational limitations, we account for first-order electron-phonon (1ph) processes and neglect higher-order interactions that are reported to play a role in polar semiconductors [93]. Also, recent studies report the effect of quadrupole electron-phonon interactions on electron transport [141, 142]. In particular, the work of Ref. [142] predicted a significant correction to the mobility in GaAs limited by acoustic mode scattering. Our calculations were performed at 300 K at which the scattering is dominated by polar optical phonons, and so we neglected quadrupole interactions. Further, we ignore the effect of spin-orbit coupling, as spin-orbit interactions in silicon are weak and thus do not have a significant effect on transport properties like mobility [90]. Similarly, for our work in Si, quadrupole electron-phonon interactions were neglected, as they are reported to provide only a small correction to silicon mobility at room temperature [143].

Chapter 3

FIRST-PRINCIPLES SIMULATIONS OF NONEQUILIBRIUM ELECTRONIC FLUCTUATIONS IN GALLIUM ARSENIDE AND SILICON

This chapter has been adapted, in part, from:

1. **Choi[†], Alexander Y.**, Cheng[†], P. S., Hatanpää, B. & Minnich, A. J. Electronic noise of warm electrons in semiconductors from first principles. *Phys. Rev. Materials* **5,** 044603. https://link.aps.org/doi/10.1103/PhysRevMaterials.5.04460 (4 Apr. 2021).

   Contributions A.Y.C. wrote the Python backend for Boltzmann Transport calculations, performed the data analysis, made the paper figures, and wrote a majority of the manuscript.

2. **Choi[†], Alexander Y.**, Hatanpää[†], B., Cheng, P. S. & Minnich, A. J. Nonequilibrium transport and fluctuations of hot electrons in Si from first-principles. *In preparation.*

   Contributions A.Y.C. wrote the Python backend for Boltzmann Transport calculations, performed the initial set of calculations, performed data analysis, and wrote half the manuscript.

As described in the previous chapter, computation of electronic noise in semiconductors can provide useful information about materials that would not be available from conventional simulations of low-field transport quantities. In this chapter, we describe our calculations of both transport and fluctuation quantities using the theory outlined in the previous chapter. Our work represents a substantial advancement in *ab initio* studies of materials. In particular, we move beyond the "cold-electron" approximation typical in low-field studies and provide the first calculations of transport and spectral noise power in carriers that are heated above the lattice temperature. Further, our method provides a means to go beyond semi-empirical models for electronic noise, allowing us to identify the microscopic mechanisms responsible for electronic fluctuations in a predictive manner. By applying our method in well-studied semiconductors and comparing simulated transport and fluctuation observables to experiment, we evaluate the standard for the accepted level of theory of charge transport, bandstructure, and scattering in these materials.

We present our results in two major parts. In the first section, we apply our method to warm electrons in GaAs. Using the nonequilibrium distribution function, we calculate the warm electron DC and AC mobilities and demonstrate that the method provides good comparison to experimental measurements of the heating. By calculating the fluctuations, we show that the anisotropy and spectral features of the noise power in GaAs can be explained by the disparate timescales of momentum and energy exchange with phonons, even though scattering is dominated by the highly inelastic polar optical phonon scattering mechanism. Next, we extend the methodology to hot electrons in silicon. In contrast to single valley, direct-bandgap semiconductors such as GaAs, in multivalley semiconductors such as Si, intervalley coupling plays a strong role for even low fields. We demonstrate the ability of our method to resolve the contribution of heating and redistribution in the valleys to both high field transport and fluctuations. Our analysis indicates that the widely-accepted one-phonon approximation for the e-ph interaction is unable to reproduce measurements of the warm electron tensor in Si. This result indicates that incorporating higher-level scattering mechanisms such as two-phonon may be necessary to accurately simulate noise in Si.

3.1 Electronic transport in GaAs

Gallium arsenide (GaAs) is III-V compound semiconductor with zincblende crystal structure. As depicted in Fig. 3.1, GaAs is a direct bandgap semiconductor with a single conduction band minimum at the Γ point. To excellent approximation, the Gamma valley is spherical with effective mass $0.063 m_0$ [86]. Because of the high mobility resulting from a light conduction band minimum, GaAs is a commonly used material in high speed electronics operating at microwave frequencies [38]. Further up the conduction band, GaAs possesses eight degenerate valleys at the L point and six degenerate valleys at the X point. The large energy separation between the valleys $\Delta E_{\Gamma L} = 300$ meV and $\Delta E_{\Gamma X} = 470$ meV [145] means that at room temperature and for typical doping levels, equilibrium electrons remain mostly in the Γ valley (for 300 K and $n = 10^{16}$ cm^{-3}, over 99.9% of electrons are in Γ).

We begin this section examining the steady state distribution and associated transport observables for the cold and warm electron regimes in room temperature GaAs. Figure 3.2 plots the deviational steady state distribution functions $\Delta f_{\mathbf{k}} = f^s_{\mathbf{k}} - f^0_{\mathbf{k}}$ under the two approximations versus the wave vector parallel to the electric field, k_x. We refer to this direction as the longitudinal direction. At low fields $\mathcal{E} < 100\,\mathrm{V\,cm^{-1}}$, the cold electron approximation is accurate and the solutions are nearly identical.

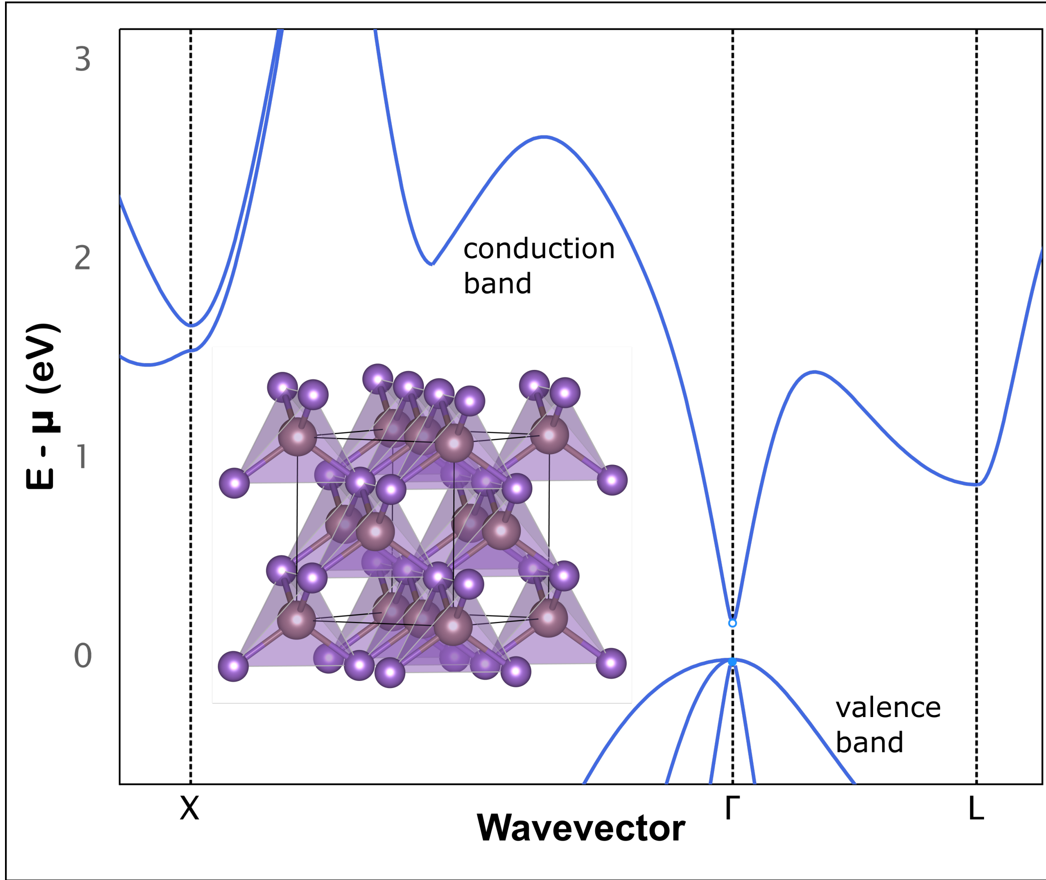

Figure 3.1: Conduction and valence band structure of GaAs with the $F\bar{4}3m$[216] Hermann Mauguin space group. **Inset:** Conventional cell of GaAs in the zincblende structure. Data generated with the Materials Project [144].

In contrast, as the field increases, differences in the distribution functions emerge. Under the cold electron approximation, Eqn. 2.12 shows that $\Delta f_{\mathbf{k}}$ is required to possess odd symmetry about the Brillouin zone center because the forcing gradient $\partial f^0_{\mathbf{k}}/\partial_{\mathbf{k}}$ is odd with respect to k_x while the scattering matrix is even ($\Theta_{\mathbf{k}\mathbf{k}'} = \Theta_{-\mathbf{k}-\mathbf{k}'}$). This symmetry is evident in the cold electron solutions at all fields in Fig. 3.2. Physically, this symmetry indicates that in the cold electron case, states with negative wavevector are depopulated to the exact same degree that the corresponding positive wavevector are filled. Since the net population does not change with energy, electrons under this approximation do not heat with the field. This is in contrast to the warm electron case, where the electronic distribution function develop asymmetrically in momentum space as the non-equilibrium gradient modeled by Eqn. 2.8 grows with the field. At $\mathcal{E} = 800\ \mathrm{V\,cm^{-1}}$, warm electrons reach comparatively high wavevector states in the direction of the field as exhibited by the momentum-space

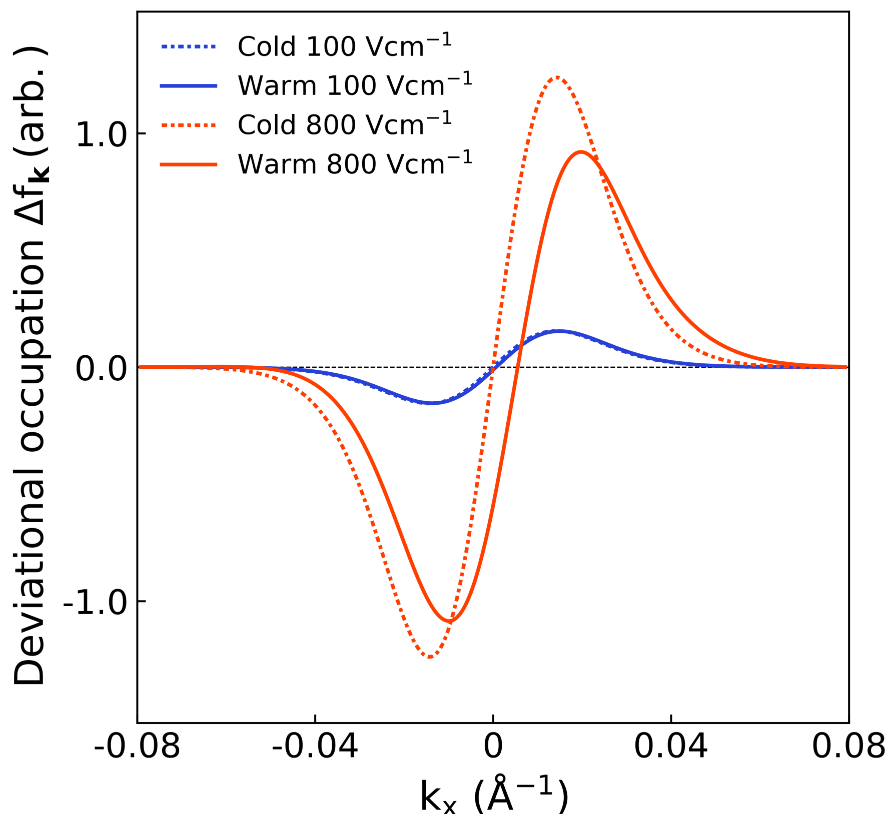

Figure 3.2: Deviational occupation Δf_k in GaAs at 300 K under the cold (dotted lines) and warm (solid lines) electron approximations versus longitudinal wave vector k_x. Curves plotted for $\mathcal{E}$ = 100 V cm^{-1} (blue), and $\mathcal{E}$ = 800 V cm^{-1} (orange). The dashed black line is a guide to the eye. At the lower field, the two approximations result in nearly identical distribution functions. At the higher field, the cold-electron approximation fails to capture the assymetrical development of the distribution function.

tail in Fig. 3.2. These electrons absorb energy from the field and are heated above the lattice temperature.

The transport properties of the warm electron distribution differ from those of the cold distribution because warm electrons in the high momentum, high energy tail are able to emit optical phonons and hence exhibit higher scattering rates. As reported previously [92], the predicted mobility of GaAs exceeds the experimental mobility owing to the exclusion of higher-order phonon scattering processes and the lower calculated effective mass (0.055 m_0) compared to experiment (0.067 m_0) [93].

Therefore, to facilitate comparison, we examine the DC mobility normalized by its low-field value in Fig. 3.3. The low-field value of the computed mobility is 17,420

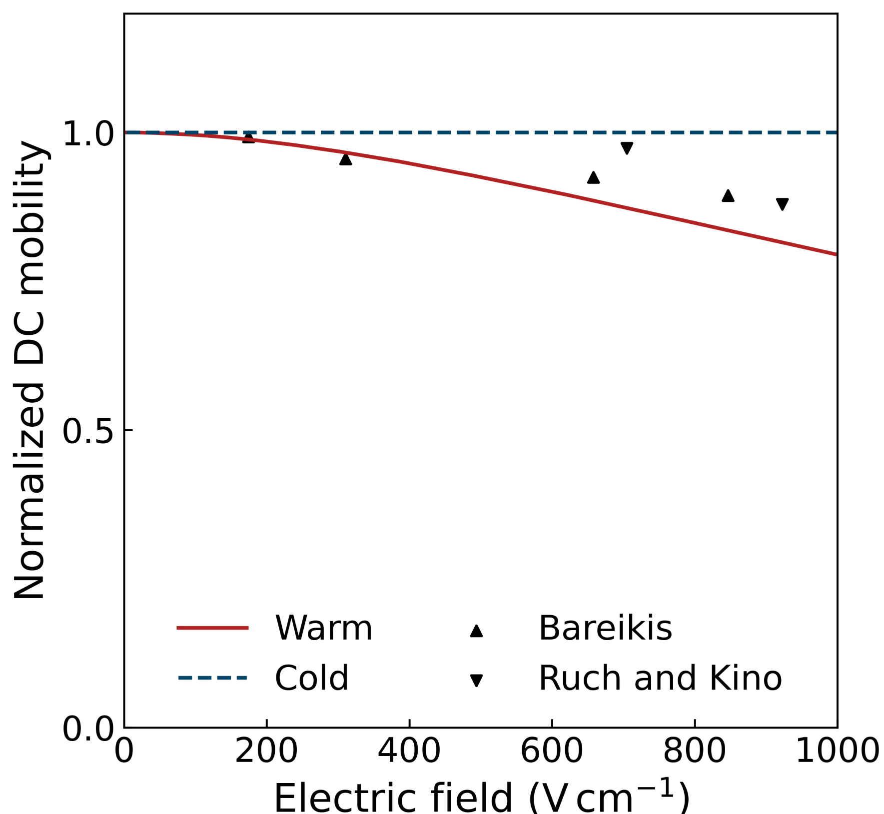

Figure 3.3: Normalized longitudinal (∥) DC mobility versus electric field of the cold (dashed blue line) and warm electrons (solid red line). The heating of the electrons leads to a decreased mobility. The trend of the normalized mobility agrees well with experiments: Figure 1, Ref. [146] (Upward black triangles) and Figure 4, Ref. [147] (Downward black triangles).

cm^2 V^{-1} s^{-1}. At low fields $\mathcal{E} < 100$ V cm^{-1}, the mobility under the warm and cold electron approximations agrees to within 1%. At higher fields $\mathcal{E} = 800$ V cm^{-1}, the DC mobility of the warm electrons has decreased by more than 10%. This behavior is qualitatively consistent with the sublinear current voltage characteristic (CVC) of n-type GaAs [38], or a decrease in mobility with increasing electron temperature caused by a concomitant increase in the average scattering rate. The field dependence of the normalized mobility shows favorable comparison to experiment, implying that our calculation is properly capturing the heating with the field.

In addition to steady quantities, the small-signal AC mobility can be computed as in Eqn. 2.17. Figure 3.4 presents the small-signal AC mobility for the warm electron gas versus frequency for several electric fields. At zero frequency, the equilibrium AC mobility is equal to the equilibrium DC mobility, as expected. The decrease of

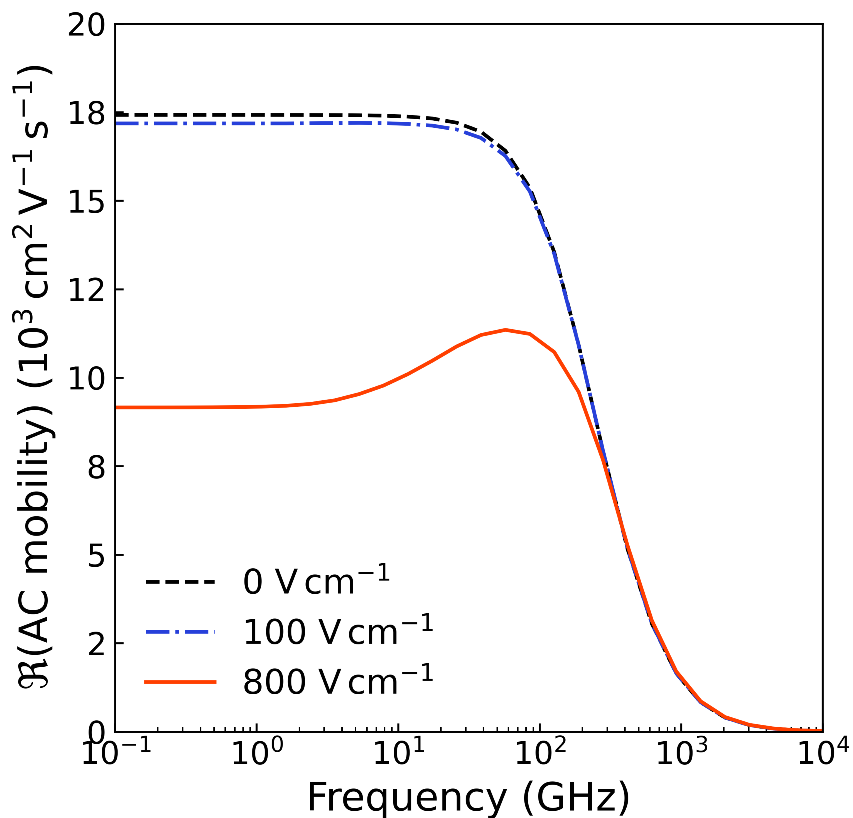

Figure 3.4: Real part of the longitudinal small-signal AC mobility versus frequency for equilibrium (dashed black line), $\mathcal{E}$ = 100 V cm^{-1} (dash-dot blue line), and $\mathcal{E}$ = 800 V cm^{-1} (solid orange line) under the warm electron approximation. The AC mobility exhibits spectral features at frequencies that are characteristic of the inverse momentum and energy relaxation times (see Section 3.3).

the AC mobility with electric field is also consistent with the trend observed in the DC mobility. At $f \sim 1$ THz, the AC field frequency exceeds the phonon-mediated scattering rates which redistribute the electrons in response to the field, and thus the AC mobility rolls off at all fields. This result reflects the electrical response transitioning from a purely resistive to a purely reactive regime as the frequency exceeds the highest scattering rates.

The frequency dependence of the AC mobility indicates the relevant timescales of momentum and energy relaxation [148]. In particular, for 800 V cm^{-1}, we observe a lower value of the AC mobility at low frequency, followed by a maximum at around 100 GHz. This feature is due to energy exchange with phonons and will be discussed in Section 3.3.

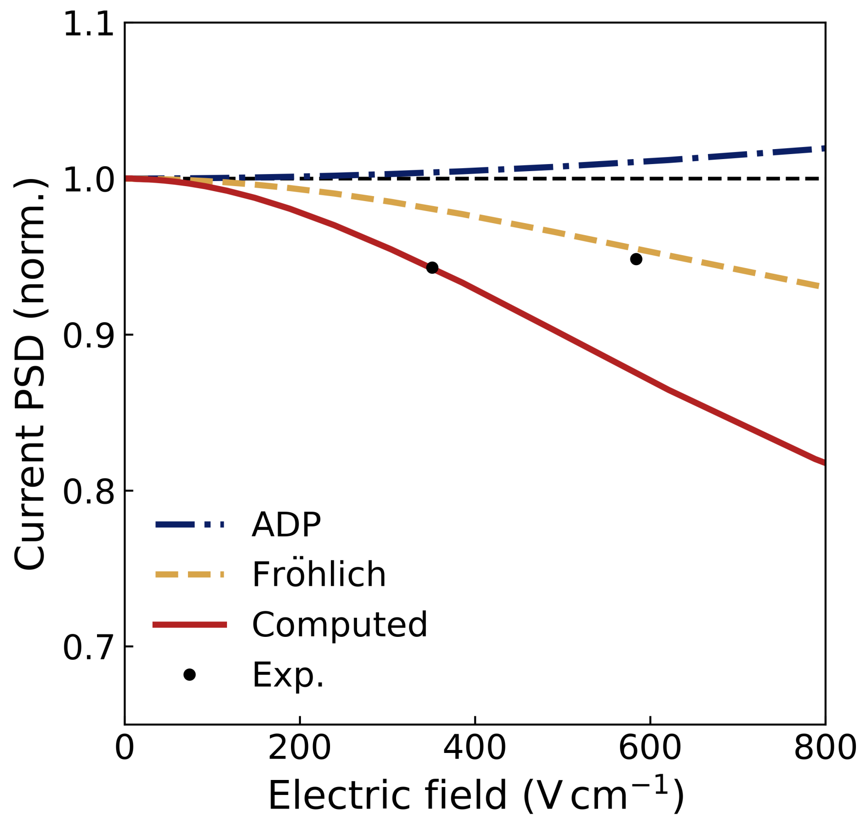

Figure 3.5: Spectral density of longitudinal current density fluctuations (solid red line) normalized to the Nyquist value versus electric field along with Davydov spectral densities calculated using an acoustic deformation potential (ADP) (dash-dot blue line) and Fröhlich (dashed yellow line). At equilibrium, the noise agrees with Nyquist-Johnson noise (dotted black line). The *ab initio* calculation predicts a steeper decrease in current PSD with field compared to the approximations. The symbols correspond to experimental measurements (Figure 11, Ref. [149]).

3.2 Diffusion noise in GaAs

We now calculate the spectral density of current fluctuations from the non-equilibrium steady state in GaAs. Figure 3.5 shows the spectral density of longitudinal current fluctuations versus electric field at an observation frequency of 1 MHz, far smaller than any scattering rate. At equilibrium, the noise is given by the Nyquist relation, Eqn. 2.30. It is conventional to report the spectral density normalized to the Nyqist value to allow comparison between samples of different carrier density, and we follow this convention here [98].

As the electric field increases, the computed noise decreases below the Nyquist value. Few experimental studies of noise in GaAs cover the fields of present interest, but

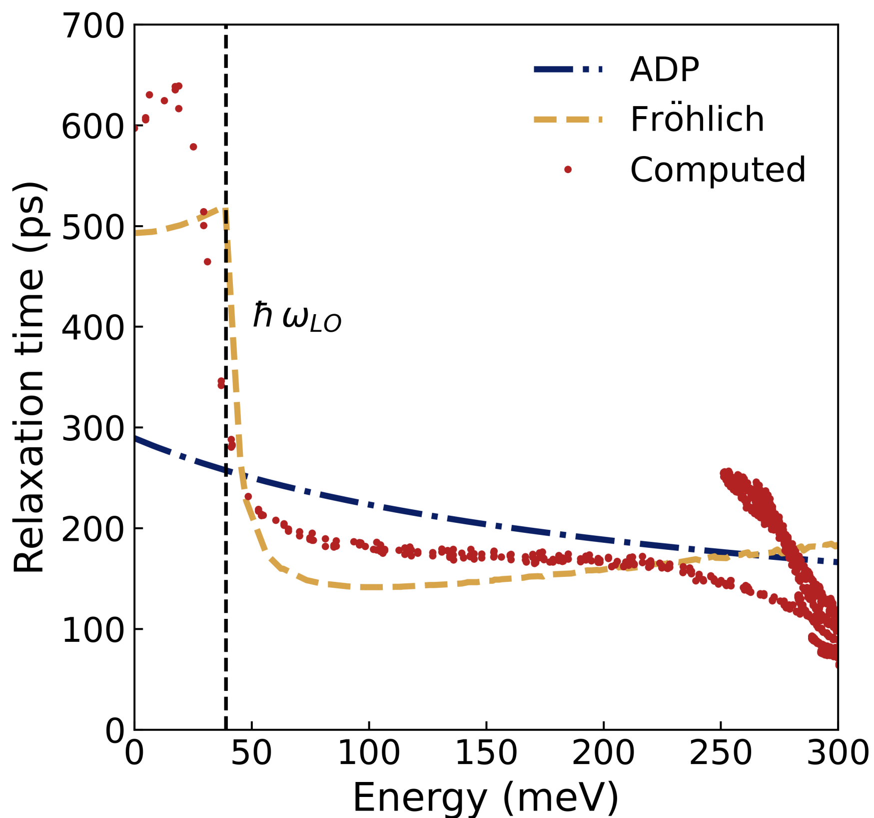

Figure 3.6: Relaxation time versus energy above conduction band minimum for GaAs at 300 K using ADP (dash-dot blue line), Fröhlich potential (dashed yellow line), and computed (red circles). The energy of the zone-center LO phonon is shown for reference (dashed black line). The qualitative agreement between the Fröhlich and computed first-principles relaxation times is an indication of the dominance of the LO phonon mode in GaAs at room temperature.

reasonable agreement is observed with measurements by Bareikis *et al.* [149]. We note that a decrease with field is observed in other studies in GaAs [146, 150] though the sparsity of data in the relevant electric field range prevents direct comparison.

To better understand the decreasing trend, we use an approximate solution of the Boltzmann equation for an electron gas interacting quasi-elastically with a thermal phonon bath [5, 151]. Under the quasi-elastic approximation, the distribution function is expanded in momentum space using Legendre polynomials. Because the distribution is nearly isotropic in momentum space under quasi-elastic scattering, only the two lowest Legendre polynomials need be retained [152]. The zeroth-order term gives the occupancy versus energy and is known as the Davydov distribution.

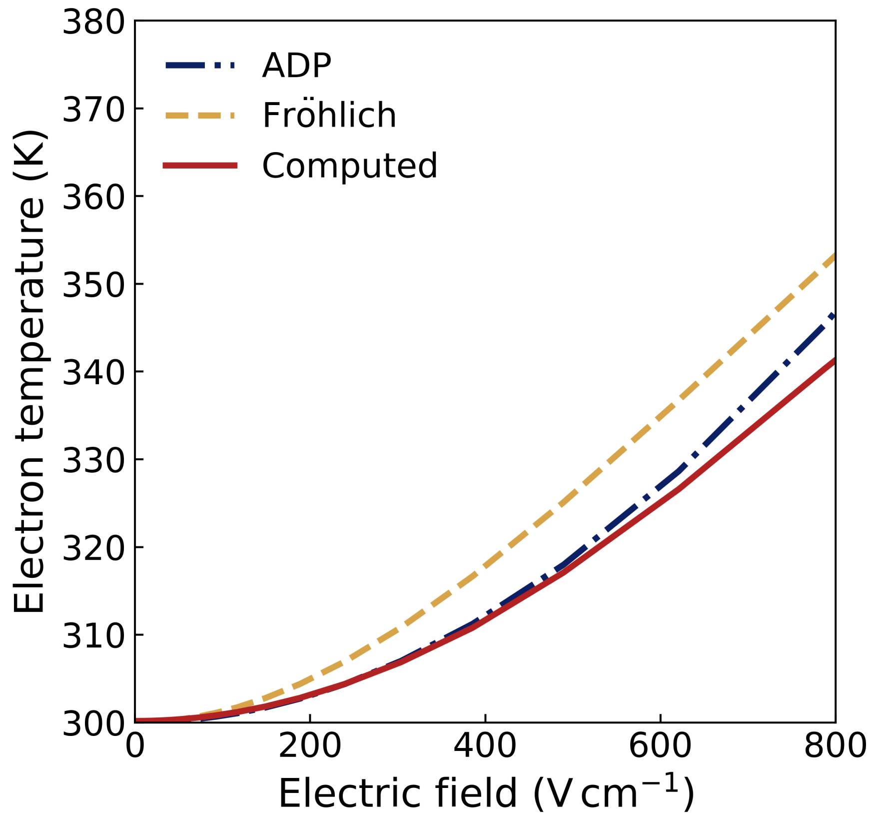

Figure 3.7: Effective electron gas temperature versus electric field for ADP (dash-dot blue line), Fröhlich (dashed yellow line), and computed (solid red line). The magnitude of electron heating is similar among the various calculations, indicating that heating alone cannot be responsible for the disparity in the power spectral density.

The Davydov distribution can be expressed in terms of an integral equation:

$$F_\epsilon = A \exp\left[- \int_0^\epsilon \frac{d\epsilon'}{k_B T_0 + 2e^2 \mathcal{E}^2 \tau_{\epsilon'} \tau_{\epsilon'}^{en} / 3m^*} \right] \tag{3.1}$$

where A is a normalizing factor for the particle number and m^* is the effective mass. The Davydov model is parametrized by the energy dependence of the momentum and energy relaxation times, τ and τ_ϵ, respectively, and the inelasticity ratio τ/τ_ϵ [38]. Once these parameters are specified, the Davydov distribution can be computed and used with Eqn. 2.26 to calculate the PSD of current fluctuations [4]. The Davydov distribution can be analytically expressed if the relaxation times exhibit simple energy dependencies such as a power law-dependence on the carrier energy [153].

For $\tau_\epsilon = P_a \epsilon^{-0.5}$ and $\tau_\epsilon^{en} = P_b \epsilon^{-0.5}$ the distribution is:

$$F_\epsilon = A \exp\left[-\frac{3\, m\, \epsilon^2}{4\, P_a\, P_b\, e^2\, \mathcal{E}^2}\, {}_2F_1\left(1, 2, 3, \frac{-3\, \epsilon\, k_B T_0\, m}{2\, P_a\, P_b\, e^2\, \mathcal{E}^2}\right)\right] \tag{3.2}$$

where ${}_2F_1$ is the Gauss Hypergeometric function. On the other hand, if the energy and momentum relaxation times are constants with respect to energy, we obtain the heated Maxwellian.

$$F_\epsilon = A \exp\left[\frac{-\epsilon}{k_B T + 2\, P_a\, P_b\, e^2\, \mathcal{E}^2 / 3\, m}\right]. \tag{3.3}$$

For the present study, we choose to use more physically motivated models of the relaxation time as comparisons to the real *ab initio* calculations. Approximate analytic expressions for the electron relaxation times in semiconductors are available in the literature [86]. Previous works have calculated the Davydov distribution for a power-law energy dependence of the relaxation times such as that from the acoustic deformation potential (ADP) [154–156]. For scattering mediated by an acoustic deformation potential D_A, the relaxation times can be expressed as:

$$\tau^{-1} = \frac{\pi D_A^2 k_B T}{\hbar c_l} g_c(\epsilon) = \frac{\sqrt{2m^3} D_A^2 k_B T}{\pi \hbar^4 c_l} \sqrt{\epsilon} \tag{3.4}$$

where c_l is the elastic constant and g_c is the density of states.

Although Eqn. 3.4 can provide a reasonable approximation to acoustic modes, studies have established that for polar materials such GaAs at room temperature, the long-ranged Fröhlich interaction with longitudinal optical (LO) phonons is the dominant scattering mechanism [34, 92]. A suitable expression for the relaxation times associated with the LO mode can be obtained through the Fröhlich approximation:

$$\tau^{-1} = \tau_0^{-1} \sqrt{\frac{\hbar\, \omega_0}{\epsilon}} \left[N_0 \operatorname{arcsinh}\left(\sqrt{\frac{\epsilon}{\hbar\, \omega_0}}\right) + (N_0 + 1) \operatorname{arcsinh}\left(\sqrt{\frac{\epsilon}{\hbar\, \omega_0} - 1}\right)\right] \tag{3.5}$$

where $\hbar\, \omega_0$ is the optical phonon energy, N_0 is the thermal occupation of the optical phonon, and τ_0^{-1} is the inverse Frölich time. Note that the second term in the sum of Eqn. 3.5 describes the relaxation times for states with energy above the threshold for LO emission $\hbar\omega_0$.

In Fig. 3.5, we compare the *ab initio* longitudinal spectral density to that predicted using the Davydov distribution with both the ADP and Fröhlich scattering rates. In both of these approximations, the relaxation times have been scaled such that the distributions produce the same low-field mobility as the full computed solution, and the inelasticity ratio has been selected using an estimation of the energy and momentum relaxation times (see Fig. 3.9 and Fig. 3.10). The spectral density from the full simulation is observed to decrease monotonically with the electric field. This decrease is captured qualitatively by the Fröhlich calculation. In contrast, the ADP noise increases monotonically with field.

These trends can be understood in terms of the differing energy dependencies of the relaxation times under the various approximations. Figure 3.6 shows the phonon-mediated relaxation times versus energy for electrons in GaAs at 300 K for the three cases. Below the zone-center LO phonon energy $\hbar\omega_{LO} \sim 35$ meV, the computed relaxation times are set by LO phonon absorption [92]. Above the LO phonon energy, LO emission becomes dominant and the relaxation times sharply decrease to a value that remains roughly constant until electron energies are near the L-valley minimum at ~ 0.25 eV above the CBM. As one would expect, this absorption-to-emission transition is qualitatively captured by the Fröhlich approximation. The ADP relaxation times agree reasonably well with the computed relaxation times in the emission-dominated region but clearly do not exhibit the absorption-to-emission transition.

The electric field dependence of the spectral noise power reflects the balance between the growth of scattering rates with electron energy and the heating of the electron gas by the DC field [157]. To understand this balance, we examine the effective electron temperature of the steady distribution for the three cases in Figure 3.7. The energy density of the non-equilibrium distribution is defined as a Brillouin zone sum over the distribution:

$$\langle \epsilon \rangle = \frac{1}{\mathcal{V}_0} \sum_{\mathbf{k}} \epsilon_{\mathbf{k}} f^s_{\mathbf{k}}. \tag{3.6}$$

The effective electron temperature is calculated as the temperature of a Maxwell-Boltzmann distribution that yields the same energy density as the steady non-equilibrium distribution. At low fields $\mathcal{E} < 100$ V cm^{-1}, the temperature is equal to the lattice temperature. As the electric field increases, the effective temperature increases, corresponding to occupancy at higher energies and increased scattering

rates. Near equilibrium where the mobilities are equivalent, the temperature rise predicted from each approximation is similar, but at higher fields, the *ab initio* calculation predicts a slightly lower temperature than do either the ADP or Fröhlich approximations, indicating a stronger energy coupling between charge carriers and the lattice.

As the electron gas heats, higher energy states are occupied and thus the spectral noise power, Eqn. 2.26, includes contributions from fluctuations in those states; hence, the spectral noise power may increase on heating. On the other hand, at these high energies, the scattering events which damp out fluctuations are more frequent, tending to decrease the noise. The competition between these mechanisms sets the trends shown in Figure 3.5. By calculating the spectral densities produced by the acoustic deformation and Fröhlich potentials, we have the ability to directly assess the impact of heating and scattering. For both Fröhlich and the present calculations, the sharp increase in scattering rates associated with the absorption-to-emission transition dominates, and the spectral density decreases monotonically with electric field. In contrast, the ADP approximation shows increasing noise with electric field as the heating of the electrons dominates the weak increase of the scattering rates.

The evolution of the spectral density with electric field demonstrates the sensitivity of the spectral noise power to the energy dependence of the scattering rates. Although the mobility at equilibrium is equivalent for all three cases, the non-equilibrium noise behavior exhibits qualitatively different trends depending on the energy dependence and inelasticity of the scattering mechanisms. This sensitivity illustrates that a rigorous treatment of the electron-phonon interactions is necessary to produce accurate simulations of fluctuations in GaAs.

Another powerful utility of our method is the ability to differentiate the contribution of individual electronic states to the overall noise. Figure 3.8a shows the state-by-state decomposition of the DC longitudinal spectral density against the longitudinal group velocity for different values of the electric field. The plotted quantity represents the contribution of a given state to the spectral density, which is obtainable as a state-labeled vector by omitting the sum over $\mathbf{k}$ in Eqn. 2.26. The features of the two curves in the figure can be understood as a balance between competing mechanisms that set the noise. Two characteristics determine the contribution of a state to the current spectral density. The first contributing factor is the occupation of the state, specified by the distribution function. A higher occupation of electrons in a given state increases the number of fluctuations out of the state and augments the noise.

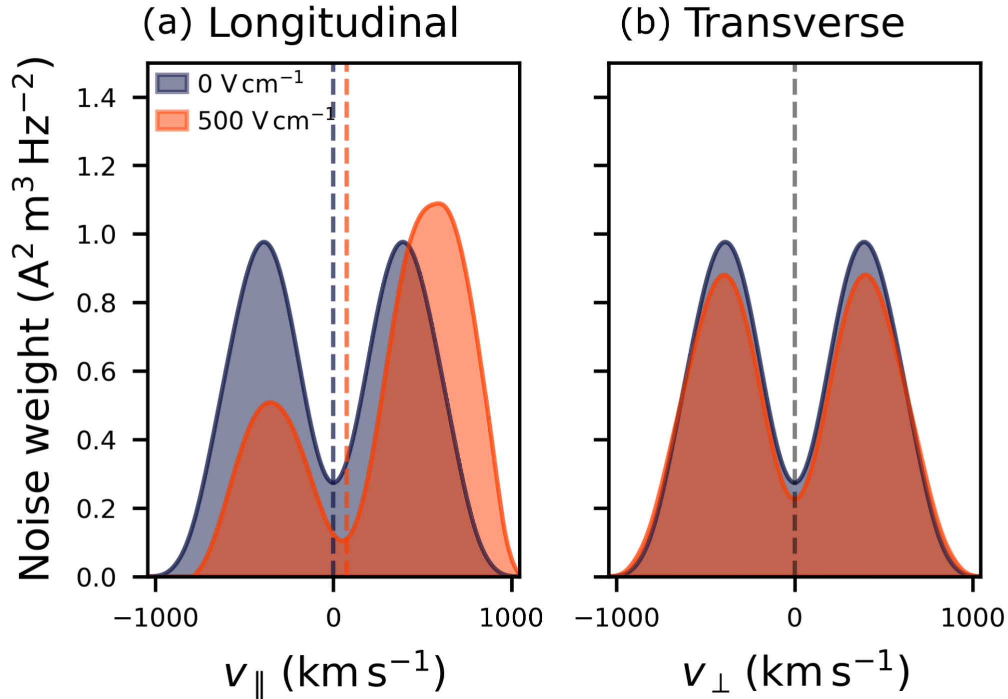

Figure 3.8: Kernel density estimate of the state-wise contribution to the (a) longitudinal and (b) transverse current spectral density as a function of the group velocity at equilibrium (blue volumes) and at 500 V cm^{-1} (red volumes). The noise contribution of each state is determined by the occupation and the magnitude of the induced fluctuation. The drift velocity in either the longitudinal or transverse directions are shown as dashed lines.

The second contributing factor is the magnitude of the current fluctuation induced by a fluctuation in the state, specified by the difference between the longitudinal group velocity and the drift velocity, $|v_\parallel - V_\parallel|$.

At the highest group velocity states $|v_\parallel| > 1000$ km s^{-1}, the occupation is negligible in the warm electron regime. In equilibrium, the low occupancy of these high momentum states limits the contribution to the noise. However, as the field increases, electrons shift from low energy states to the same high velocity, high momentum tail observed in Fig. 3.2. Consequently at 500 V cm^{-1}, states near $v_\parallel = 1000$ km s^{-1} contribute more to the noise. In contrast, the noise contribution to the transverse spectral density shown in Fig. 3.8b remains symmetric in the transverse direction to the field, since there is no redistribution of the population transversely. The maxima in both plots represent the optimal balance of relatively high occupancy and large velocity deviation $|v_{\parallel,\perp} - V_{\parallel,\perp}|$.

3.3 Spectral noise power in GaAs

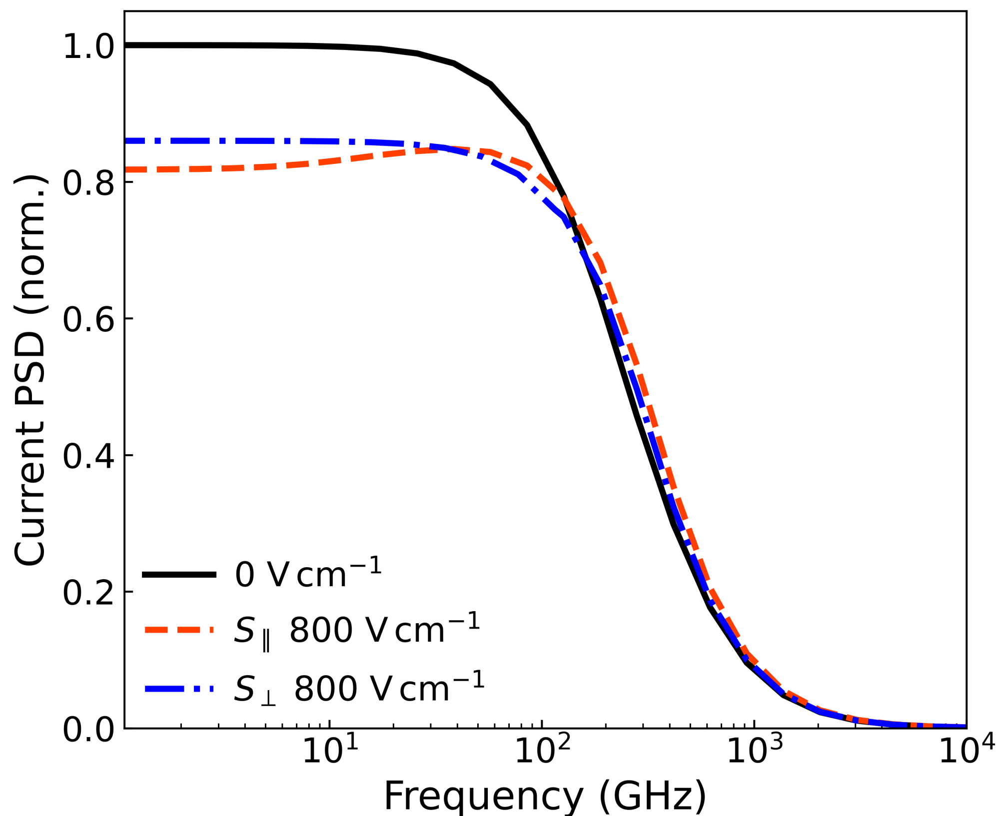

Figure 3.9: Computed power spectral density (PSD) of longitudinal (∥, dashed orange line) and transverse (⊥, dashed-dotted blue line) current density fluctuations versus frequency at $\mathcal{E}$ = 800 V cm^{-1}, along with the Nyquist-Johnson prediction for $\mathcal{E}$ = 0 (solid black line). In contrast to equilibrium, the non-equilibrium spectral densities exhibit an energy-dependent time scale that manifests as anisotropy between the longitudinal and transverse PSDs.

The non-equilibrium noise exhibits spectral features that are not present in the Nyquist-Johnson case. Figure 3.9 shows the spectral density of longitudinal (L) and transverse (T) current fluctuations (relative to the electric field axis) versus frequency at $\mathcal{E}$ = 800 V cm^{-1}. There are several notable features of the spectral density in this figure. First, the spectral density is constant at low frequencies and rolls off as frequency increases, decreasing to 50% of its low frequency value at 300 GHz. Secondly, an anisotropy exists between the longitudinal and transverse spectral densities in terms of both the magnitude and the frequency dependence. In both cases, the spectral density at low frequencies is suppressed relative to the equilibrium value. Finally, the longitudinal noise exhibits a non-monotonic trend

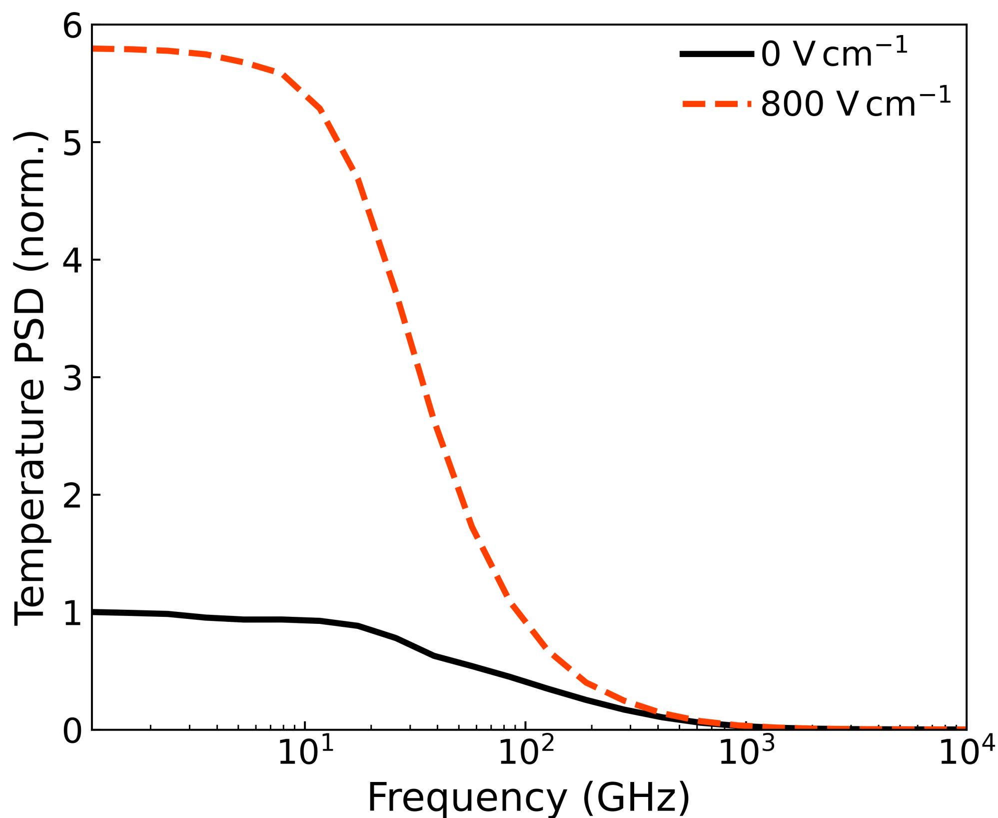

Figure 3.10: Spectral density of energy fluctuations versus frequency at equilibrium (solid black line), $\mathcal{E}$ = 800 V cm^{-1} (dashed orange line). The time scale for electron temperature fluctuations sets the upper frequency limit for the convective mechanism.

for frequencies around 50 GHz, similar to that observed for the AC mobility in Fig. 3.4. Spectroscopic measurements of the noise power at these frequencies have not been performed, but these trends are qualitatively similar to those observed in recent Monte Carlo simulations [131].

We discuss each of these points in turn. Consider first the noise at equilibrium. The zero-field curve shows that the longitudinal and transverse spectral densities are identical and coincide with the Nyquist-Johnson value, Eqn. 2.30, as one would expect for an isotropic material in thermal equilibrium. As with the AC mobility, the spectral density rolls off at frequencies exceeding the phonon-mediated scattering rates because the electronic system cannot redistribute in response to the fluctuation at such high frequencies. This roll-off behavior has been noted previously [87] and has also been observed for phonon thermal conductivity (see Fig. 1b in Ref. [158]).

Now consider the noise with $\mathcal{E} = 800\ \mathrm{V\,cm^{-1}}$. A similar roll-off with increasing frequency as the equilibrium case is observed. At low frequency, both the longitudinal and transverse spectral densities are lower than the Nyquist value because of the increased electron temperature and the correspondingly lower mobility that is observed in Fig. 3.3. However, an anisotropy exists in the spectral densities. The origin of this feature is the 'convective' mechanism [5, 13, 38] and can be understood by decomposing the non-equilibrium current fluctuations into two sources. The first source is the fluctuation of the drift velocity, induced by stochastic transitions between states of differing group velocity. The second source is the fluctuation of the electron temperature, induced by random energy exchange with the thermal phonon bath. These fluctuations are present, but uncoupled in the equilibrium case. In contrast, under non-equilibrium conditions, these fluctuations couple as the current drives the energy exchange with the lattice. When the electron gas is heated by the applied electric field, fluctuations in the current induce variations in the Joule heating. The resulting electron temperature fluctuations change the conductivity, which in turn modifies the current in a positive feedback loop. This coupling only exists for fluctuations longitudinal to the electric field because fluctuations transverse to the field do not produce a mean current and consequently do not affect Joule heating. In sublinear CVC materials such as GaAs, the conductivity decreases with electron temperature, and the convective mechanism suppresses longitudinal fluctuations. This feature is indeed observed in Fig. 3.9.

The convective mechanism is only present at frequencies $\omega\tau_\epsilon \ll 1$, where τ_ϵ is the energy relaxation time. As discussed above, the local maxima from the convective contribution appears at the timescale of the energy relaxation $\omega\tau_\epsilon = 1$ in the longitudinal direction (see Ref. [38], Chapter 7). The energy relaxation time can also be directly extracted by calculating the spectral density of electron temperature fluctuations versus frequency.

$$S_{\delta T_e \delta T_e}(\omega) = 2\left(\frac{2ek_B}{\mathcal{V}_0}\right)^2 \Re\left[\sum_{\mathbf{k}} \epsilon_{\mathbf{k}} \sum_{\mathbf{k}'} (i\omega\,\mathbb{I} + \Lambda)^{-1}_{\mathbf{k}\mathbf{k}'} \sum_{\mathbf{k}_1} \epsilon_{\mathbf{k}_1}\left(f^s_{\mathbf{k}'}\delta_{\mathbf{k}'\mathbf{k}_1} - \frac{f^s_{\mathbf{k}'} f^s_{\mathbf{k}_1}}{N}\right)\right] \tag{3.7}$$

This calculation is the energy analogue of Eqn. 2.26, where the relevant state quantity is the energy instead of the group velocity. Figure 3.10 shows the spectral density of energy fluctuations versus frequency for several electric fields. At low frequencies, $f < 10\,\mathrm{GHz}$, the spectral density increases with field as the temperature

fluctuations rise with higher current and the resulting increase in the Joule heating. At higher frequencies, $f \sim 50$ GHz, the energy fluctuations decrease to 50% of their low frequency values and begin to converge for the two fields shown. This convergence signifies that the temperature of the electron gas cannot change sufficiently rapidly due to its finite thermal capacitance. Consequently, above these frequencies the convective noise mechanism is removed and the anisotropy of the densities in Fig. 3.9 also disappears; the longitudinal and transverse spectral densities converge. The same convective mechanism described here is also responsible for the non-monotonic trend of the AC mobility seen in Fig. 3.4.

3.4 Quasi-elastic scattering in GaAs

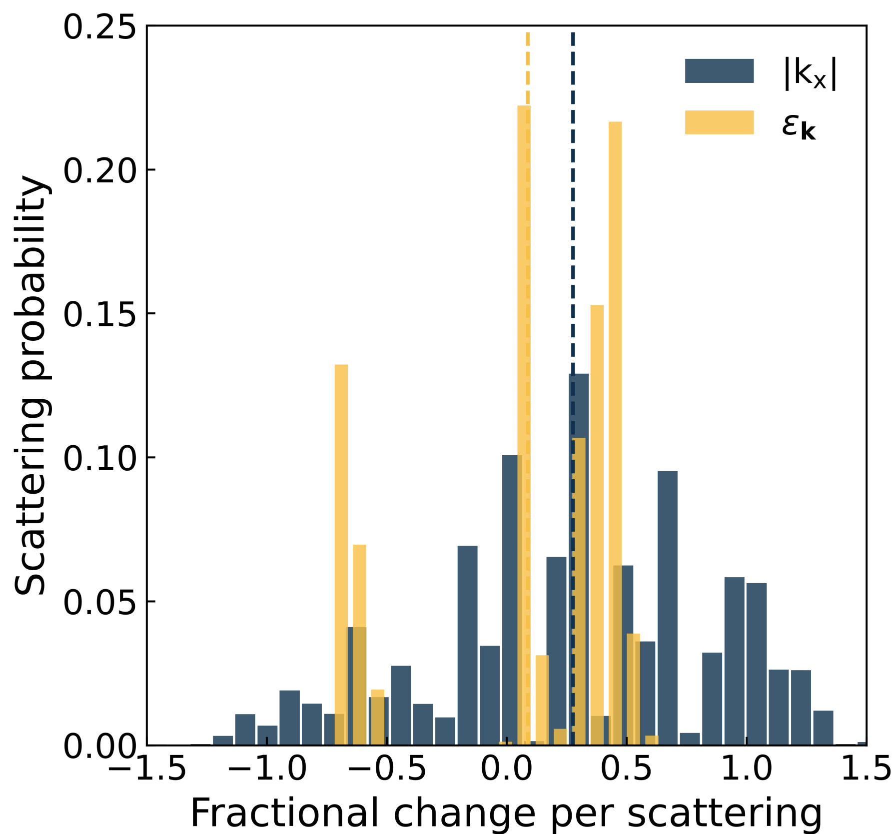

Figure 3.11: Probability histograms of longitudinal momentum loss $R_{\mathbf{k}}$ (blue bars) and energy loss $R_{\epsilon_{\mathbf{k}}}$ (yellow bars) normalized by the thermal averages at 800 V cm^{-1}. The dashed lines represent the average transfer per scattering event. At this field, the average fractional dissipation of longitudinal momentum is $\sim 3\times$ larger than that for energy.

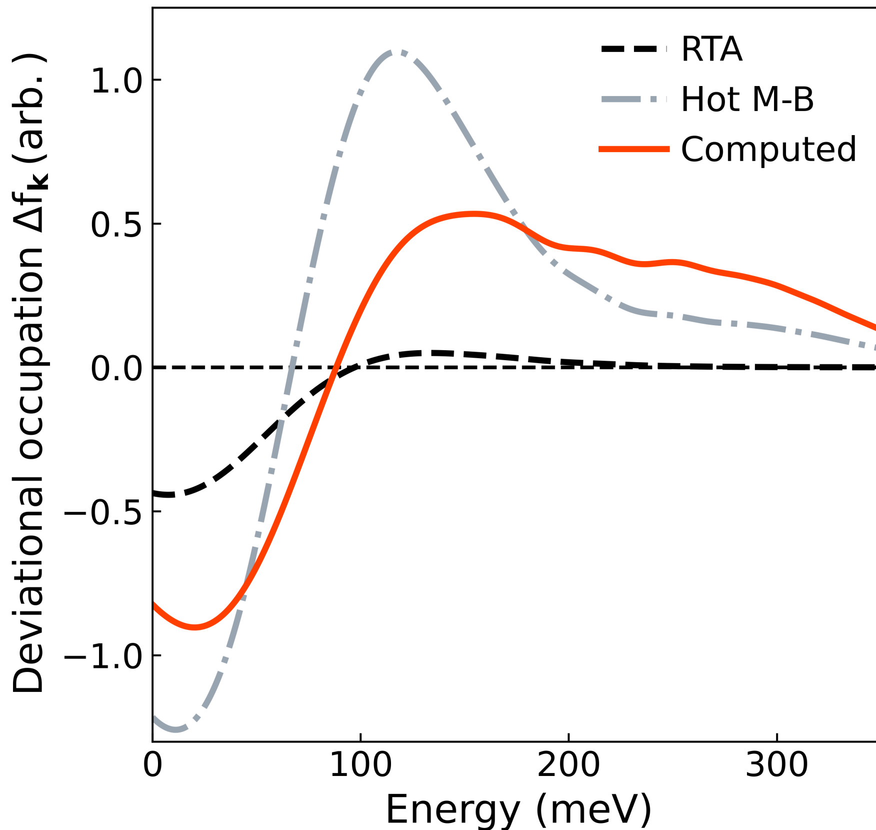

Figure 3.12: Deviational occupation $\Delta f_{\mathbf{k}}$ in GaAs at 300 K versus energy calculated under the RTA (dashed black line), hot Maxwell-Boltzmann (dashed-dotted grey line), and *ab initio* warm electron approximation (solid orange line) at 800 V cm^{-1}. The dashed black line is added as a guide to the eye. Neither the RTA nor the Maxwell-Boltzmann capture the hot electron tail.

In previous sections in this chapter, we have seen how the present formalism for electronic noise permits the study of the microscopic processes responsible for electronic noise in a manner that is difficult to obtain by other methods. In addition to information about timescales, our method can be applied to provide an explicit link between individual microscopic processes and the energy and momentum coupling in the system. As an example, consider the spectral features present in Figs. 3.9 and 3.10. Comparing the frequency where the current power spectral density and energy power spectral density reach half of their low frequency values (300 GHz versus 50 GHz, respectively), the energy relaxation time is inferred to be around 6 times longer than the momentum relaxation time, implying that the quasi-elastic assumption is valid. This observation is surprising given the well-known dominance of high-energy LO phonon emission in GaAs [92] and that inelasticity is expected only when

the physical temperature is comparable to the Debye temperature [87]. Analytical treatments of noise under dominant LO phonon coupling typically assume strongly inelastic interactions between the electrons and lattice (see Sec. 3.8 of Ref. [5], Sec. 7.3 of Ref. [38], or Ref. [159]).

We identify the origin of this discrepancy by examining how individual scattering events contribute to the momentum and energy relaxation of the electron system to the phonons. These transfers can be expressed as sums over each of the electron-phonon scattering processes in the collision integral weighted by the energy and momentum of the mediating phonon. Every electronic state in the BZ is coupled via phonons to other states; by summing over all possible scattering processes, we obtain the average energy and momentum exchanged in a single scattering event for every state in the BZ. More precisely, the state-wise fractional change in momentum is calculated as:

$$R_{k_x} = \frac{1}{\Theta_{\mathbf{kk}}\langle|k_x|\rangle}\sum_{\mathbf{k}'}\Delta k_x\,\Theta_{\mathbf{k}'\mathbf{k}} \tag{3.8}$$

and the fractional change in energy as:

$$R_{\epsilon_{\mathbf{k}}} = \frac{1}{\Theta_{\mathbf{kk}}\langle|\epsilon_{\mathbf{k}}|\rangle}\sum_{\mathbf{k}'}\Delta \epsilon_{\mathbf{k}}\,\Theta_{\mathbf{k}'\mathbf{k}} \tag{3.9}$$

where $\Delta x = x - x'$ is the difference in the state quantity k_x or $\epsilon_{\mathbf{k}}$ between $\mathbf{k}$ and $\mathbf{k}'$. $\langle|x|\rangle$ denotes the magnitude of the thermal average of the relevant quantity; $\Theta_{\mathbf{k}'\mathbf{k}}$ represents the component of the diagonal element of the collision matrix (the scattering rate) corresponding to scattering from $\mathbf{k}$ to $\mathbf{k}'$; and other variables carry the same meaning as defined in Section 2.4.

The state-wise fractional changes in the momentum and energy at 800 V cm^{-1} are plotted as a probability histogram in Fig. 3.11. In this figure, we have binned each electronic state in the BZ by the value of $R_{\mathbf{k}}$ and $R_{\epsilon_{\mathbf{k}}}$. For all the states in a given bin, we calculate the probability of scattering in a unit time interval $\mathcal{P} \propto \sum_{\text{bin}} \Theta_{\mathbf{kk}} f^s_{m\mathbf{k}}$ (the final quantity is normalized to unity). In this figure, the x-axis indicates the average fractional change in energy or momentum induced by the scattering event. Positive values of the fractional change correspond to net transfers of energy or momentum to the lattice, or dissipation, while negative values correspond to net transfers from the lattice to the electrons, or accumulation. The height of a given

bar represents the population-weighted probability of scattering in the given time interval.

Figure 3.11 reveals several features. First, energy transfers are clustered into two groups. The grouping of accumulation events around -0.75 corresponds to the ~ 35 meV energy gain associated with the absorption of LO phonons. These absorption events constitute the dominant form of scattering for electrons below the emission threshold $\hbar\omega_{LO}$. At energies above the threshold, a relatively disperse grouping of the dissipation events reflects a balance between LO emission and absorption for high energy electronic states. Second, in contrast to energy transfers, momentum transfers grow with the wave vector of the mediating phonon. Consequently, a broader and more disperse distribution of momentum transfers is available compared to energy. Finally, the net balance between dissipation and accumulation differs between energy and momentum. In equilibrium, these processes are of course precisely balanced, but at 800 $\mathrm{V\,cm^{-1}}$, the net transfers for both quantities are dissipative as the warm electrons transfer excess momentum and energy from the field to the lattice. The dashed lines in the figure represent the average transfer per scattering event and indicate that the net momentum dissipation exceeds the energy dissipation by around a factor of 3. This imbalance is partly responsible for the disparate time scales of energy and momentum relaxation observed in Figs. 3.9 and 3.10.

The second contributing factor to the relatively long energy relaxation time in room temperature GaAs is the presence of a hot electron tail in the calculated distribution. In Fig. 3.12, we plot the steady deviational distribution, Δf_s, calculated under the warm electron approximation using the full *e*-ph scattering matrix versus energy. For reference, we also calculate the corresponding distributions for a hot Maxwell-Boltzmann distribution at the non-equilibrium electron temperature and a 'relaxation-time distribution' obtained under the warm electron approximation with only the on-diagonal elements of the scattering matrix. The *ab initio* treatment predicts a hot electron tail that is not observed with either approximate method. Although representing only a small fraction of the population, these hot electrons are at energies $5-10\times$ the thermal average value. Consequently, many scattering events are needed to return these electrons to equilibrium, and the correspondingly the energy relaxation times associated with these processes are long. The result is that the quasi-elastic approximation is unexpectedly accurate in room temperature GaAs despite the inelastic nature of optical phonon scattering, thus explaining the features in the spectral noise power and AC mobility.

3.5 Hot electron phenomena in multivalley semiconductors

In the previous section, we have described the application of the method developed in Chapter 2 to GaAs. In many ways, this application represents the simplest implementation of the theory. GaAs is a direct bandgap semiconductor with cubic symmetry. Under the warm electron constraint, carriers in GaAs are primarily confined to the Γ valley at the conduction band minima which is isotropic and spherical to excellent approximation. In single-valley materials such as GaAs, the principle effect of the electric field is to raise the average energy of carriers by heating, which biases the occupancy in k-space towards the direction of the field and increases the interaction with the lattice.

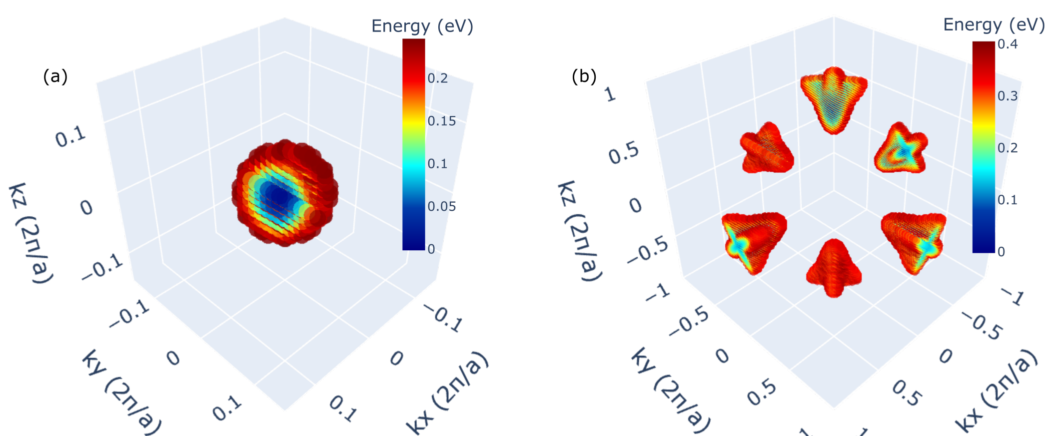

Figure 3.13: Valley structure of the conduction band minima of (a) GaAs and (b) Si plotted in Cartesian momentm space coordinates. Color indicates state energy above the conduction band minimum. While GaAs is characterized by a single spherical band at the Γ point, Si possesses six equivalent ellipsoidal bands in the ⟨100⟩. When Si is heated by an electric field, the redistribution of electrons among the six valleys causes anisotropy in macroscopic observables such as the electrical conductivity and power spectral density.

In contrast, a more complex situation arises for semiconductors that possess multiple equivalent valleys at the conduction band minima. In these materials, even under the warm electron constraint, the electric field alters not only the average energy of the carriers but also the distribution of carriers among the different valleys. Intervalley coupling, or scattering between different valleys, manifests as features not seen in GaAs such as nonparalellism of the current with electric field [160], anisotropic mobility [161] and spectral density [38], and hot carrier redistribution among valleys [162]. Computing these properties can be accomplished with the

same electron-phonon matrix elements used to calculate the mobility and noise properties.

To investigate the more complex case of multi-valley semiconductors, we perform calculations in silicon. Silicon is an elemental semiconductor with diamond cubic crystal structure. As can be see in Fig. 3.13, in contrast to GaAs, Si is an indirect gap material with six equivalent valleys along $\langle 100 \rangle$. These valleys are ellipsoidal and well-approximated with effective masses $m_{\parallel} = 0.98 m_0$ and $m_{\perp} = 0.19 m_0$. As electrons are driven out of equilibrium in Si, anisotropic redistribution in the valleys creates anisotropy in the macroscopic quantities such as the conductivity and the noise spectral densities. In this analysis, we extend the method to treat carriers in the hot electron regime. In our previous study, the electric field was restricted to values where $\Delta f_{m\mathbf{k}} \ll f^0_{m\mathbf{k}}$ to ensure the linearization above was valid. However, an important observation is that the linearization of the collision integral is valid as long as $f^0_{\mathbf{k}} \ll 1$, corrresponding to non-degenerate occupation of the electronic states. Under this less restrictive requirement, we are able to simulate the transport and fluctuations of "hot electrons" in Si where $\Delta f_{m\mathbf{k}} > f^0_{m\mathbf{k}}$.

3.6 Electronic transport and fluctuations in Si

In Si, when the electric field is aligned along a high symmetry direction such as the $\langle 111 \rangle$, the six valleys are oriented equivalently with respect to the electric field. Each valley thus has the same population, and contributes equally to transport properties. Even under non-equilibrium conditions, the valleys remain identical in their contribution to macroscopic observables. Figure 3.14 shows the population of a single representative valley when the field is oriented along $\langle 111 \rangle$. The population in the valley is exactly one-sixth of the total population and that fraction is invariant with respect to the field strength.

On the other hand, when the field is aligned along an arbitrary axis, the anisotropic bandstructure breaks the equivalency among the valleys when the electrons are heated by the field. For example, when a field is applied along $\langle 100 \rangle$ the valleys are no longer equivalently oriented, but are rather split into two groups. The first group is composed of the two valleys along $\langle 100 \rangle$ oriented longitudinally to the field. Under these conditions, valleys of this type have a higher population in states along the longitudinal axis, which presents a high effective mass ($m_{\parallel} = 0.98 m_0$). Consequently, electrons in these valleys are harder to accelerate with the field. Heating by the field is proportional to the electrical mobility, and so these valleys of

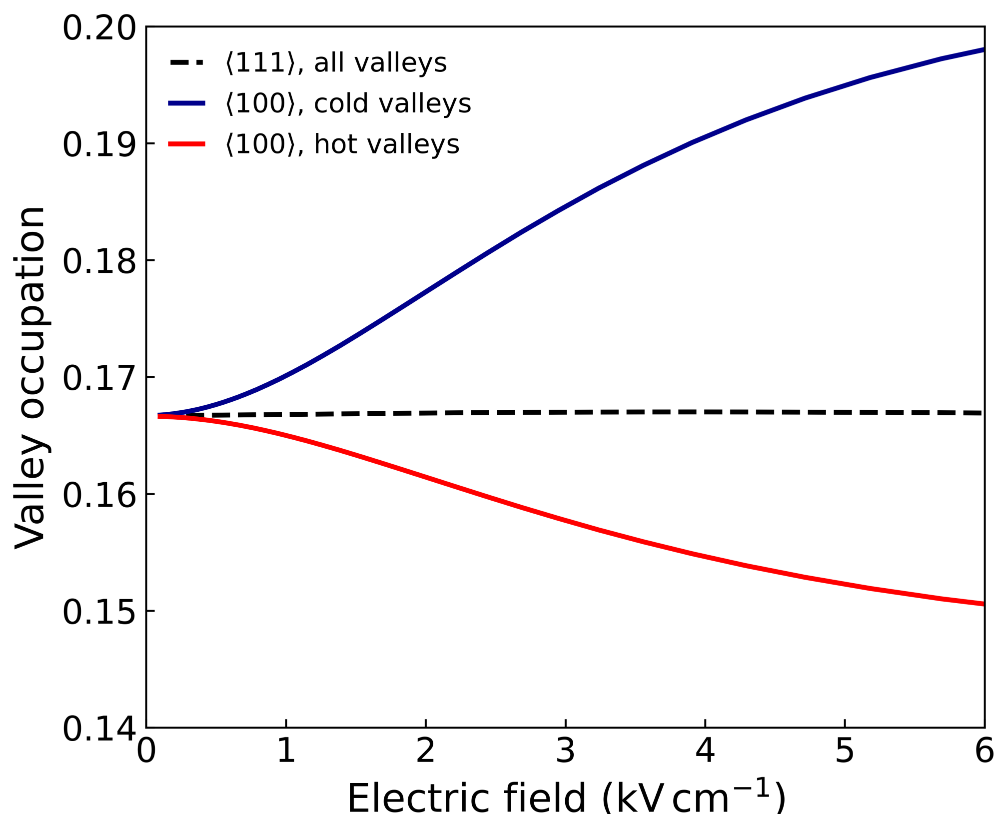

Figure 3.14: Population of individual valleys for Si versus electric field. When field is applied in the ⟨111⟩ direction, valleys are equivalent and population in each remains constant with field. In contrast, for the inequivalent ⟨100⟩ case, two cold valleys longitudinal to ⟨100⟩ form with increased population, and four hot valleys with decreased population from equilibrium.

this type are termed "cold" valleys. The second group is composed of the four valleys oriented transversely to the electric field, along ⟨010⟩ and ⟨001⟩. These valleys have their longitudinal axes perpendicular to the electric field, and thus present a smaller effective mass along this direction ($m_{\perp} = 0.2\, m_0$) and consequently are termed "hot." Figure 3.14 shows that for a field in ⟨100⟩, the valleys no longer remain equivalent under non-equilibrium conditions. Figure 3.15 shows the equivalent electron temperature of each valley type as a function of the electric field. When the field is oriented along the high symmetry ⟨111⟩ direction, each valley heats by an equivalent amount, proportional to the reciprocal of the effective mass along this axis. In contrast, when the field is oriented along ⟨100⟩, in the "hot" valleys, the heating is more efficient due to the lower effective mass than in the "cold" valleys.

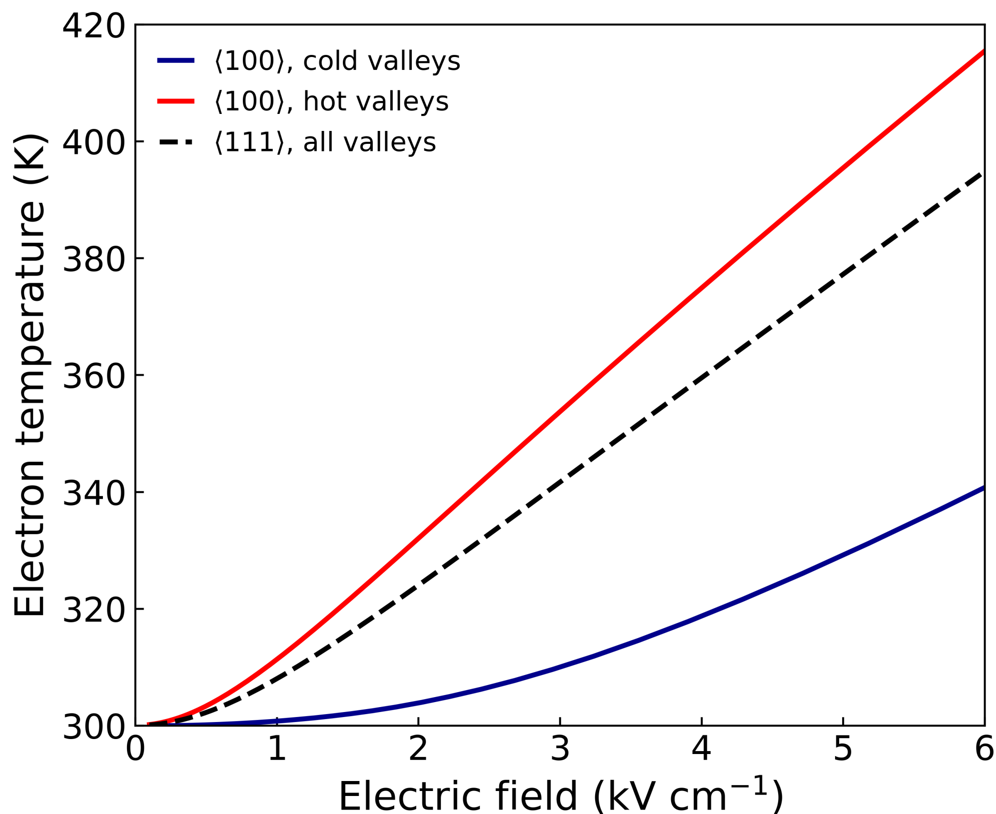

Figure 3.15: Equivalent electron temperature calculated for each valley type for electric field applied in the ⟨100⟩ (solid lines) and ⟨111⟩ (dashed black line). When the field is applied along the high symmetry direction, all valleys remain equivalent and heat at a rate proportional to the inverse of the mean effective mass. On the other hand, when the field is applied along ⟨100⟩ heating in the four transversely oriented valleys at ⟨010⟩ and ⟨001⟩ is more efficient due to the lower effective mass while the heating in the two heavy longitudinally oriented valleys is less efficient.

As the field increases, electrons evaporate from the 4 hot valleys and condense in the 2 cold valleys as seen in Fig. 3.14.

The transfer of carriers between inequivalent valleys has important effects on observables such as the drift velocity. Figure 3.16 shows the drift velocity-field curves for Si for electric field oriented along ⟨111⟩ and ⟨100⟩. When the field is along ⟨100⟩, the four hot valleys exhibit a higher mobility than in the equivalent valley case, while the two cold valleys exhibit a lower relative mobility. Intervalley scattering causes the population redistribution to the cold valleys seen in Fig. 3.14, and the overall effect is a lower drift velocity when the field is applied in the ⟨100⟩.

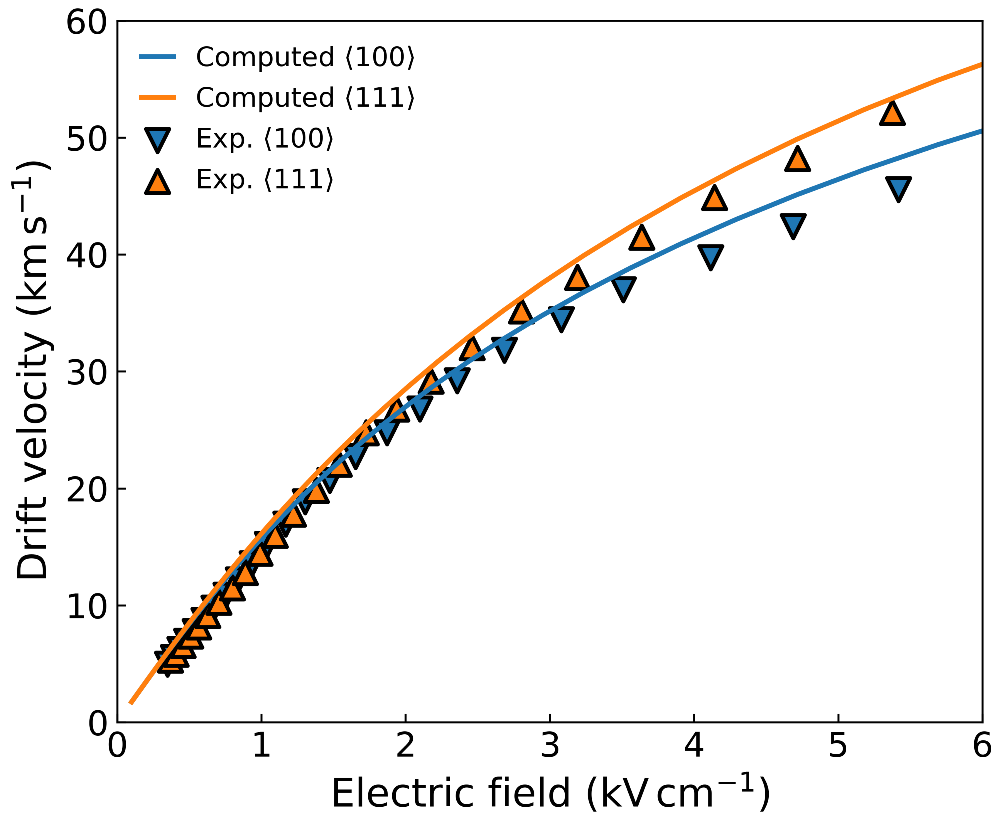

Figure 3.16: Drift velocity versus electric field for the cases of the field applied in both the ⟨111⟩ and ⟨100⟩ directions. Election redistribution into the cold valleys with lower mobility causes a lower drift velocity at high fields in the ⟨100⟩ case. The symbols correspond to experimental measurements (Figure 6(a), Ref. [161]).

Warm electron tensor in Si

The above results illustrate that our simulations qualitatively reproduce the experimentally measured variation of the mobility with field as well as the reported anisotropy in the mobility for warm electrons in Si [161]. A more quantitative analysis of the agreement can be obtained through direct calculations of the warm electron conductivity tensor of the material. At very weak electric fields such that $T_e = T_l$, the current is expressed through σ_0, the linear DC conductivity of Eqn. 2.13. At intermediate fields for which $T_e > T_l$, the current density vector $\mathbf{j} = j_1, j_2, j_3$ in a semiconductor may be expanded as a power series of the electric field as:

$$j_i = \mathcal{E}\sigma_0 e_i + E^3 \sigma_{iklm} e_k e_l e_m + \ldots \tag{3.10}$$

where e_i represent the cubic axes of the material and σ_{iklm} is the fourth-rank warm electron conductivity tensor. The warm electron regime is the constrains the electric field to the range for which the first two-terms of this expansion are a suitable approximation of the conductivity. For cubic crystals with class 23 symmetry, the 81 components of the warm electron tensor can be reduced to three independent constants $\sigma_{1111}, \sigma_{1122}, \sigma_{2211}$ through cyclic permutation and arbitrary permutation of the last three subscripts. For elemental Si, which is characterized by the $m3m$ point group, the fourfold axis guarantees the equivalency of each coordinate axis and consequently, the arbitrary permutation extends to all four subscripts such that $\sigma_{1122} = \sigma_{2211}$ [163].

For the definitions $\sigma_{1111} = \sigma_0\beta$ and $\sigma_{1122} = \sigma_0(\beta-\gamma)/3$, Eqn. 3.10 can be expressed in matrix notation as:

$$\mathbf{j} = \sigma_0\{[1 + (\beta - \gamma)\mathcal{E}^2]\Delta + \gamma\mathcal{E}^2\Gamma_1\} \cdot \mathbf{E} \tag{3.11}$$

where β and γ are fitting parameters, Δ is the unit tensor, and Γ_1 is:

$$\begin{pmatrix} e_1^2 & 0 & 0 \\ 0 & e_2^2 & 0 \\ 0 & 0 & e_3^2 \end{pmatrix}.$$

From these results, the longitudinal current in the field direction can be expressed as:

$$j_l = \mathbf{j} \cdot \mathbf{e} = \sigma_0\mathcal{E}\left[1 + \beta\left(\sum_i e_i^4 - 1\right)\mathcal{E}^2\right] \tag{3.12}$$

and the transverse component j_t can be expressed as:

$$\frac{j_t}{j_l} = \gamma\sqrt{\sum_i e_i^6 - \left(\sum_j e_j^4\right)^2}. \tag{3.13}$$

These results indicate that owing to symmetry considerations, charge transport for warm electrons in Si is fully defined by the coefficients β and γ that describe the rate change of the conductivity with heating and the non-parallelism of the field, respectively. These quantities are macroscopic indicators of the energy coupling of

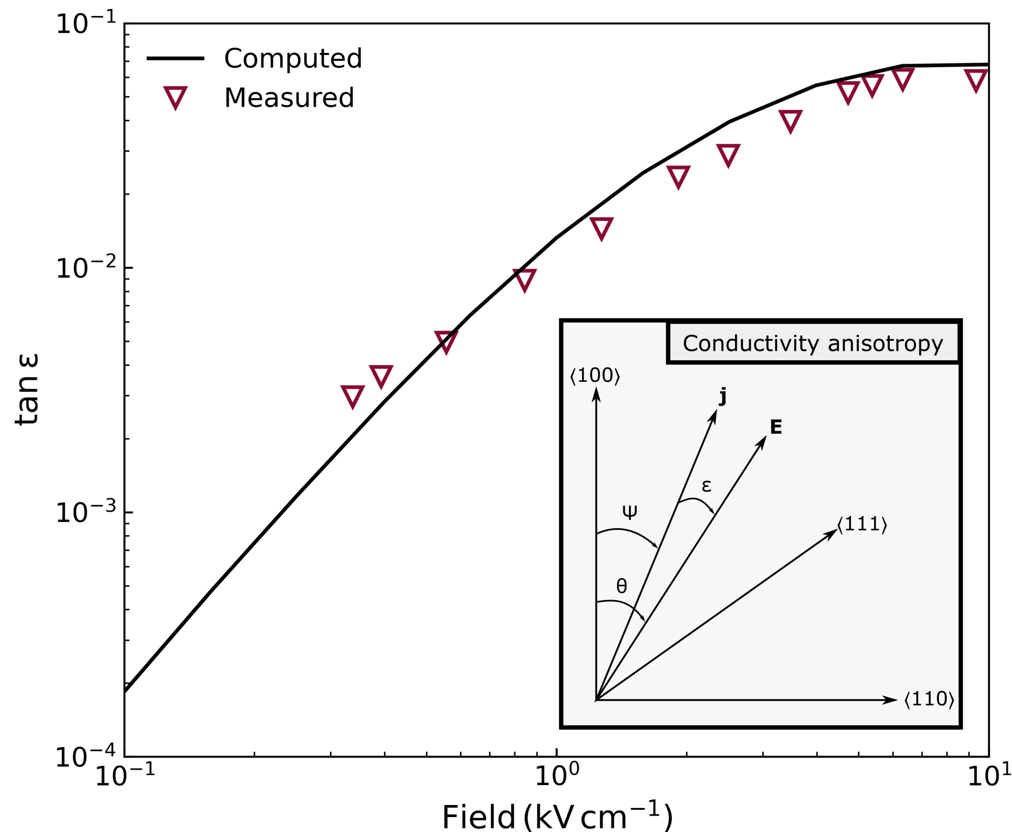

Figure 3.17: Computed (black solid line) current non-parallelism ratio $\tan\epsilon$ versus electric field strength at $\theta = 23°$. The simulated non-parallelism is in excellent agreement with reported measurements of Ref. [164] in n-Si (red triangles), indicating accurate calculation of anisotropy in the bandstructure. **Inset**: A common experimental technique to quantify the anisotropy of the conductivity is to sweep the orientation of the electric field θ with respect to $\langle 100\rangle$ in the (110) plane and to measure the non-parallelism angle ϵ.

carriers to the lattice and the anisotropy of the electronic bandstructure. Computing β and γ allows for a more quantitative comparison of our *ab initio* simulations to experiments that examination of the drift-field curves alone.

Equation 3.13 indicates that the coefficient γ is a measure of the non-parallelism of the electric field and the current in cubic semiconductors. A common experimental technique to quantify this non-parallelism, also known as the Shibuya-Sasaki effect [165], is to apply an electric field in the (110) plane and sweep the orientation θ of the field from $\langle 100\rangle$ to $\langle 111\rangle$. Under such conditions, the current non-parallelism is quantified by the angle ϵ as seen in the inset of Fig. 3.17. In practice, it is

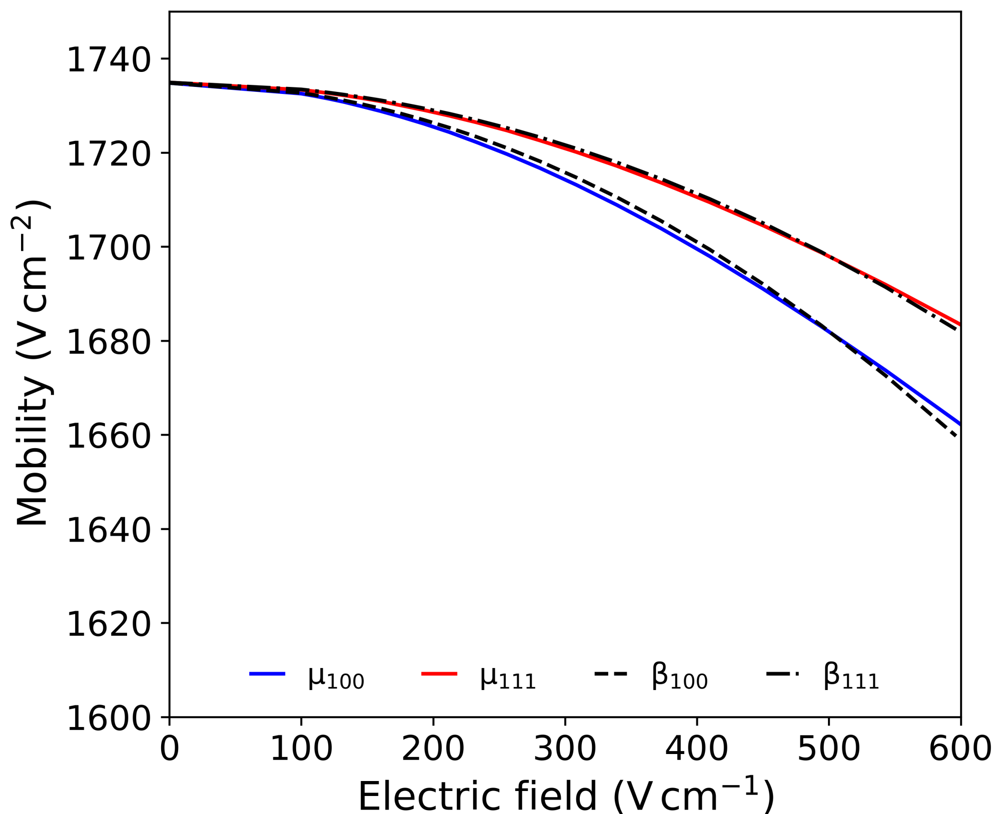

Figure 3.18: Simulated longitudinal mobility as a function of electric field strength along the ⟨100⟩ (solid blue line) and ⟨111⟩ (solid red line) axes along with the fitted warm-electron model of Eqn. 3.11 for β. The β component of the warm electron tensor describes the rate at which the mobility changes with the applied field, and is a macroscopic descriptor of the energy exchange between charge carriers and the lattice.

common to report measurements of $\tan \epsilon = j_t / j_l$, which by Eqn. 3.13 is equivalent to γ. Figure 3.17 shows the computed current non-paralellism $\tan\epsilon$ at a fixed field orientation versus electric field strength. The simulated non-parallelism exhibits excellent agreement with measurements in n-Si [164], indicating that our calculations have correctly captured the anisotropy of the bandstructure over a broad range of energies.

Simulations of the longitudinal mobility can be used to extract β for different orientations of the electric field in the (110) plane. Figure. 3.18 shows computations of the longitudinal mobility along the ⟨111⟩ and ⟨100⟩ axes. Fitting the data in the warm electron regime, we can extract β by fitting the simulated mobility to the

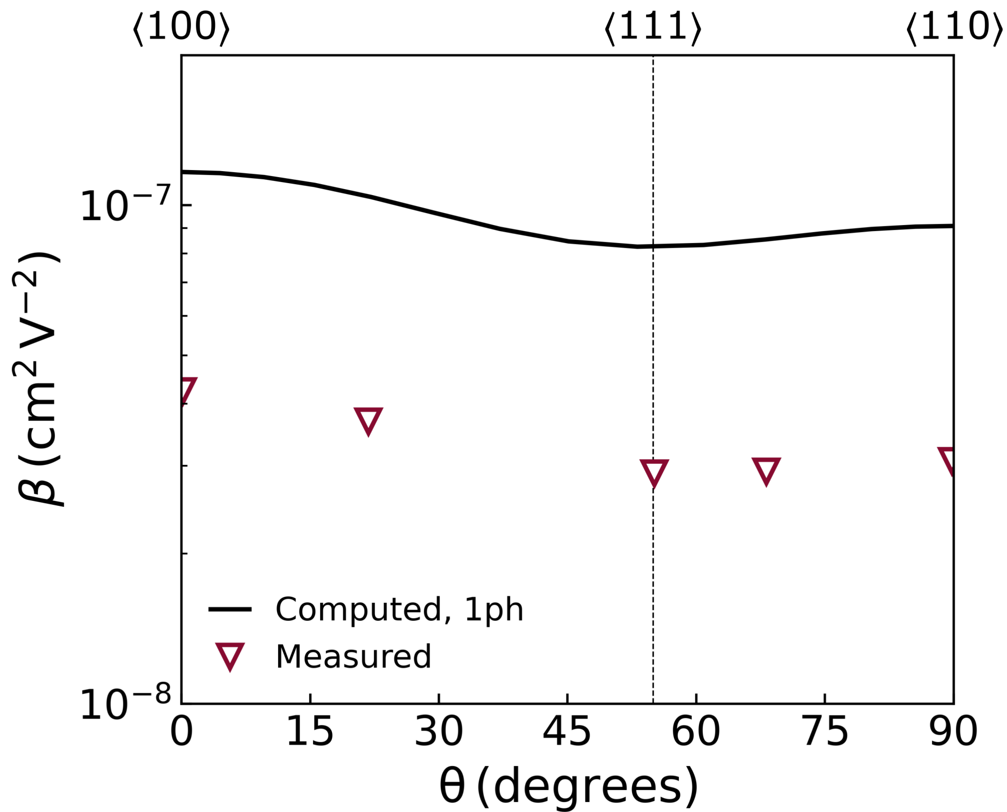

Figure 3.19: Simulated anisotropy of β (black solid line) as a function of the field orientation in the (110) plane θ. Although the widely accepted 1-phonon scattering theory in n-Si is capable of reasonable qualitative fitting of the velocity-field curve shown in Fig. 3.16, the simulated β at all orientations is about twice as large as that reported in measurements [166] (red triangles), suggesting that the present theory is not accurately describing energy relaxation in Si.

parabola described by Eqn. 3.11. Figure 3.19 shows the extracted β for simulations sweeping the electric field from the $\langle 100 \rangle$ to $\langle 110 \rangle$ axis with angle θ. While the simulated dependence of β on the orientation of the field captures the trend exhibited in measurements [166], with an initial decrease to a minima from $\theta = 0 - 55°$ followed by an increase from $55 - 90°$, the computed values exceed measurements by roughly a factor of two. This result, combined with Fig. 3.17 indicates that while our simulations have correctly reproduced the anisotropy and non-parallelism of the electrical conductivity in Si, our simulations fail to reproduce the energy coupling of electrons to the lattice parameterized by β.

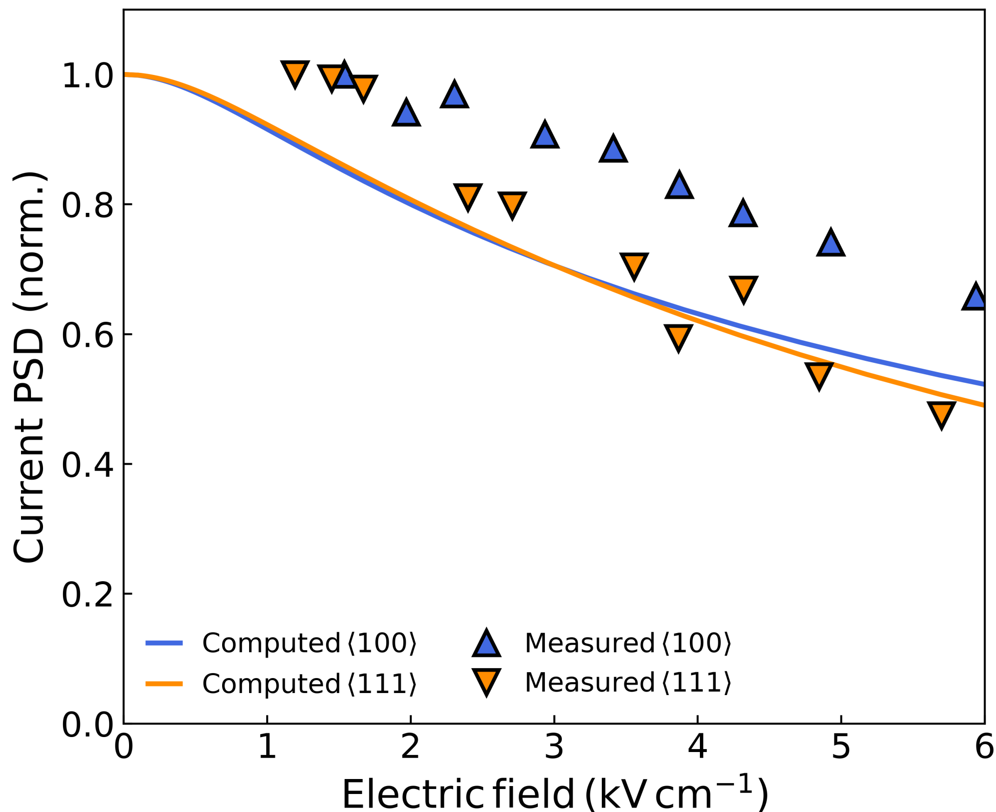

Figure 3.20: Simulated longitudinal current density fluctuations in Si at 300 K along the ⟨100⟩ (solid blue line) and ⟨100⟩ (solid orange line) axes, normalized to the Nyquist value as a function of electric field. The symbols correspond to experimental measurements (Figure 4, Ref. [167]).

Refinement of scattering theory in Si

The discrepancy between measurements and our simulations of the warm electron tensor in Si illustrates the utility of the newly developed method. Si is an extremely well-studied material in the *ab initio* community [31, 90, 95, 143, 168]. In recent years, using the low-field phonon-limited mobility as a simulated observable, first-principles studies in Si have generated increasingly refined models of charge transport and scattering in Si. Recent works have identified the contributions of various many-body quasiparticle corrections such as the long-range quadrupole interaction [143, 168], spin-orbit coupling [90, 95], and of different approximations to the exchange and correlation potential [90]. Despite this progress, owing to the focus on the low-field mobility, there have been few efforts to investigate energy relaxation between heated electrons and the lattice.

Extending first-principles calculations to observables such as the warm electron tensor therefore represents a more rigorous test of the accepted physical models of scattering and bandstructure in Si. Calculations of the power spectral density in Si confirm the qualitative picture outlined by Fig. 3.19. Figure. 3.20 shows computations of the longitudinal current spectral density in Si at 300 K as a function of the electric field along the high symmetry axes $\langle 100 \rangle$ and $\langle 111 \rangle$. Our calculations reproduce some qualitative features exhibited in measurements [167]. The computations capture the monotonic decrease in the PSD up to 600 $\mathrm{kV\,cm^{-1}}$. Further, the computations show that at sufficiently large fields, the spectral density along the $\langle 100 \rangle$ begins to exceed that along the $\langle 111 \rangle$ as inequivalency between hot and cold valleys induces intervalley velocity fluctuations [38]. The electric field at which the inequivalency between $\langle 100 \rangle$ and $\langle 111 \rangle$ becomes apparent is an indication of the energy balance between electrons and the lattice, as the split-off only occurs when the electrons are heated enough to redistribute asymmetrically into hot and cold valleys as seen in Fig. 3.14. In the computations, the critical field is around 4 $\mathrm{kV\,cm^{-1}}$, which is substantially higher than the 2 $\mathrm{kV\,cm^{-1}}$ observed in experiments. In confirmation of the qualitative picture outlined by Fig. 3.19, these results indicate that the implemented theory is an insufficient description of the electron-phonon interaction in warm Si.

A plausible explanation for the discrepancies of Figs. 3.19 and 3.20 is that multiphonon scattering mechanisms such as the 2ph processes described in Sec. 2.3 are needed to properly capture energy relaxation in Si. Recent *ab initio* studies have highlighted the importance of 2ph processes in polar materials such as GaAs [93], however in non-polar materials such as Si, the accepted level of theory for first-principles transport calculations is the leading-order, 1ph expansion of the electron-phonon interaction. [41, 90, 95, 139]. While the contribution of multiphonon processes to phenomena such as the infrared optical absorption [169, 170], the second-order Raman spectrum [171, 172], or magnetophonon resonance [173] in non-polar semiconductors has been well-characterized experimentally, the impact of 2ph processes on the warm electron tensor remains less explored.

Promisingly, some early theoretical studies have identified scattering involving two short-wavelength acoustic modes as a significant energy dissipation mechanism in Si, comparable to that of 1ph acoustic scattering [174, 175]. Conducted prior to the development of first-principles methods, these computations relied upon simplified models of Si, utilizing parabolic bandstructure, deformation potential approxima-

tions to the scattering, and heated Maxwellian distribution functions. Furthermore, the magnitude of the contribution of 2ph scattering to energy dissipation in Si remains a subject of open debate [176, 177]. Consequently, further *ab initio* studies in Si are necessary to expound the contribution of 2ph processes to energy relaxation and accurately reproduce the measured electronic noise. These studies are the subject of our ongoing work.

3.7 Summary of simulations

In the previous two chapters, we have described an *ab initio* theory of electronic noise for hot electrons in semiconductors. In contrast to the typical Monte Carlo approaches to hot electron noise [129–131, 178], the method requires no adjustable parameters, with the phonon dispersion, band structure, and electron-phonon coupling calculated from first-principles. Further, this method permits the study of transport even when the electrons are not in equilibrium with the lattice, being free of the cold electron approximation used in previous transport studies. To demonstrate the method, we first performed calculations in GaAs, a technologically relevant material, and demonstrated that the spectral features of the AC mobility and current noise are linked to the disparate time scales of energy and momentum relaxation. The quasi-elastic approximation is unexpectedly accurate in GaAs despite the dominance of highly inelastic polar optical phonon scattering. In our second application, we investigated transport and fluctuations of hot electrons in Si. Our computations reveal that the accepted level of 1ph scattering theory is unable to reproduce measurements of the warm electron tensor and the current power spectral density in Si. These results suggest that a higher level of scattering theory, possibly incorporating 2ph processes, is necessary to accurately capture energy dissipation in this material. Our work paves the way for first-principles studies of electronic noise in other semiconductors that will advance the study of transport phenomena and applications of low-noise semiconductor devices.

Chapter 4

CHARACTERIZATION OF SELF-HEATING IN CRYOGENIC HIGH ELECTRON MOBILITY TRANSISTORS USING SCHOTTKY THERMOMETRY

This chapter has been adapted, in part, from:

1. **Choi, Alexander Y.**, Esho, I., Gabritchidze, B., Kooi, J. & Minnich, A. J. Characterization of self-heating in cryogenic high electron mobility transistors using Schottky thermometry. *Journal of Applied Physics* **130.** https://doi.org/10.1063/5.0063331 (15 Oct. 2021).

   Contributions A.Y.C. built the experimental setup, performed all Schottky thermometry measurements, wrote the data analysis code, performed the data analysis, made the paper figures, and wrote the manuscript.

A theoretical approach to fluctuations can provide deep insights into the physics of noise in commonly used materials. One objective of our work, as illustrated in Chapters 2 and 3, has been to use theory and simulations to understand the microscopic mechanisms underpinning noise in semiconductor materials. A second objective of this thesis is to contribute to the understanding of electronic noise in the context of practical applications. To this end, targeted experiments on electronic noise in cryogenic low-noise detectors can provide valuable information on the mechanisms that set the performance limits of the best scientific instrumentation.

The overarching goal of this chapter is to develop an experimental technique to assess the thermal contribution to the microwave noise figure of a HEMT amplifier operated at both room and cryogenic temperatures. We begin the chapter by discussing the background of the field, culminating in the open question that motivates our study. Next, we discuss conventional thermometry methods and the specific requirements of our system that make such methods impractical. To address these requirements, we describe the Schottky thermometry technique and how it enables the extraction of gate temperature through simple DC and high-frequency S-Par measurements. Following this, we provide information about our samples as well as the relevant specifications necessary for the implementation of the technique. To conclude this chapter, we will discuss the extracted temperature and thermal resistance and the

implications of the measurement for amplifiers operating at the cryogenic low noise operating point.

4.1 Background

In this work, we focus on improving the understanding of noise in high electron mobility transistors (HEMTs). HEMTs are distinguished from the more commonly-used MOSFETs in the method used to produce the conducting channel. The difference can be best understood by examining the energy band diagrams as seen in Fig. 4.1. In an n-channel MOSFET, the metal gate stack sits atop a doped p-type semiconductor channel, with a thin oxide interface separating the materials. As positive bias is applied to the gate, a depletion layer forms at the interface as holes are forced away from the interface. At even higher voltages, above the threshold voltage, the depletion layer reaches a maximum thickness and a thin inversion layer of electrons forms at the interface. When the channel is biased, electrons in the inversion layer provide a conducting channel through the device.

In contrast to the MOSFET, which use a planar MOS to create an inversion layer in a doped semiconductor, the HEMT channel is formed by combining materials with dissimilar bandgaps into a heterojunction. Specifically, the HEMT channel is formed from a doped wideband semiconductor and an intrinsic narrow band semiconductor. As seen in Fig. 4.1, band-bending in the dissimilar materials creates a quantum well at the interface, and at sufficiently high biases, free electrons in the doped semiconductor fall into the well of the intrinsic semiconductor, and are confined as a two-dimensional electron gas (2DEG). In contrast to the MOSFET, the charge carriers in the HEMT are spatially separated from the impurities. Due to the associated reduction in impurity scattering, HEMTs possess significantly improved mobility over MOSFETs, allowing for higher gain and faster switching [38].

These qualities make HEMTs particuarly suitable for precision instrumentation. Microwave low noise amplifiers (LNAs) based on HEMTs are widely-used components of scientific instrumentation in fields such as radio astronomy [47, 48], deep space communication [179], and quantum computing [49–53]. After decades of development [55, 60, 67–69], HEMT LNAs have achieved cryogenic noise temperatures approximately 5-10 times the quantum limit over frequencies from 1-100 GHz [47]. Despite this progress, applications drive the development of amplifiers with ever-lower noise figures.

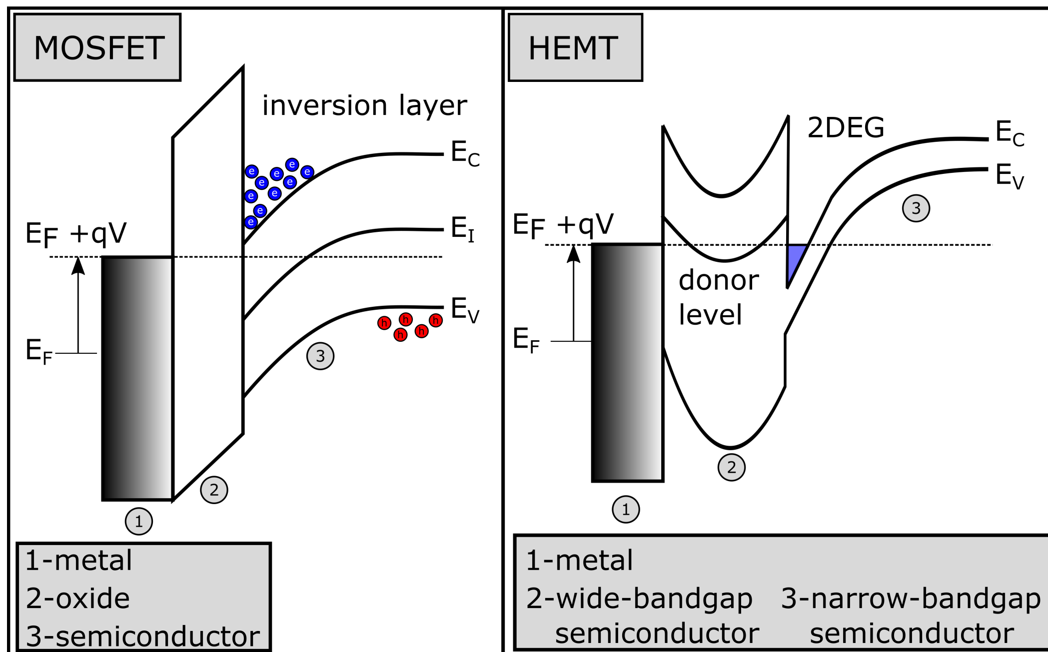

Figure 4.1: Representative energy band diagrams of n-channel metal oxide semiconductor field effect transistor (MOSFET) and high electron mobility tranistor (HEMT). In a n-MOSFET, when sufficiently high bias applied to the metal gate, holes are forced away from the interface and a thin inversion layer of electrons serves as the conducting channel of the device. In contrast, in HEMTs, the conducting channel is formed from the 2DEG produced at the heterojucntion of two semiconductors, one wide and the other narrow bandgap.

Noise in HEMT amplifiers is typically interpreted using lumped-element circuit models such as the Pospieszalski model [46]. As seen in Fig. 4.2, in this model noise is decomposed into components associated with the drain conductance and the gate resistance, parameterized by by equivalent noise temperatures T_d and T_g, respectively. These components have been ascribed to hot-electron noise in the channel and thermal noise in the gate. The gate noise temperature T_g is typically assumed to be the cryostat base temperature, $T_g = T$, while the drain temperature is fit to measured noise data. For a constant drain current, the hot electron contribution is taken to be constant and the minimum noise figure then scales as $T_g^{1/2}$ [48]. Owing to this scaling, low noise amplifiers are typically operated at cryogenic temperatures in weak-sensing applications.

Although the noise temperature does decrease with base temperature over a range of temperatures as predicted, at liquid helium temperatures the noise temperature is observed to plateau to a value several times the quantum noise limit [72–75].

This noise temperature plateau has been attributed to a variety of mechanisms, including drain shot noise [76], gate leakage current [55], and self-heating [72, 77]. In particular, Ref. [72] used measurements of microwave noise to conclude that the thermal resistance associated with phonon radiation leads to non-negligible self-heating at cryogenic temperatures. However, this conclusion is based on an indirect estimate of the gate junction temperature using a noise model.

Measurements of the gate temperature at the low-noise bias and cryogenic temperatures would provide more direct evidence that self-heating is the origin of the noise temperature plateau. This measurement is challenging for conventional thermometery techniques such as IR microscopy [78, 79], micro-Raman spectroscopy [80–82], or liquid crystal thermography [83]. In particular, micro-Raman is challenging owing to the sub-micron dimensions associated with the HEMT structure. Modern HEMTs typically possess gates with length on the order of 100 nm while the spot-size for Raman is typically on the order of 500 nm. IR microscopy is similarly limited by geometrical constraints; the HEMT gate junction is typically buried under passivating oxide layers to form a dielectric barrier to the rest of the device, preventing direct imaging of local hotspots. Finally, nematic liquid crystal thermometers can only provide an averaged temperature over the film and cannot be used to measure buried layers. Other methods such as resistance thermometry of the gate require the fabrication of custom structures or the use of alternate metals [180] which can be difficult to incorporate into the HEMT process [181].

Owing to these dificulties, self-heating in FETs is usually characterized with measurements of other temperature-sensitive electrical parameters. Early semi-quantitative studies of self-heating in CMOS estimated the temperature under bias using the temperature-dependence of drain current [182–184]. However, these approaches neglected a number of mechanisms relevant to the drain current in sub-micron devices such as the bias dependence of threshold voltage, series resistances, and non-stationary transport effects, which are known to be important in modern HEMTs and could affect the extracted temperature rise. Later studies of self-heating in MOSFETs incorporated some of these effects and reported measurements of temperature rise and thermal time constants [185]. Recent work in SOI MOSFETs reported that the dominant thermal resistance is due to the buried oxide layer [186].

Self-heating studies in HEMTs have largely focused on GaN power FETs operated at room temperature, where device lifetime is limited by channel heating [187]. In one approach, the temperature rise is extracted from pulsed measurements on the gate

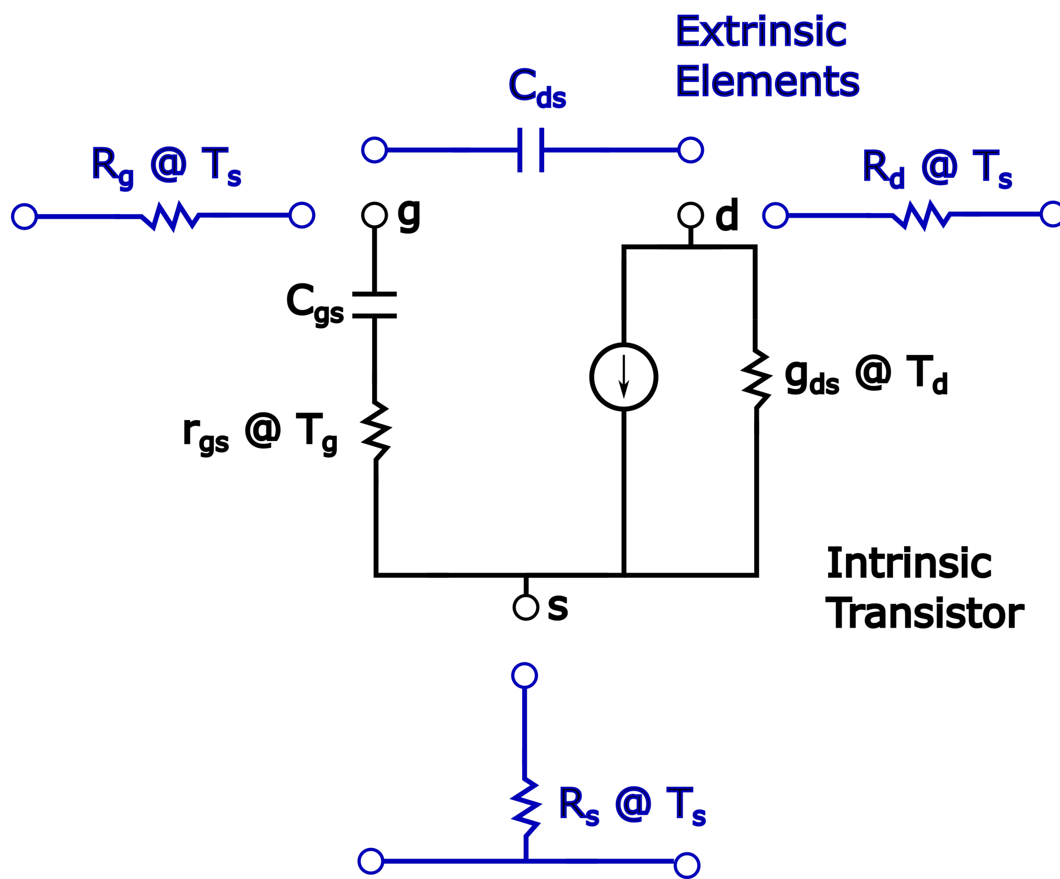

Figure 4.2: Pospieszalski FET noise model. The extrinsic parasitic elements (blue) such as the gate, source, and drain pad resistances as well as the various capacitances are typically removed via a de-embedding procedure. Noise in the intrinsic device (black) is disaggregated into a thermal source added at the gate input and a hot electron source added at the channel output.

[188, 189], but this technique is generally unsuitable for low noise cryogenic HEMTs, where the thermal time constants are on the same order as the pulse duration [190]. Bautista and Long used calibrated measurements of gate leakage current for various drain biases to conclude that the gate temperature in cryogenic InP HEMTs was close to that of the base temperature. [75] However, the magnitude of the thermal resistance was not reported, and the physical origin of the thermal resistance and the impact of self-heating on the noise performance at liquid helium temperatures were not discussed. As a result, self-heating in cryogenic III-V HEMTs and its impact on noise remains a topic of interest.

In this work, we report measurements of the junction temperature and thermal resistance of the gate in a low-noise metamorphic HEMT using a Schottky thermometry

method based on the temperature-dependent forward diode characteristics of the gate. At cryogenic temperatures, we observe a nonlinear trend of the thermal resistance on dissipated power that is consistent with heat transport by phonon radiation. Although the measurements are not performed at the low-noise bias, this finding can be used to estimate the magnitude of self-heating at this bias. Using a radiation circuit model, we find that at the low-noise bias the gate self-heats to a value comparable to the physical temperature of the channel, contradicting the typical assumption that the gate is isothermal with the base temperature. Our study thus implies that without improvements to device thermal management to remove heat from the gate, self-heating results in a practical lower limit for HEMT microwave noise figure at cryogenic temperatures.

4.2 Schottky Thermometry technique

We measure temperature of the HEMT gate-barrier junction by utilizing the gate's diode characteristics. Under thermionic emission theory, the current in a Schottky diode under forward bias is given by:

$$I = I_S \exp\left(\frac{q\,(V - IR_S)}{\eta\, k_B T_j}\right) \tag{4.1}$$

where q is the elementary charge, k_B is the Boltzmann constant, R_S is the parasitic series resistance, I_S is the saturation current, η is the ideality factor, and T_j is the intrinsic junction temperature. In many previous diode characterization studies [191–193], $I - V$ characteristics at different base temperatures T are fit to Eqn. 4.1 and the diode parameters R_S, I_S, and η are extracted under two assumptions. The first assumption is that the junction is at the base temperature $T_j = T$, or that the junction is isothermal with the rest of the device. The second assumption is that the Schottky parameters are independent of temperature and consequently have no bias dependence. These assumptions are only accurate when the power dissipated as Joule heating is insufficient to cause substantial temperature rise during measurement. In reality, as higher frequency performance drives miniaturization of the HEMT gate, devices are subject to increasingly high power densities $\sim$ mW µm^{-2}. With modern gate areas on the order of a square micron, these biases can induce large temperature rises due to self-heating. Consequently in devices where self-heating occurs, the conventional technique can lead large errors in the characterization of the Schottky parameters, as each point on a typical $I - V$ curve is at a different temperature. To address this limitation, in this work, we employ a

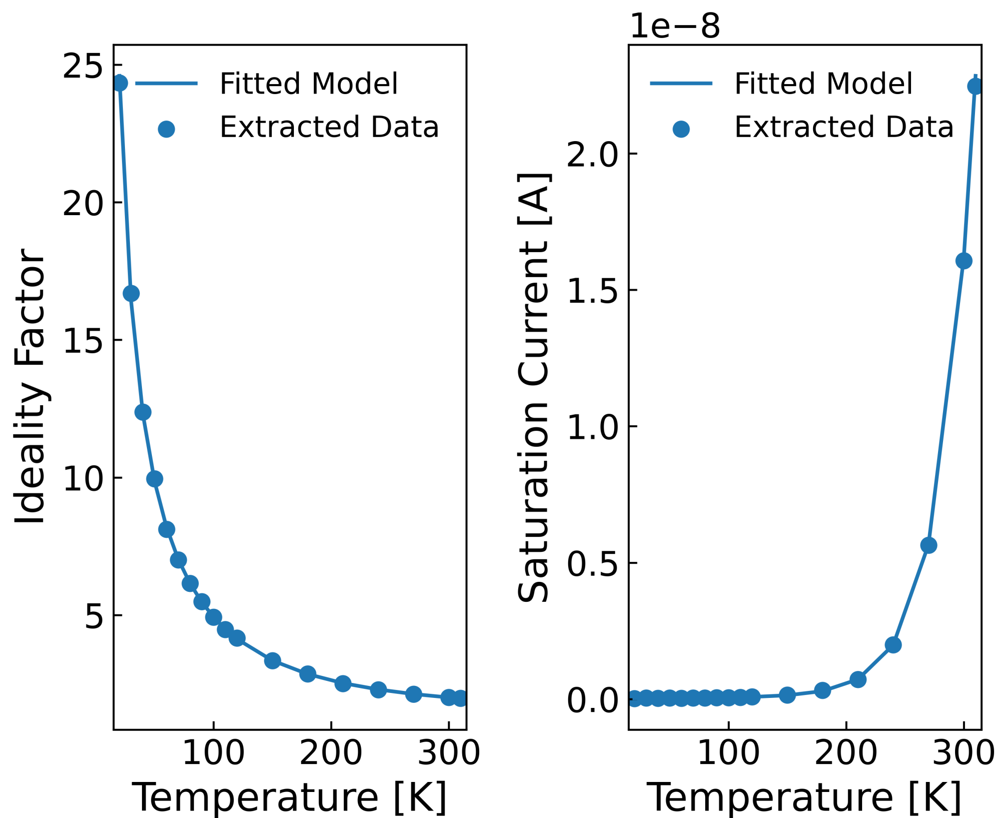

Figure 4.3: Extracted base temperature dependence (solid lines) for (a) the ideality factor and (b) the saturation current of a typical HEMT gate Schottky diode from cryogenic to room temperature. The fitted model shows excellent agreement with the measured ideality factor and saturation current (markers) across the entire temperature range. The uncertainty of the extracted quantities is sufficiently small that error bars are not visible.

technique [194] that combines direct current $I - V$ measurements at different base temperatures with high-frequency scattering parameter measurements. This method is free from the limiting assumptions of the conventional method and allows us to extract the thermal resistance and temperature of the gate-barrier Schottky diode.

Two mechanisms contribute to charge transport across the Schottky barrier. The first mechanism is thermionic emission (TE), in which carriers are thermally excited over the Schottky barrier. Naturally, the magnitude of the thermionic emission is temperature-dependant and in typical metal/n-GaAs junctions, TE tends to dominate current at temperatures above 100 K [195]. The second mechanism is associated with the quantum mechanical tunneling of electrons directly from the conduction

band of the semiconductor into the metal. This mechanism is independent of the temperature, and tends to dominate the forward diode characteriscs at low temperatures below 100 K [196, 197]. Considering both thermionic emission and tunneling, the temperate-dependence of the saturation current is expressed as [197]:

$$I_s(T_j) = S_a A^{**} T_j^2 \exp\left(\frac{-q\Psi_b}{\eta k_B T_j}\right) + I_0 \tag{4.2}$$

where S_a is the diode surface area, A^{**} is the classical Richardson constant, Ψ_b is the barrier height, and I_0 is the temperature-independent tunneling current.

The ideality factor is expressed:

$$\eta(T_j) = \frac{q}{k_B T_j} E_{00} \coth\left(\frac{qE_{00}}{k_B T_j}\right). \tag{4.3}$$

To obtain T_j for a given bias, the temperature dependence of I_S and η is extracted from DC I-V characteristics by varying the cryostat base temperature at low bias where self-heating is negligible and fitting to Eqn. 4.2 and 4.3. The extracted temperature dependence for a typical measurement is shown in Fig. 4.3.

Next, the small-signal resistance about a DC bias is determined from the microwave S parameters as:

$$r_T = \Re(Z_{11}) = R_S + r_j = R_S + \frac{\eta(T_j) k_B T_j}{qI} \tag{4.4}$$

where Z_{11} is the complex input impedance of the gate and r_j is the temperature-dependent dynamic resistance. Equating expressions for the series resistance in Eqns. 4.4 and 4.1 yields an equation including the measured Schottky and S Parameters in which the only unknown is the junction temperature:

$$\frac{V}{I} - \frac{\eta(T_j)\, k_B T_j}{qI} \ln\left(\frac{I}{I_S(T_j)}\right) = r_T - \frac{\eta(T_j)\, k_B T_j}{qI}. \tag{4.5}$$

With the DC I-V characteristics and S parameters for different biases known, we obtain the junction temperature at various base temperatures by numerically solving Eqn. 4.5. Although this method was originally developed for THz Schottky diodes at room temperature, the physical basis for the measurement is general and it can be applied to the gate Schottky diodes of HEMTs at cryogenic temperatures so long as the $I - V$ characteristics exhibit a dependence on temperature.

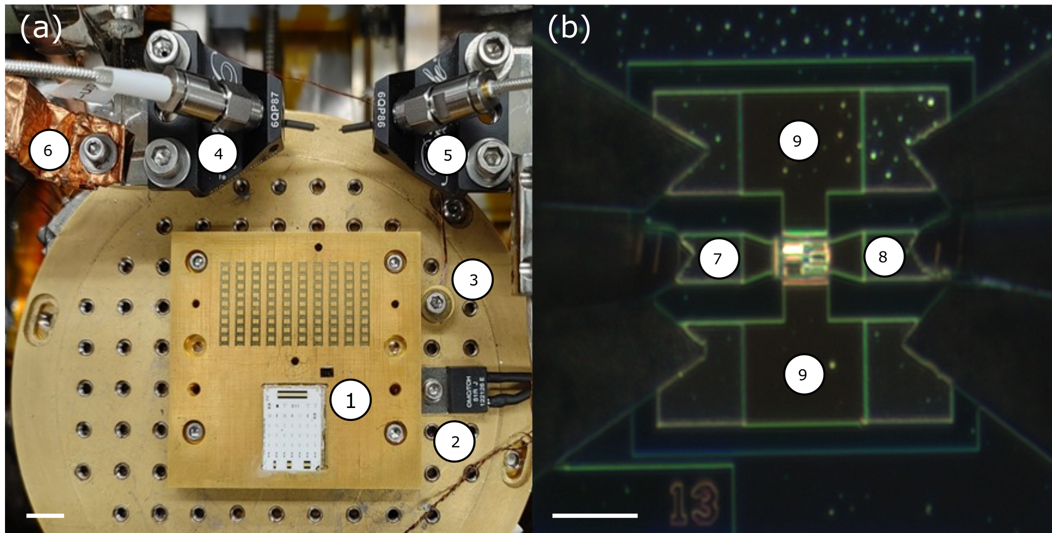

Figure 4.4: Microscope images of probe station instrumentation. (a) Stage of the cryogenic probe station used for DC and S Par measurements of the cryogenic HEMTs. (1) Brass mounting chuck (2) Lakeshore heater resistor (3) Lakeshore temperature sensor (4) CPW to coaxial gate probe (5) CPW to coaxial drain probe (6) coaxial thermal strap. (b) Magnified view of HEMT chip during probing. (7) gate pad (8) drain pad (9) common source pads. Scalebars correspond to 10 mm (left) and 100 μm (right).

4.3 Sample and method specification

We used this method to characterize the gate thermal resistance of an OMMIC metamorphic HEMT with 70 nm gate length and 200 μm gate width consisting of an InGaAs-InAlAs-InGaAsInAlAs epitaxial stack on a semi-insulating GaAs substrate over base temperatures from 20–300 K. Further details of the device are specified in Ch. 5.1 of Ref. [198]. All measurements were performed in a custom cryogenic probe station depicted in in Fig. 4.4 with cryostat base temperature (denoted base temperature, T) controlled between 20 K and 300 K by a LakeShore 336 temperature controller. The coplanar-waveguide (CPW) style probes are controlled with independent precision translation stages to enable the user to position the probes at specified x,y,z coordinates over the chuck, where the sample is mounted. The apparatus is cooled using a Sumitomo RDK-415D Gifford McMahon cryocooler and is capable of reaching 20 K from room-temperature within 8 hours. The WR-10 style probes are manually adjusted by an operator monitoring the system through an optical microscope positioned above vacuum windows in the radiation shield and cryostat lid. A schematic of the transmission lines in the cryostat is depicted in Fig. 4.5. Additional details of the measurement platform are available [199]. The

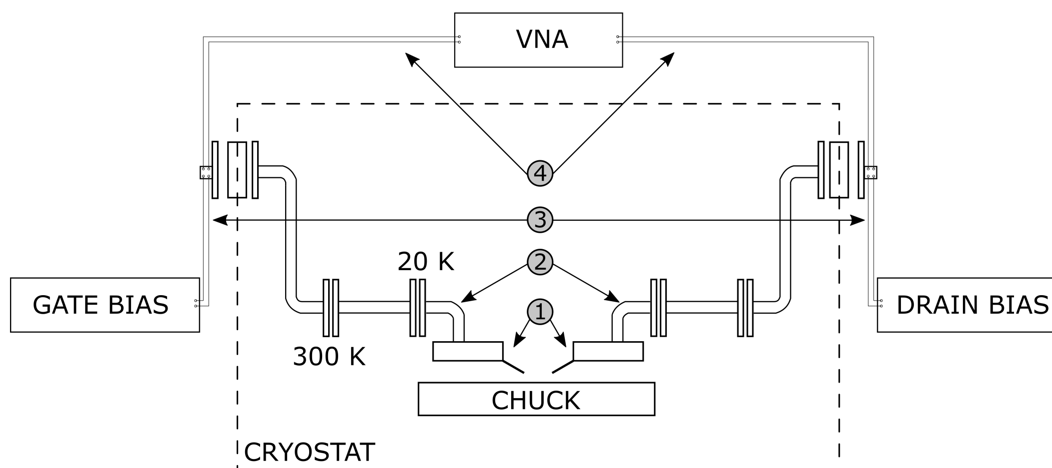

Figure 4.5: Schematic of cryogenic probe station setup for Schottky thermometry measurements. (1) WR-10 style coplanar-waveguide probes (2) internal SMA coaxial transmission lines (3) direct current transmission lines (4) external SMA coaxial transmission lines. Figure adapted from Ref. [199].

HEMT was biased using a Minicircuits ZX85-12G-S+ bias-tee. S-parameter measurements were performed with a Rohde & Schwarz ZVA50 vector network analyzer from 10 MHz to 18 GHz, calibrated with the through-reflect-match method.

The DC measurements were corrected for the parasitic resistance of the bias-tee and coaxial lines. In particular, the resistance through the transmission lines is measured by landing the CPW probes on a calibrated through pad. The temperature-dependence of the Schottky parameters I_s and η were extracted in the log-linear region at low bias $I \sim 100\ \mu A$ so that self-heating can be neglected but at sufficiently high bias so that the characteristic is still log-linear [200]. The saturation current and ideality factor were fit to Eqns. 4.3 and 4.2. The saturation current expression was modified by adding a temperature-independent term to Eqn. 3 in Ref. [194] to account for the tunneling gate leakage current that is known to dominate in low temperature Schottky diodes [197]. The numerical solution for Eqn. 4.5 is performed using Broyden's first Jacobian algorithm [201] from the SciPy optimization library.

After extracting the junction temperature, we verified that the self-heating can be neglected in the fit range by confirming that the temperature rise induced by the dissipation in the fit range at the highest extracted thermal resistance satisfies $T_j - T \ll T$. For example, the power density of the diode at 20 K and at 75 μA is $\approx$ 3 μW μm^{-2}. The highest thermal resistance extracted at 20 K is 800 μW μm^{-2}. The corresponding temperature rise is only 2 K, which satisfies $\Delta T/T_0 \ll 1$. The

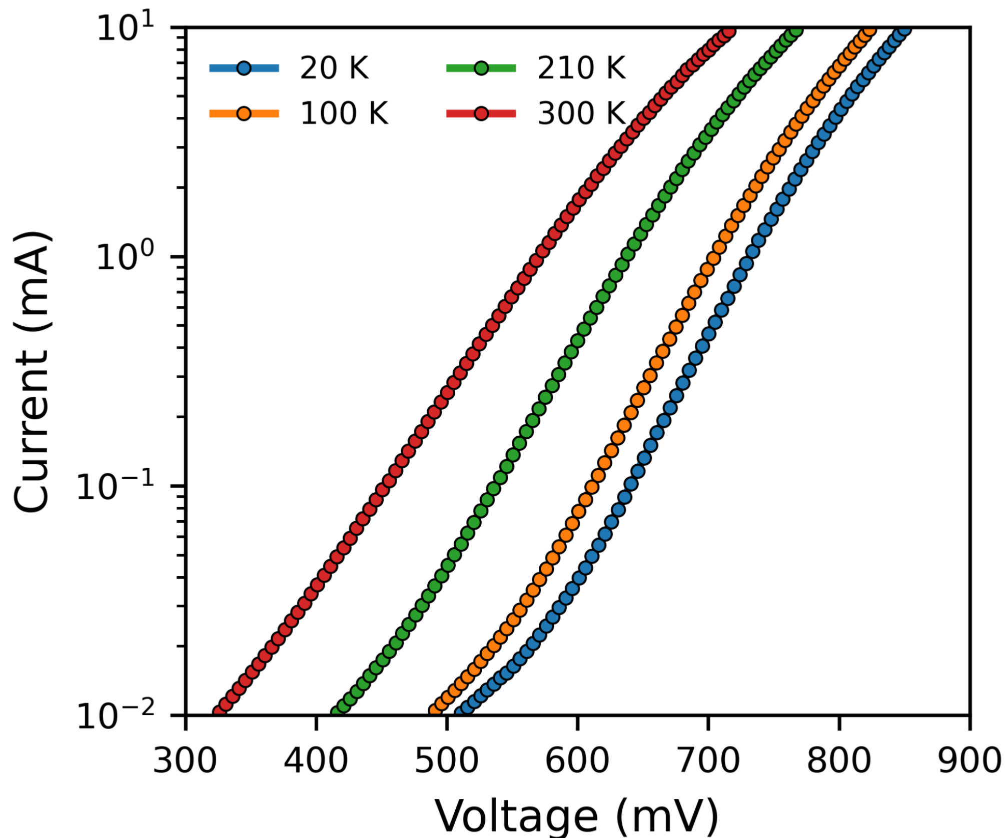

Figure 4.6: Measured forward I-V characteristics of the HEMT at different base temperatures (colored symbols). We fit the temperature-dependence of the Schottky parameters for $I \lesssim 100$ μA for which $T_j \approx T$ and the diode characteristics are log-linear. The DC resistance is combined with S-parameter measurements to extract the junction temperature at the 0.5-9 mA biases for which self-heating occurs. Uncertainties in the measurements are sufficiently small that error bars are not visible.

junction temperature was extracted at biases ranging from 0.5 to 9 mA for which the capacitance of the channel depletion layer is negligible. In this current range, the frequency dependence of r_T is negligible up to 1 GHz, and the influence of the parasitic capacitances is negligible. For the calculation of the thermal resistance, we took the area of the gate to be 14 $\mu m^2 = 70$ nm $\times$ 200 μm.

4.4 Schottky I-V measurements

Figure 4.6 shows the measured forward bias DC I-V characteristics at different base temperatures. The form of the characteristic is qualitatively consistent with those

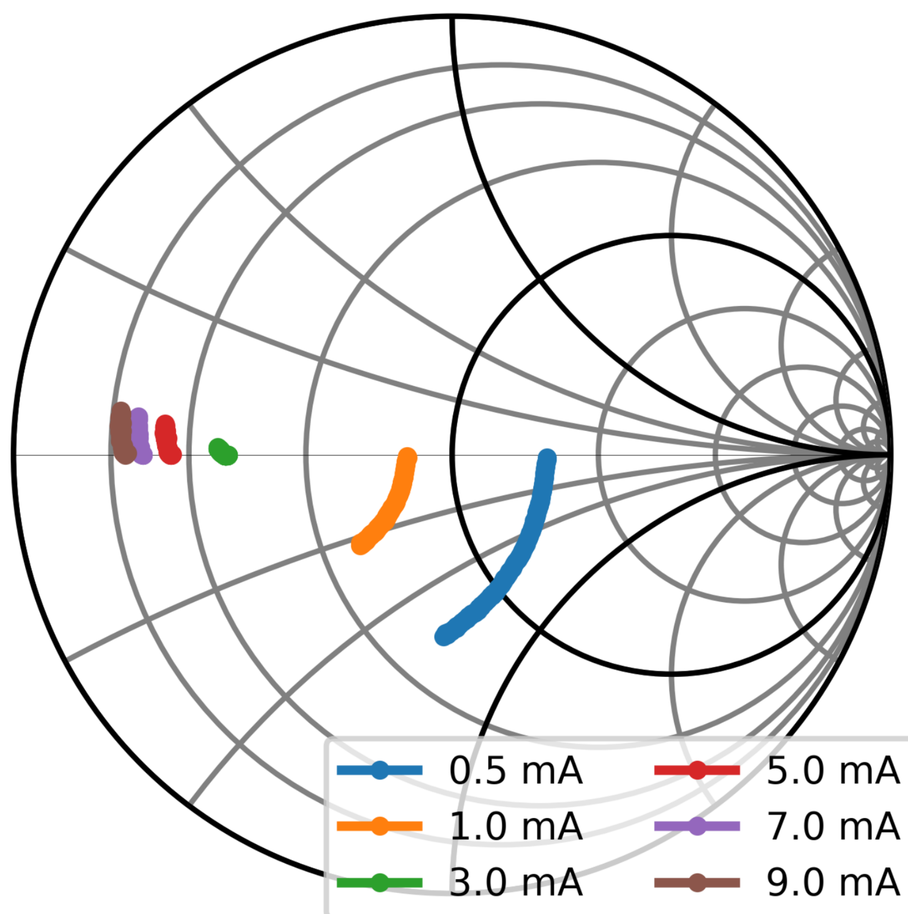

Figure 4.7: Small-signal reflection coefficient extracted from S-parameters at different bias points (colored markers) and T = 20 K from 1-10 GHz. The small-signal resistance is extracted by taking the real part of the input impedance.

from other low noise HEMTs reported in the literature (see Fig. 3c in Ref. [52]). The gate current is larger than the typical HEMT leakage current because the gate is forward-biased in the present experiments. As the device is cooled, the characteristics shift to higher threshold voltages but still exhibit a clear dependence on temperature. On a semilog plot such as shown here, the saturation current is obtained from the y-intercept of a linear fit to the log-linear region while the ideality factor is extracted from the slope $qV/\eta k_B T$ of the same region. The measured Schottky parameters were then used to fit the temperature dependence of the saturation current and ideality factor as discussed in Section 4.2.

Figure 4.7 shows the measured reflection coefficient S_{11} at various bias points at 20

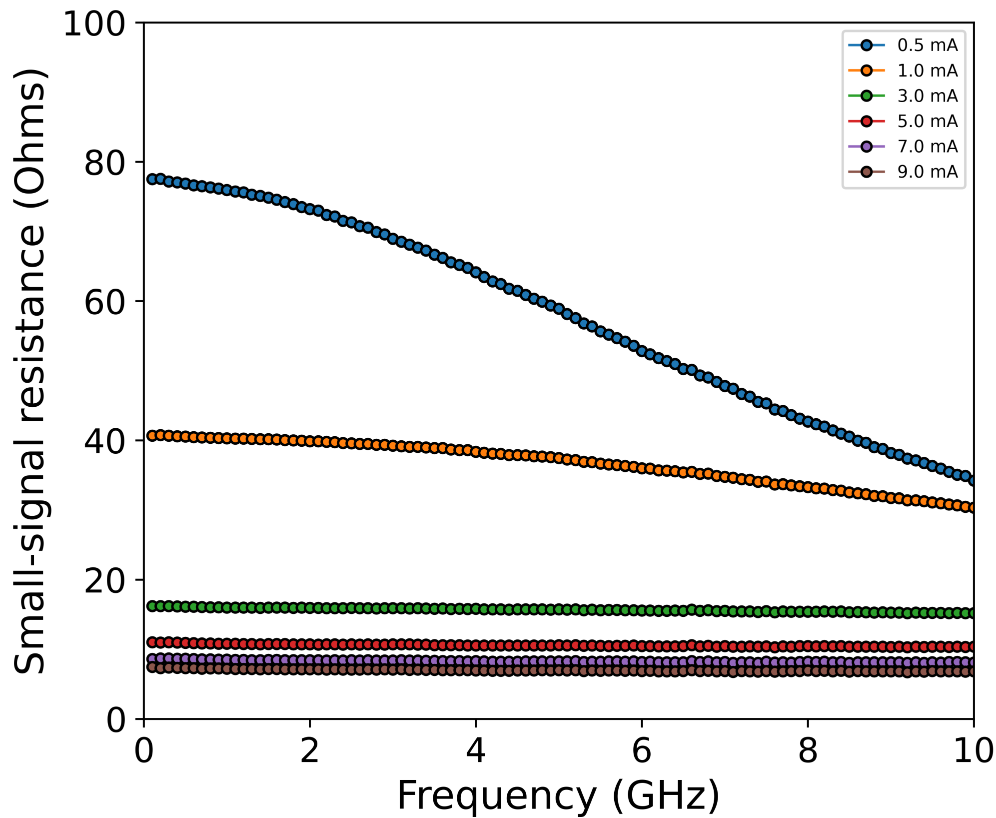

Figure 4.8: Small signal resistance extracted from S-parameters at different bias points (colored markers) and $T = 20$ K from 1-10 GHz. At low bias and high frequencies, the effect of the parasitic gate-source capacitance becomes apparent and the resistance drops off. To avoid this effect, the resistance is extracted only below 1 GHz where the capacitance is negligible. Uncertaintities in the measurement are sufficiently small that error bars are not visible.

K from 1-10 GHz. The small signal resistance is obtained from the reflection coefficient through $r_T = \mathrm{Re}[(1 + S_{11})/(1 - S_{11})Z_0]$ where $Z_0 = 50\ \Omega$ is the characteristic impedance of the system. As seen in Fig. 4.8, at low biases such as 0.5 mA and high frequencies > 2 GHz, parasitic capacitance in the gate manifests as a roll-off in the small signal resistance. To mitigate the influence of this effect, we extract the small signal resistance under 1 GHz where it is nearly frequency-independent. Combining the small signal resistance with the temperature-dependence of the Schottky parameters, we may solve Eqn. 4.5 for the junction temperature.

4.5 Qualitative modeling of I-V characteristics

Even before direct extraction of the junction temperature, qualitative evidence of self-heating can be obtained by inspecting the I-V characteristics. Ideal Schottky diodes exhibit log-linear I-V characteristics, but in practice deviations are observed owing to self-heating and parasitic series resistance. Series resistance leads to a sublinear log I-V while self-heating causes a superlinear trend (see Fig. 3 in Ref. [194]). These effects depend on bias as well as temperature, and their balance determines the trend of the measured I-V characteristic.

Figure 4.9 compares the measured I-V characteristics with those generated by an ideal Schottky model, a cold-diode model, and a model including self-heating with a constant thermal resistance R_{th}. The ideal Schottky model neglects series resistance and self-heating and consequently exhibits log-linear DC characteristics at all biases. The cold-diode model incorporates the series resistance but neglects self-heating so that the junction temperature equals the base temperature at all biases, $T_j = T$. Finally, the linear-heating model incorporates series resistance, temperature-dependent Schottky parameters, and assumes that the junction temperature increases linearly with the dissipated power, $T_j = T + R_{th} IV$, with thermal resistance R_{th} as a fitting parameter. Through comparison to measured DC I-V, we can infer the magnitude and power dependence of the junction temperature T_j at different T.

Figure 4.9a shows the model comparison to measurements at $T = 300$ K. At low biases below 1 mA the measured diode is nearly ideal and exhibits the expected log-linear trend (Region A). At 1 mA, the cold-diode model, linear-heating model, and measured current agree to within 3%, indicating that the temperature rise at this bias is small compared to the base temperature. At high currents exceeding 1 mA, the series resistance leads to a sublinear trend (Region B); however, the cold-diode model including only series resistance underpredicts the measured current at high biases ($\sim$ 9 mA) by $\sim$ 25%. In contrast, the linear-heating model agrees with the measured I-V characteristics in Region B. From this comparison, we infer that at 300 K, self-heating is appreciable above 1 mA biases and that the thermal resistance is constant with power.

Figure 4.9b shows the model comparison at $T = 20$ K. As at 300 K, below 100 μA the diode is nearly ideal, but a super-linear trend associated with self-heating is evident at biases between 100 μA and 1 mA (Region C), which is not observed at 300 K. At 1 mA, the measured current exceeds that of the cold-diode model by over 15%, indicating that the temperature increase due to self-heating is substantially

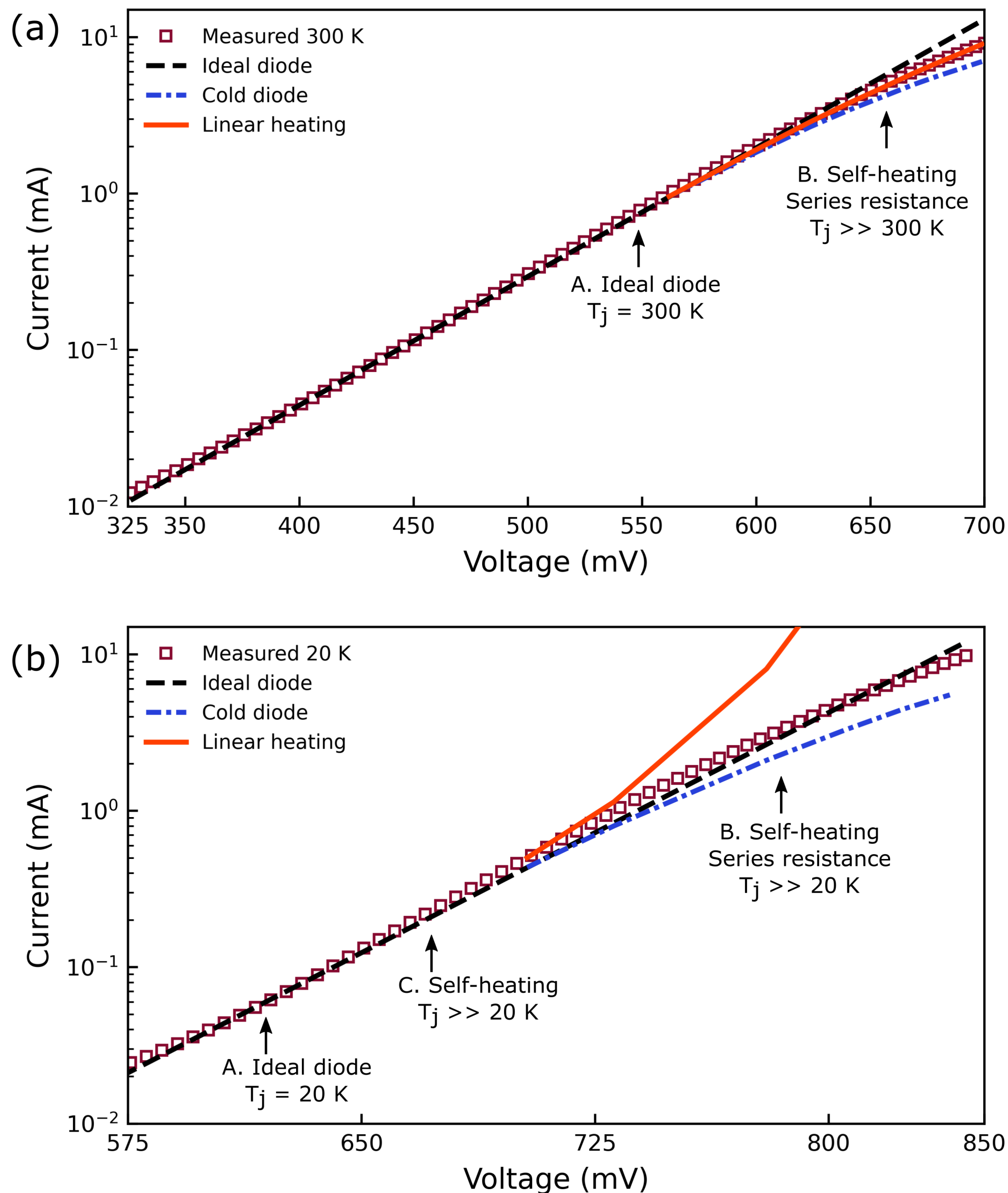

Figure 4.9: Measured *I*-*V* characteristics at **(a)** 300 K and **(b)** 20 K (red markers) compared to the ideal diode (black dashed line), cold diode (blue dashed dotted line), and linear-heating model (orange solid line). The cold-diode model captures the data well at low biases under 1 mA. A calculation assuming constant thermal resistance explains the high-bias measurements above 1 mA at 300 K but not at 20 K, implying the dominance of a different heat transfer mechanism at cryogenic temperatures. See text for additional details. The curves for cold diode model and linear heating model coincide with the ideal diode model below 0.5 mA and are omitted for clarity.

larger at this bias than at 300 K. Furthermore, above 1 mA (Region B) the linear-heating model at 20 K markedly overpredicts the measured current, indicating that the thermal resistance must decrease as the bias increases at 20 K.

4.6 Junction temperature extraction

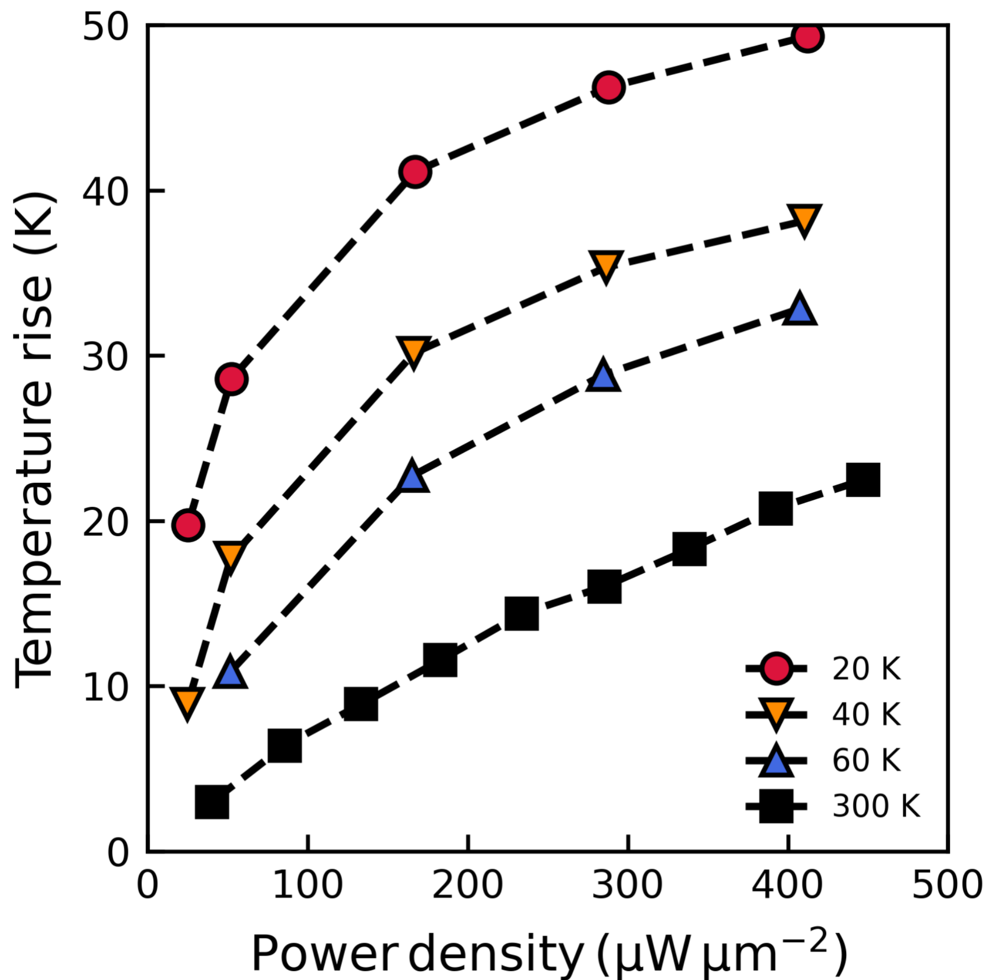

Figure 4.10: Junction temperature rise, $T_j - T$, versus dissipated power density at base temperatures 20 K (red circles), 40 K (yellow triangles), 60 K (blue triangles), and 300 K (black squares). The temperature rise is approximately linear with power at room temperature but nonlinear at cryogenic temperatures. Dashed black lines are added as guides to the eye.

We now perform a quantitative analysis of the data by using the method in Sec. 4.2 to extract the junction temperature. Figure 4.10 shows the extracted junction temperature rise versus power for T = 300 K, 60 K, 40 K, and 20 K. The features

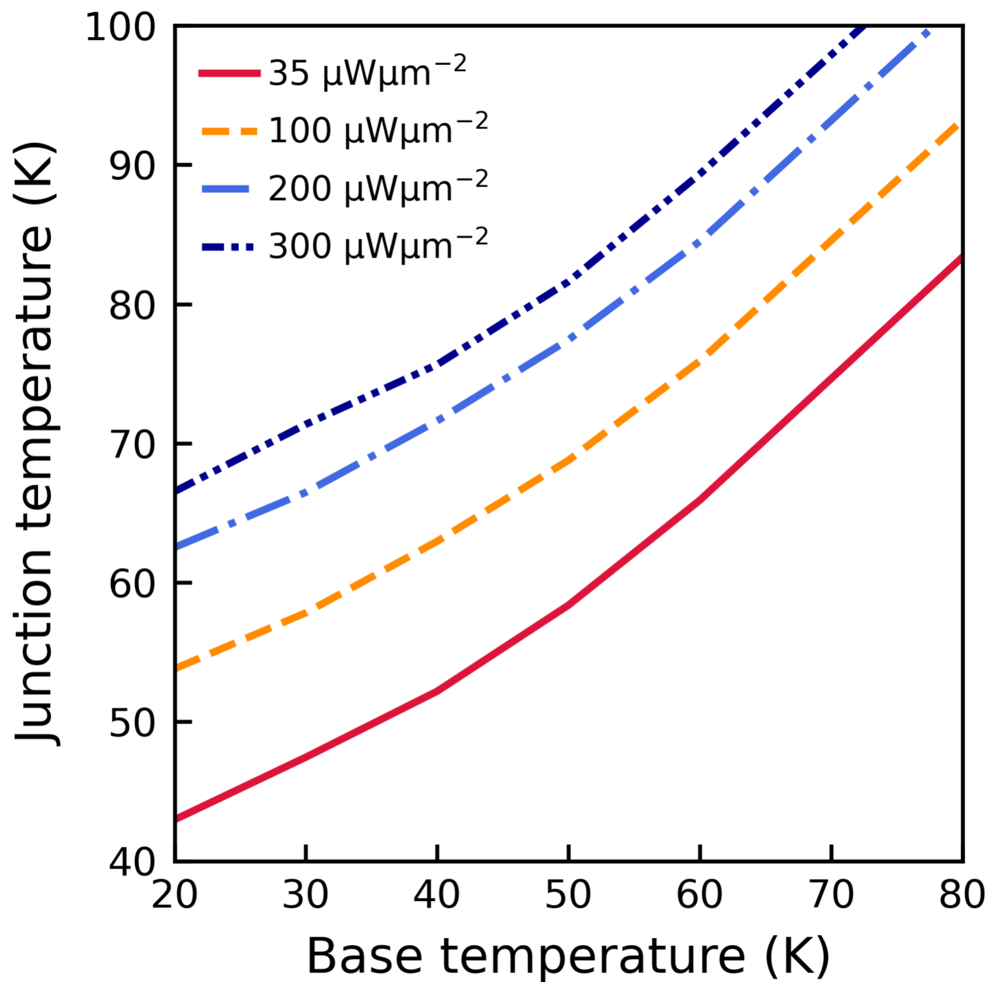

Figure 4.11: Interpolated junction temperature, T_j versus base temperatures, T at various power densities (colored lines). As the device is cooled, the junction temperature begins to plateau due to self-heating.

of the temperature rise are consistent with the qualitative expectations developed in Fig. 4.9. First, at T = 300 K, the temperature rise is nearly linear with the dissipated power, indicating that a constant thermal resistance can account for the measurements. Second, at the low bias point of 1 mA and 40 µW µm^{-2}, the junction temperature rise is 3 K or 1% of the base temperature, confirming the qualitative prediction of small temperature rise at this power shown in Fig. 4.9a. In contrast, at cryogenic temperatures, the temperature rise exhibits a nonlinear trend with power, with the temperature initially increasing rapidly but transitioning to a weaker increase at higher powers. This observation is consistent with Fig. 4.9b and suggests

that the thermal resistance decreases as the bias is increased. At $T = 20$ K and the same low bias point of 1 mA and 50 μW μm^{-2}, the temperature rise is 29 K, almost 10 times larger than the room temperature value of 3 K. This difference is on the same order as the difference in heat capacity between these temperatures, which decreases by over an order of magnitude from 300 K to 20 K [202]. At $T =$ 40 K and 60 K, the temperature rise exhibits the same qualitative features as those seen at 20 K, but for the same power, the temperature rise is smaller at higher base temperatures.

As described in Sec. 4.2, the junction temperature is extracted for fixed gate current values. To extract the temperature dependence of the junction temperature at fixed power instead of current, we linearly interpolate the junction temperatures for each power density. This procedure is analogous to taking a vertical slice at fixed power in Fig. 4.10. Figure 4.11 shows the interpolated junction temperature versus the base temperature for various power densities applied to the gate. At base temperatures near 80 K and all powers, the junction temperature decreases with base temperature as $\Delta T_j/\Delta T \sim 0.9$ K/K, meaning that at these temperatures, a change in base temperature is exhibited nearly completely in the junction temperature as well. As the cryostat is cooled to 20 K, the cooling coefficient $\Delta T_j/\Delta T$ drops to ~ 0.45 K/K, indicating that while the bulk device continues to cool, the gate temperature cools less rapidly due to self-heating. The observed temperature plateau in Fig. 4.11 implies that the thermal resistance at all powers must increase nonlinearly as the junction temperature decreases below ~ 50 K.

4.7 Phonon radiation resistance

We now compute the thermal resistance $R_{th} = \Delta T/q$ as the ratio of the junction temperature rise in Fig. 4.10 and the power density. Figure 4.12 shows the thermal resistance versus power density. At room temperature, the thermal resistance is nearly constant with power, as expected from Figs. 4.9a and 4.10. As the device is cooled to cryogenic temperatures, the thermal resistance increases at all powers. At 1 mA and 40 μW μm^{-2}, the thermal resistance increases by almost an order of magnitude from 300 K to 20 K. Furthermore, at cryogenic temperatures the thermal resistance exhibits a nonlinear power dependence.

The magnitude and trend of the thermal resistance with temperature are inconsistent with a conduction thermal resistance associated with the thermal conductivity of the epitaxial semiconductor materials. For example, the conduction thermal resis-

tance based on the bulk thermal conductivity of GaAs at $T = 20$ K is $L/\kappa \approx 0.5$ K μm^2 mW^{-1} for $\kappa = 2000$ W m^{-1} K^{-1} [202] and $L = 1$ μm, orders of magnitude smaller than the observed resistance. If this thermal resistance was the dominant contributor, the temperature rise at 20 K and 1 mW would be only 0.03 K, which is far smaller than the extracted temperature rise. Even with accounting for large thermal gradients by taking the value at an intermediate temperature of 100 K, $\kappa = 200$ W m^{-1} K^{-1}, the estimated temperature rise is only 0.3 K. The lower thermal conductivity of the alloy is also unable to explain the discrepancy.

In addition to this magnitude discrepancy, bulk conduction cannot explain the temperature trend exhibited in the measurements. While the conduction thermal resistance is predicted to decrease by around an order of magnitude from 300 K to 20 K based on the temperature dependence of the thermal conductivity ($\kappa_{20\,K}/\kappa_{300\,K} \approx 40$ [202]), the opposite trend is observed in the measurements where the thermal resistance actually increases at lower temperatures. This analysis indicates that the measured thermal resistance is not associated with the thermal conductivity of the semiconductors.

Instead, the resistance can be attributed to the thermal boundary resistance of the gate-semiconductor interface. The HEMT gate is formed by depositing a metallic stack consisting of metals such as Pt, Ti, and Au on the InAlAs barrier layer that has been subjected to semiconductor processing steps such as wet etching. At 300 K, reported values of thermal boundary conductance for a soft metal such as gold on semiconductor are in the range of 30-40 MW m^{-2} K^{-1} [203]. These studies used pristine interfaces for which the metal is evaporated directly onto a high-quality crystalline substrate. In contrast, the etching step in the fabrication of the gate leaves an amorphous region several nanometers thick at the gate-semiconductor junction (see Figure 4.11(a) in Ref. [204]). Prior measurements report that crystalline disorder can increase thermal boundary resistance by factors of approximately 3-4 (see Figure 7 in Ref. [205]) as phonons with atomic-scale wavelengths are reflected at the interface [45]. At 300 K, the average thermal resistance of the HEMT over all power levels is 60 K μm^2 mW^{-1}. This value corresponds to a conductance of 17 MW m^{-2} K^{-1}, which is consistent with the above values for thermal conductance of a defective interface.

We next examine the origin of the nonlinear trend of thermal resistance versus power in Fig. 4.12. Assuming the total gate thermal resistance is dominated by the thermal boundary resistance, in principle a microscopic model of thermal bound-

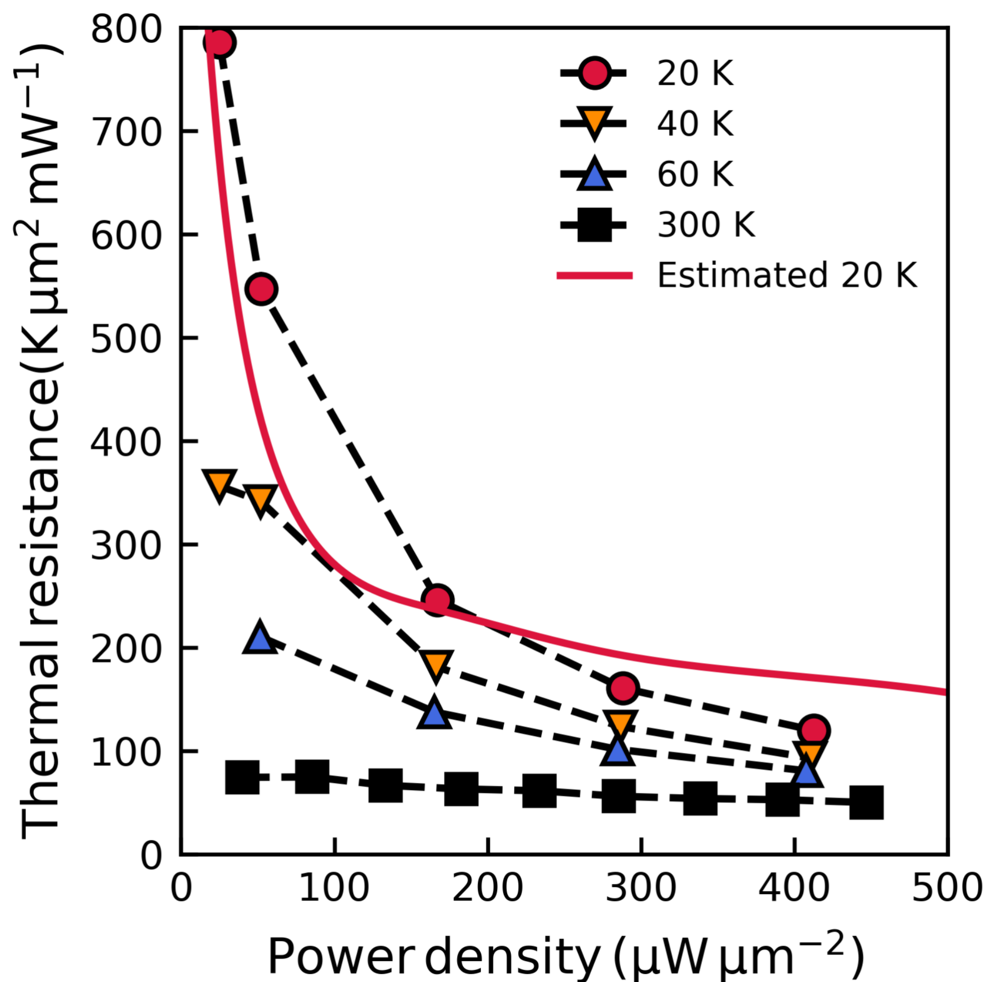

Figure 4.12: Thermal resistance of the junction versus power density at base temperatures of 20 K (red circles), 40 K (yellow triangles), 60 K (blue triangles), and 300 K (black squares). At room temperature, the thermal resistance is nearly independent of power and thus junction temperature. At cryogenic temperatures, the thermal resistance increases nonlinearly as the power and junction temperature decrease. While diffusion theory is not able to explain these trends, the features of the measurement are qualitatively consistent with the predictions of a simple model assuming the thermal resistance is dominated by phonon radiation through the interface (computed at 20 K, red solid line). Dashed black lines are added as guides to the eye.

ary resistance could be constructed from thermal resistance versus temperature and knowledge of the phonon density of states of the semiconductor and metal. However in practice, the bake and passivation steps in the gate fabrication induce atomic dif-

fusion and the formation of intermetallic compounds [204]. As a result, knowledge of the atomic structure and vibrational modes of the interface required for such a model is lacking.

Considering these challenges, we instead construct a qualitative model for the thermal resistance in which the phonons are assumed to follow a Debye model. The heat flux through the interface can be expressed in terms of the Debye density of states $D(\omega)$ as:

$$q = \frac{1}{4}\int_0^{\omega_D} \xi(\omega)D(\omega)\,\hbar\omega(f_{BE}(T_j) - f_{BE}(T))\,d\omega \tag{4.6}$$

where $\xi(\omega)$ is the frequency-dependent transmission through the interface and $f_{BE}(T)$ is the Bose-Einstein distribution evaluated at temperature T. With an appropriate change of variables $u = \hbar\omega/k_B T$, and assuming the temperature dependence of the transmission can be neglected, the integral can be recast into a more convenient form:

$$q = \frac{3k_B^4}{8\pi^2 c^2 \hbar^2}(T_j^4 - T^4)\int_0^{u_D} \xi \frac{u^3}{e^u - 1}du \tag{4.7}$$

where $u_D = \theta_D/T$ is the ratio of the Debye temperature associated with atomic vibrations at the interface and the temperature. Assuming that the temperature is small compared to the Debye temperature such that the upper bound of the integrand can be set to infinity, the integral becomes the Rienmann-Zeta function and can be evaluated analytically. The resulting expression is the solid-state equivalent of the Stefan-Boltzmann law [206]:

$$q = \epsilon\sigma_p(T_j^4 - T^4) \tag{4.8}$$

where ϵ is the integrated transmission coefficient associated with phonons impinging on the interface [207] and $\sigma_p = \pi^2 k_B^4/40\hbar^3 v_{ave}^2 \sim 600\ \mathrm{W\,m^{-2}\,K^{-4}}$ is the Stefan-Boltzmann constant for phonons in GaAs. Here, $v_{ave} \approx 3500\ \mathrm{m\,s^{-1}}$ is the Debye velocity in GaAs computed from the average sound velocities [202]. If the gradient of temperatures across the junction is small, that is if $T_j - T \ll T$, one obtains the familiar T^{-3} dependence of the thermal resistance. However for the large temperature rise depicted in Fig. 4.10, this linearization is inappropriate. Instead, a large signal thermal resistance can be defined by factoring the quartic term [208]:

$$R_{th}^{-1} = \epsilon\sigma_p\,(T_j + T)(T_j^2 + T^2). \tag{4.9}$$

Physically, the power dependence of the measured thermal resistance observed in Fig. 4.12 can be interpreted microscopically through this model. The value of the radiation resistance depends on the number of available heat conduction channels, parameterized by the phonon occupation. At room temperature, where phonon modes are classically occupied, the occupation of the modes does not vary strongly with temperature and consequently, the thermal resistance is nearly constant with power. In contrast, at sufficiently low temperatures, the phonon Bose-Einstein occupation depends strongly on temperature and consequently the observed resistance is a strong function of the dissipated power. Applying this model to the data measured at 20 K, we obtain the curve shown in Fig. 4.12. Despite the simplicity of the phonon radiation model, it qualitatively captures the nonlinear variation of thermal resistance with power with $\epsilon \sim 0.02$ as the best fit parameter. The physical picture of heat dissipation from the gate that emerges is therefore the radiation of phonons from the gate with a heat flux that is smaller than the pure radiation value owing to phonon reflections at the gate-semiconductor interface.

4.8 Phonon radiation at the low noise operating point

We now discuss the implications of heat dissipation by phonon radiation on the self-heating and microwave noise figure of HEMTs. In the present experiments, the gate was forward-biased while the drain was grounded so that heat was generated by the emission of phonons by hot electrons in the gate metal. However, under the typical low noise operating conditions for depletion-mode HEMTs, the gate and drain are reverse and forward biased, respectively, and heat is generated by the emission of phonons from hot electrons flowing through the channel. Despite these differences, the identification of the phonon radiation mechanism supported by the measurements in this study allows us to assess the magnitude of self-heating at the low-noise operating bias. Considering heat transport to occur by phonon radiation, at the low-noise bias phonons generated in the channel radiate to the gate which then radiates phonons to the substrate to balance the incoming heat flux. The steady-state temperature of the gate is set by the radiation space resistances between the gate, channel, and substrate.

An equivalent radiation circuit model for the system, as shown in Fig. 4.13, can be used to predict the temperature rise in the gate from the radiative phonon flux originating at the drain (see Eqn. 6.48 and Fig. 6.12 of Ref. [209]). In this model, the three nodes in the circuit are the channel (c), gate (g), and substrate (s) linked by space radiation resistances. We assume that all surfaces are black for simplicity. The

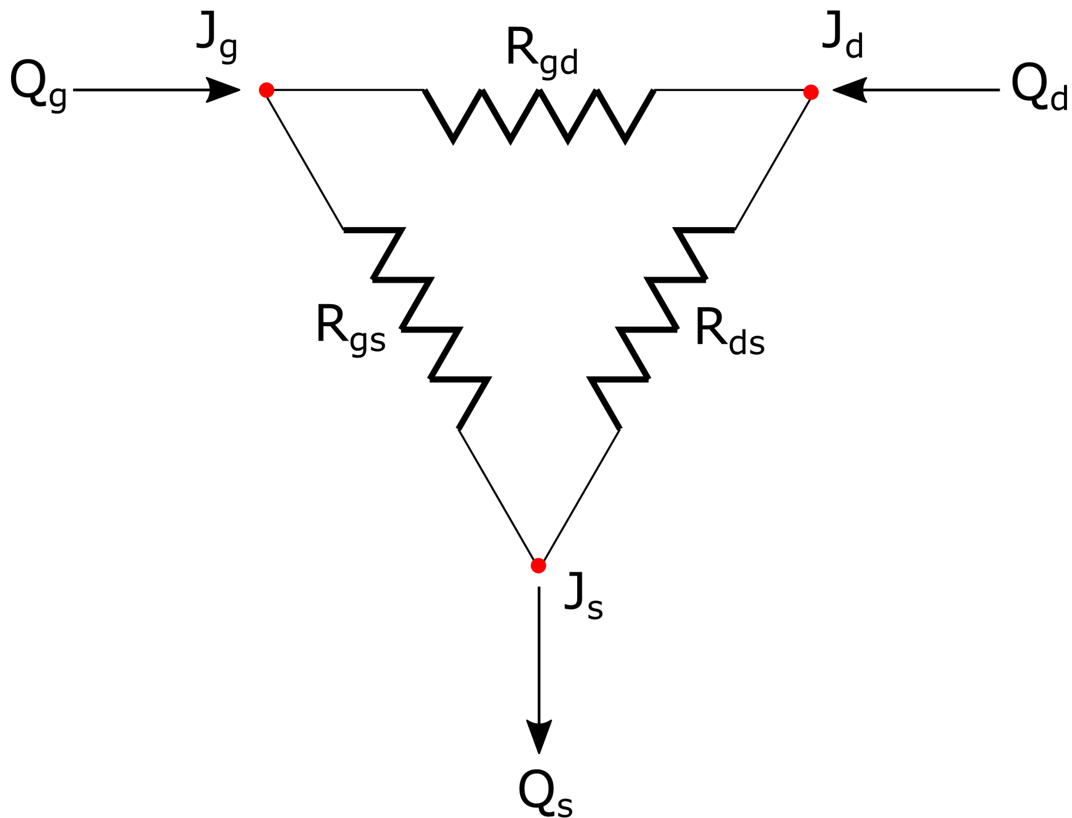

Figure 4.13: Equivalent thermal circuit model of the cryogenic HEMT at the low noise operating point. Under the phonon blackbody regime, the source, gate, and channel are linked by radiation space resistances. Under the appropriate approximations, this circuit can be solved for the gate and channel temperatures as a function of channel dissipation and substrate temperature.

gate node is assumed to be adiabatic such that all absorbed radiation is re-emitted. This assumption is well-justified since the only other mode of heat transfer available to the gate is conduction through the thickness of the gate itself. The contribution of this path can be easily estimated by Fourier's Law with the cryogenic thermal conductivity of gold as $\kappa \approx 10\,\mathrm{W\,m^{-1}\,K}$, the cross sectional area of the gate as 0.15 $\mu\mathrm{m}^2$, and a relevant length scale on the order of 50 µm. With these values, we predict a conductive heat loss out of the gate of $\sim$ 150 nW, which is indeed significantly smaller than the typical dissipation in HEMTs of order $\sim$ mW (see Supplementary Information in Ref. [72]).

Under these assumptions, the gate emissive power J_g can be expressed as:

$$J_g = \frac{J_d R_{cg} + J_c R_{gs}}{R_{cg} + R_{gs}} \tag{4.10}$$

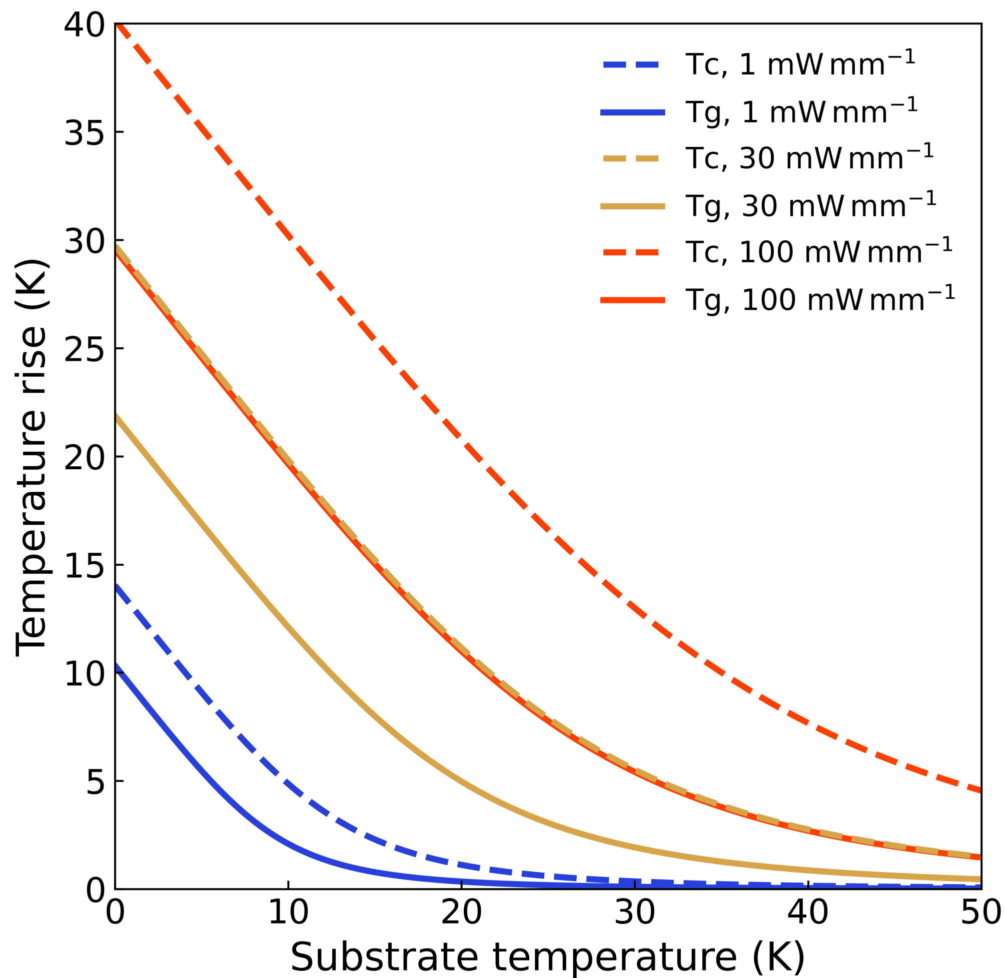

Figure 4.14: For a given substrate temperature and channel dissipation, the radiation circuit is solved for the gate and channel temperatures, here plotted as temperature increase relative to the substrate. At high substrate temperatures > 50 K, the temperature rise at all biases is a small fraction of the substrate temperature. However at liquid helium temperatures, the temperature rise at even small biases may be several times the substrate temperature. For typical HEMT parameters, the temperature rise in the gate is approximately 2/3 of that in the channel.

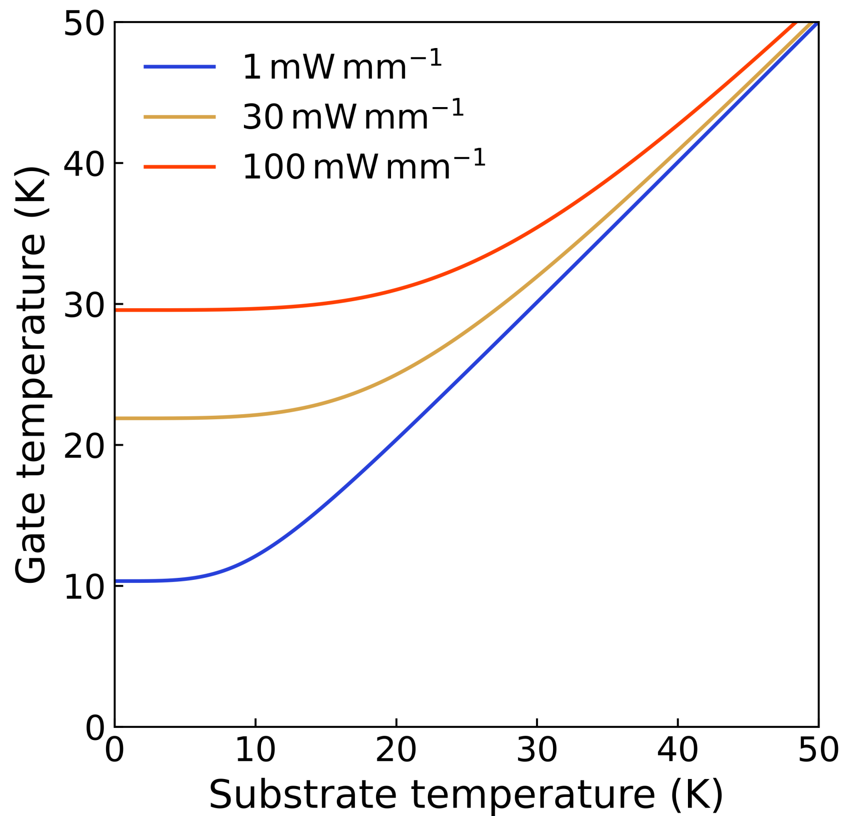

Figure 4.15: The simulated gate temperature under low noise bias conditions for the typical HEMT geometry. At high temperatures > 50 K, decreasing the substrate temperature by 1 K produces almost an equivalent decrease in the gate thermal noise. However as the substrate temperature continues to decrease, the gate becomes thermally decoupled from the substrate. At liquid helium temperatures, the thermal noise from the gate may be several times larger than that predicted by the substrate temperature.

where $R_{ij} = A_i F_{ij}$ is the space resistance between nodes i and j, A_i is the emitting line length, F_{ij} is the view factor, and $J_i = \sigma_p T_i^4$ is the blackbody emissive power from node i at temperature T_i. Balancing the heat fluxes in the equivalent circuit model, we obtain an expression for the the heat flux Q_c in the channel:

$$Q_c = (J_c - J_g)/R_{cg} + (J_d - J_s)/R_{cs}. \tag{4.11}$$

For a specified substrate temperature $T_s = T$ and power density from Joule heating in the channel, Eqns. 4.10 and 4.11 can be solved for the gate and channel temperatures T_g. Based on typical HEMT geometry, we estimate emitting line lengths as $A_g = A_c \sim 70$ nm. The view factor is estimated from the intercept of the 2D solid angle of the gate from the emitter region in the channel. For a typical HEMT gemometry, we obtain $F_{cg} \sim 0.3$. The results of the calculation for different power dissipations are shown in Fig. 4.14.

At a typical low-noise bias, the dissipated power is ~ 30 mW mm^{-1} [72]. Note that this dissipated power is that at the low noise bias, which is distinct from the powers used in the experiments of Sec. 4.2. As seen in Fig. 4.15, for a base temperature $T = 20$ K, numerical solution of Eqn. 4.10 predicts a gate temperature ~ 24 K, consistent with the finding of Ref. [75]. However, taking $T = 4$ K, the temperature rise in the gate is ~ 16 K and consequently, the gate temperature is predicted to equal 20 K. As is apparent from Fig. 4.15, the trend is not specific to a particular choice of dissipation. At high temperatures $T > 50$ K, the temperature rise is small relative to the substrate and cooling the substrate produces an almost equivalent decrease in the gate temperature. In contrast, at low temperatures < 30 K, the gate thermally decouples from the substrate due to self-heating and indeed at liquid helium temperatures, saturates altogether. Consequently, at the typical operating point for low noise amplifiers, the gate is predicted to be several times hotter than the substrate.

The self-heating of the gate affects the microwave noise of HEMTs because the thermal noise associated with the gate resistance is added at the input. If the steady-state gate temperature exceeds the base temperature, the microwave noise will be larger than predicted based on the base temperature. The above analysis implies that the thermal noise contribution of the HEMT gate at liquid helium temperatures is several times larger than previously assumed. An incorrect gate temperature directly affects the extracted drain temperature and consequently the interpretation of the

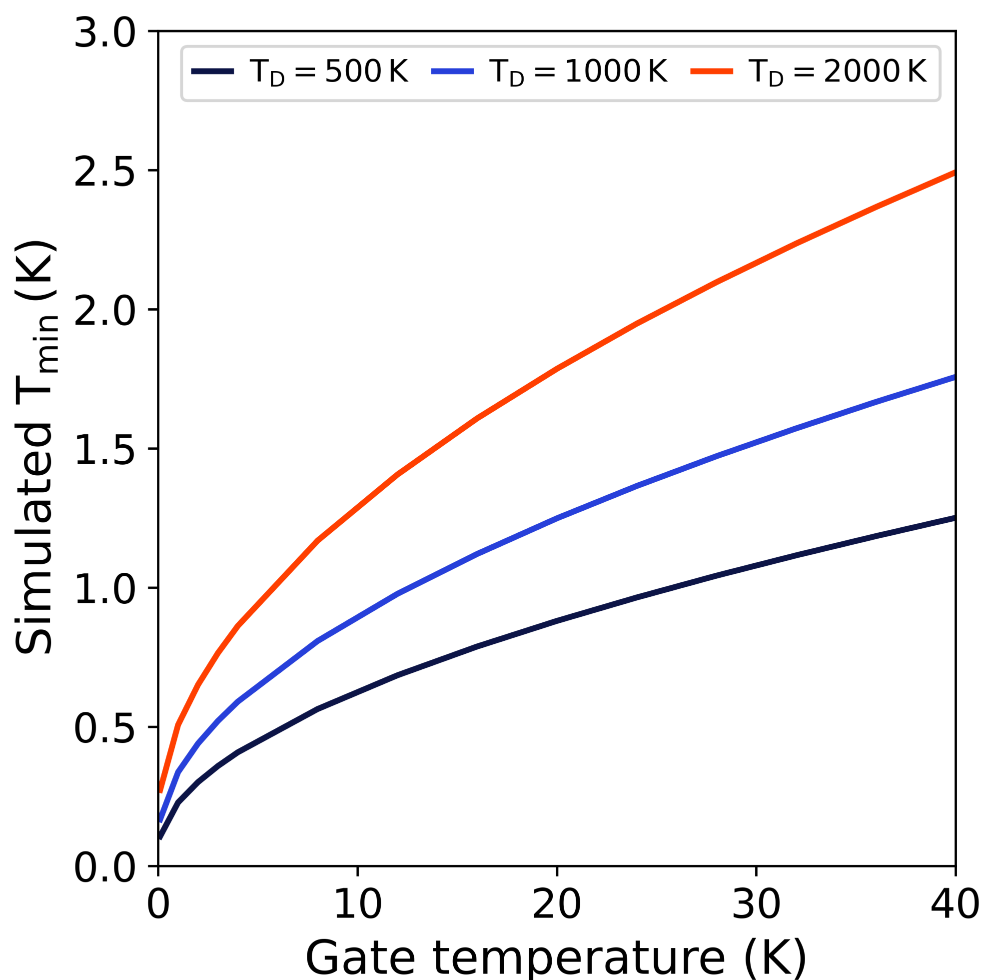

Figure 4.16: The simulated dependence of the Pospieszalski minimum noise temperature T_{min} on the gate temperature of the amplifier at substrate temperature 100 mK. Linear transistor model available from OMMIC D007IH PDK. Small-signal transistor elements obtained from [198]. Improvements in thermal management will be necessary to reduce the contribution of the gate to the minimum noise temperature of the transistor.

physical origin of noise in HEMTs. We note that previous work has interpreted noise saturation at liquid helium temperatures to the saturation of the drain noise added at the output (see Fig. 1d of Ref. [72]). Our measurements indicate that the observed noise saturation is in fact due to elevated thermal noise at the input as the gate temperature plateaus with base temperature.

Figure 4.16 shows the simulated dependence of the Pospiszalski minimum noise temperature for the transistor as a function of the gate temperature for different values of the drain temperature. This figure indicates that self-heating will limit the minimum noise temperature of cryogenic HEMT amplifiers without decreases in power consumption or improvements in device thermal management that decrease the physical temperature of the gate. Recently, LNAs with power consumption of hundreds of μW were reported, a value that is several times lower than those of typical HEMTs [52]. While these reductions can reduce gate heating, the quartic dependence associated with phonon radiation means that even at 300 μW and T = 100 mK, the gate temperature is predicted to be ∼ 10 K. Therefore, additional considerations for thermal management are necessary to reduce the excess thermal noise resulting from self-heating. A possible strategy is to introduce an additional thermal path above the gate using direct immersion in normal or superfluid liquid helium, which is routinely done for thermal management of superconducting magnets in high-energy physics experiments [210].

We have presented measurements of the gate junction temperature and thermal resistance of a low-noise HEMT from cryogenic to room temperature obtained using a Schottky thermometry method. The magnitude and trend of the extracted thermal resistance versus power and base temperature are consistent with heat dissipation by phonon radiation through an interface. Considering phonon radiation as the dominant mechanism of heat transfer, we estimate the intrinsic temperature of the gate at the low-noise operating bias using a radiation circuit. The model predicts that at liquid helium temperatures, the gate will self-heat to a temperature several times that of the base temperature. Our measurements thus indicate that self-heating constitutes a practical lower limit for the minimum microwave noise figure of cryogenic HEMT amplifiers unless thermal management strategies to remove heat from the gate can be identified.

Chapter 5

SUMMARY AND OUTLOOK

The overarching goal of this thesis has been to contribute to the development of physical models for electronic fluctuations in semiconductor materials and devices. In this thesis, we have studied electronic noise in semiconductors through a combination of first-principles simulations and experiments in HEMT transistor amplifiers. Our work has provided new and unique perspectives on both the physics of fluctuations in materials and how fluctuations in devices limit modern scientific instrumentation. In this chapter, we highlight the key contributions of this work and identify areas of future interest.

In Chapter 2, we introduced a new *ab intitio* theory of fluctuations in semiconductors through the framework of the Boltzmann Transport Equation. In contrast to earlier simulation techniques used to study noise, our method is truly first-principles and therefore requires no *ad hoc* parameters. Therefore our method provides a means of moving beyond the phenomenological descriptions of materials allowing us to identify the microscopic mechanisms responsible for electronic fluctuations in a predictive manner. Building on earlier work developed for the prediction of transport properties, our method moves beyond the typical warm electron approximation to permit the calculation of transport and fluctuation properties for charge carriers that have been excited well above the lattice temperature. The key output of the method is the fluctuation power spectral density. Under non-equilibrium conditions, this observable contains information about the magnitude and timescales of competing microscopic processes that are not accessible through transport studies alone.

In Chapter 3, we demonstrate the method by simulating noise in two technologically relevant semiconductors. In the first study in GaAs, we investigate the transport and fluctuation properties of warm electrons in GaAs. The method enables a unique modal perspective of electronic noise in semiconductors and in this study, we have resolved the contributions of individual electronic states to current noise and identified the mechanism underpinning these contributions as the disparate time scales of energy and momentum relaxation between electrons and the lattice. In our second study in Si, we simulate transport and fluctuations of hot carriers and find that the widely-accepted 1ph scattering theory is insufficient to reproduce measurements

of the warm electron tensor and the PSD.The simulation work presented in Chapters 2 and 3 is an advance in the state of art for the numerical description of electronic noise relative to the Monte Carlo method that has dominated the field for the past 40 years. Just as *ab initio* methods have stimulated new research directions for linear transport, so too will our method enable microscopic insights on electronic noise in semiconductors that are not possible with traditional methods.

In Chapter 4, we investigate the role of heat dissipation as a fundamental mechanism limiting the noise performance of high electron mobility transistors at cryogenic temperatures. We address this important question using a Schottky thermometry method that combines DC and high frequency S-parameter measurements to characterize the junction temperature and thermal resistance of the gate in a cryogenic HEMT. Our measurements support the physical picture of heat transported by phonon radiation through a defective interface at the gate-semiconductor interface, resulting in a thermal resistance that is orders of magnitude larger than that predicted by Fourier's Law. Importantly, this result implies that self-heating will be appreciable for any realistic low-noise bias at liquid helium temperatures, limiting the minimum thermal noise and hence overall noise figure of modern cryogenic HEMTs.

5.1 Future work

The *ab initio* theory of electronic noise and the applications in GaAs and Si presented in this thesis may be used as a baseline for the development of more sophisticated simulations. The theory presented in this dissertation is developed for the study of spatially homogeneous fluctuations driven by phonon-mediated scattering events. Incorporating the real-space dependence of fluctuations can enable the prediction of the charge density fluctuations that drive phenomena such as light scattering. In the case of electronic noise, our computed observable was the spectral density of fluctuations in the electronic current. The analogous quantity in a light scattering study would be the fluctuations of the dielectric constant of the material. In such a study, the incorporation of carrier-carrier interactions is necessary to reproduce experimental measurements. In principle, such calculations are an extension of the present method with an additional term in both the one-time, two-particle correlation function and in the collision operator of the BTE and with the full spatial derivative included in the kinematic portion of the equation (see Ch. 2 of [4]).

Another potentially interesting extension of the method is the inclusion of impurity-mediated scattering. This effect is particularly relevant for modeling doped semicon-

ductors at low temperatures, where electrons scatter from the local charge imbalances induced by ionized impurities. Traditionally, the influence of ionized impurities has been treated using semiempirical models such as Brooks-Herring [19]. Such models fail to incorporate important effects such as anisotropy and energy dependence of the scattering rates. Recently published work has developed a framework for the *ab initio* computation of electron-defect scattering rates [211, 212] and demonstrated that in contradiction to previous assumptions, these rates are highly energy and temperature dependent. Incorporating these calculations with the present method could potentially lead to better understanding of fluctuations in real devices such as MOSFETs and bipolar junction transistors that rely heavily on doping to promote charge transport.

At present, the developed method simulates the dynamics of the charge carriers interacting with a reservoir of phonons in thermal equilibrium. This approximation is likely appropriate when the electron heating is limited or for simulations in materials where the time-constants of phonon-phonon scattering are substantially faster than the analogous electron-phonon processes. In real devices, charge carriers are routinely excited many $k_B T$ above the conduction band edge. Under such conditions, the energy transferred to the lattice may be sufficient to drive phonons out of equilibrium. Since the primary mode of electron energy dissipation is optical phonons, the buildup of non-thermal optical phonon occupation can present a significant bottleneck to carrier cooling [213]. Consequently, in systems such as the 2DEG channels of HEMT amplifiers, one may need to incorporate hot phonon effects to fully capture energy transfer rates [214]. One method to incorporate hot phonon effects is the simultaneous solution of coupled electron and phonon Boltzmann Equations [215]. Conventionally, such methods have been computationally expensive, but recently developed numerical simulators may enable direct calculations [216].

The present method may also be applied to study other interesting materials. In Chapter 3 of this dissertation, we demonstrated that the properties of the conduction band structure in a given material are an important determinant of the presented noise characteristics. The conduction band of graphene is characterized by a linear Dirac cone and a gapless transition to the valence band at the minima. The unique structure of graphene is thought to contribute to novel transport properties [217, 218] and it may have similar influence over fluctuations in the material. A recent study [219] based on the Boltzmann-Greens function method of Stanton and Wilkins [114] simulated the current spectral density of graphene at room temperature. However,

this study used a toy-model band structure and a relaxation time approximation of the scattering. As such, the insights derived from this study are necessarily qualitative and no comparison to experiment was attempted. As first-principles calculations of the electronic structure and lattice dynamical properties of graphene are now available [220], the present theory can be easily applied to further understanding of fluctuations in graphene.

Finally, it is natural to consider how our findings may contribute to the development of next generation low noise amplifiers. The Schottky thermometry methods presented in Chapter 5 suggest that at under the conditions typical for low noise operation, excess thermal noise in the gate will limit the overall noise performance of HEMT amplifiers. Further improvements to HEMT LNAs will require changes to the device structure or operating conditions that mitigate the self-heating of the gate. The analysis presented in Fig. 4.14 suggests that minimizing the power dissipation in the channel will reduce the thermal contribution of the gate. In recent years, much effort has been dedicated to reduce HEMT power dissipation, largely motivated by a desire to reduce heat load on the cryogenic stages of quantum computing and radio astronomy measurement platforms. For example, a recent study has demonstrated that tuning the composition of the alloy channel can improve HEMT noise performance at sub-mW dissipation [52]. While the study has attributed the low noise temperature to increase in the threshold frequency and reduction in the drain temperature, employing the Schottky thermometry method proposed in this thesis would allow a direct breakdown of the measured noise into thermal and hot electron components. Repeating the analysis performed in our study can therefore contribute to greater understanding of the present noise sources and inform future optimization steps.

BIBLIOGRAPHY

1. Ziel, A. V. d. *Noise in Solid State Devices and Circuits* (Wiley, 1986).
2. Pospieszalski, M. W. *On the Dependence of FET Noise Model Parameters on Ambient Temperature* in *2017 IEEE Radio and Wireless Symposium (RWS)* (2017), 159–161.
3. Chen, G. *Nanoscale Energy Transport and Conversion: A Parallel Treatment of Electrons, Molecules, Phonons, and Photons* ISBN: 9780195159424 (Oxford University Press, 2005).
4. Gantsevich, S., Gurevich, V. & Katilius, R. Theory of Fluctuations in Nonequilibrium Electron Gas. *Riv. Del Nuovo Cimento* **2** (1979).
5. Kogan, S. *Electronic Noise and Fluctuations in Solids* (Cambridge University Press, Cambridge, 1996).
6. Nyquist, H. Thermal Agitation of Electric Charge in Conductors. *Phys. Rev.* **32.** https://link.aps.org/doi/10.1103/PhysRev.32.110, 110–113 (1 July 1928).
7. Callen, H. B. & Welton, T. A. Irreversibility and Generalized Noise. *Phys. Rev.* **83,** 34–40. https://link.aps.org/doi/10.1103/PhysRev.83.34 (1 July 1951).
8. Kubo, R. & Tomita, K. A General Theory of Magnetic Resonance Absorption. *J. Phys. Soc. Jpn.* **9,** 888–919. eprint: https://doi.org/10.1143/JPSJ.9.888. https://doi.org/10.1143/JPSJ.9.888 (1954).
9. Kubo, R. Statistical-Mechanical Theory of Irreversible Processes. I. General Theory and Simple Applications to Magnetic and Conduction Problems. *J. Phys. Soc. Jpn.* **12,** 570–586. eprint: https://doi.org/10.1143/JPSJ.12.570. https://doi.org/10.1143/JPSJ.12.570 (1957).
10. Lax, M. Generalized Mobility Theory. *Phys. Rev.* **109,** 1921–1926. https://link.aps.org/doi/10.1103/PhysRev.109.1921 (6 Mar. 1958).
11. Einstein, A. Über die von der molekularkinetischen Theorie der Wärme geforderte Bewegung von in ruhenden Flüssigkeiten suspendierten Teilchen. *Annalen der Physik* **322,** 549–560. eprint: https://onlinelibrary.wiley.com/doi/pdf/10.1002/andp.19053220806. https://onlinelibrary.wiley.com/doi/abs/10.1002/andp.19053220806 (1905).
12. Kirchhoff, G. in *Von Kirchhoff bis Planck: Theorie der Wärmestrahlung in historisch-kritischer Darstellung* (ed Schöpf, H.-G.) 131–151 (Vieweg+Teubner Verlag, Wiesbaden, 1860). ISBN: 978-3-663-13885-3. https://doi.org/10.1007/978-3-663-13885-3_10.
13. Price, P. in *Fluctuation Phenomena in Solids* (ed Burgess, R.) chap. 8 (Academic, New York, 1965).

14. Giustino, F. Electron-phonon interactions from first principles. *Rev. Mod. Phys.* **89.** https://link.aps.org/doi/10.1103/RevModPhys.89.015003, 015003 (1 Feb. 2017).

15. Fischetti, M. V. & Laux, S. E. Monte Carlo analysis of electron transport in small semiconductor devices including band-structure and space-charge effects. *Phys. Rev. B* **38,** 9721–9745. https://link.aps.org/doi/10.1103/PhysRevB.38.9721 (14 Nov. 1988).

16. Varshni, Y. Temperature dependence of the energy gap in semiconductors. *Physica* **34,** 149–154. ISSN: 0031-8914. https://www.sciencedirect.com/science/article/pii/0031891467900626 (1967).

17. Cardona, M. & Christensen, N. E. Acoustic deformation potentials and heterostructure band offsets in semiconductors. *Phys. Rev. B* **35,** 6182–6194. https://link.aps.org/doi/10.1103/PhysRevB.35.6182 (12 Apr. 1987).

18. Bardeen, J. & Shockley, W. Deformation Potentials and Mobilities in Non-Polar Crystals. *Phys. Rev.* **80,** 72–80. https://link.aps.org/doi/10.1103/PhysRev.80.72 (1 Oct. 1950).

19. Herring, C. & Vogt, E. Transport and Deformation-Potential Theory for Many-Valley Semiconductors with Anisotropic Scattering. *Phys. Rev.* **101,** 944–961. https://link.aps.org/doi/10.1103/PhysRev.101.944 (3 Feb. 1956).

20. Dacorogna, M. M., Cohen, M. L. & Lam, P. K. Self-Consistent Calculation of the q Dependence of the Electron-Phonon Coupling in Aluminum. *Phys. Rev. Lett.* **55,** 837–840. https://link.aps.org/doi/10.1103/PhysRevLett.55.837 (8 Aug. 1985).

21. Kohn, W. & Sham, L. J. Self-Consistent Equations Including Exchange and Correlation Effects. *Phys. Rev.* **140,** A1133–A1138. https://link.aps.org/doi/10.1103/PhysRev.140.A1133 (4A Nov. 1965).

22. Sholl, D., Steckel, J. A. & Sholl. *Density functional theory: A practical introduction* (Wiley, 2011).

23. Perdew, J. P. Climbing the ladder of density functional approximations. *MRS Bulletin* **38,** 743–750 (2013).

24. Baroni, S., Giannozzi, P. & Testa, A. Green's-function approach to linear response in solids. *Phys. Rev. Lett.* **58,** 1861–1864. https://link.aps.org/doi/10.1103/PhysRevLett.58.1861 (18 May 1987).

25. Bernadi, M. First-principles dynamics of electrons and phonons. *Eur. Phys. J. B* **89.** https://epjb.epj.org/articles/epjb/abs/2016/11/b160399/b160399.html (2016).

26. Mahan, G. *Condensed Matter in a Nutshell* (Princeton University Press, Princeton, 2011).

27. Cercignani, C. *The Boltzmann Equation and Its Applications* (Springer, 1988).

28. Poncé, S., Margine, E., Verdi, C. & Giustino, F. EPW: Electron–phonon coupling, transport and superconducting properties using maximally localized Wannier functions. *Computer Physics Communications* **209,** 116–133. ISSN: 0010-4655. https://www.sciencedirect.com/science/article/pii/S0010465516302260 (2016).

29. Giannozzi, P. *et al.* QUANTUM ESPRESSO: a modular and open-source software project for quantum simulations of materials. *J. Phys.: Condens. Matter* **21.** https://iopscience.iop.org/article/10.1088/0953-8984/21/39/395502/meta, 395502 (Sept. 2009).

30. Zhou, J. *et al.* Perturbo: a software package for ab initio electron-phonon interactions, charge transport and ultrafast dynamics. https://arxiv.org/abs/2002.02045 (2020).

31. Li, W. Electrical transport limited by electron-phonon coupling from Boltzmann transport equation: An ab initio study of Si, Al, and MoS_2. *Phys. Rev. B* **92.** https://link.aps.org/doi/10.1103/PhysRevB.92.075405, 075405 (7 Aug. 2015).

32. Lee, N.-E., Zhou, J.-J., Agapito, L. A. & Bernardi, M. Charge transport in organic molecular semiconductors from first principles: The bandlike hole mobility in a naphthalene crystal. *Phys. Rev. B* **97.** https://link.aps.org/doi/10.1103/PhysRevB.97.115203, 115203 (11 Mar. 2018).

33. Desai, D. C., Zviazhynski, B., Zhou, J.-J. & Bernardi, M. Magnetotransport in semiconductors and two-dimensional materials from first principles. *Phys. Rev. B* **103,** L161103. https://link.aps.org/doi/10.1103/PhysRevB.103.L161103 (16 Apr. 2021).

34. Liu, T.-H., Zhou, J., Liao, B., Singh, D. J. & Chen, G. First-principles mode-by-mode analysis for electron-phonon scattering channels and mean free path spectra in GaAs. *Phys. Rev. B* **95.** https://link.aps.org/doi/10.1103/PhysRevB.95.075206, 075206 (7 Feb. 2017).

35. Reggiani, L., Kuhn, T. & Varani, L. Noise and correlation functions of hot carriers in semiconductors. *Appl. Phys. A* **54,** 411–427 (1992).

36. Price, P. J. Intervalley Noise. *Journal of Applied Physics* **31.** https://doi.org/10.1063/1.1735782, 949–953 (1960).

37. Hooge, F. 1/f noise sources. *IEEE Transactions on Electron Devices* **41,** 1926–1935 (1994).

38. Hartnagel, H., Katilius, R. & Matulionis, A. *Microwave Noise in Semiconductor Devices* chap. 8 (John Wiley & Sons, New York, 2001).

39. Vogl, P. Microscopic theory of electron-phonon interaction in insulators or semiconductors. *Phys. Rev. B* **13,** 694–704. https://link.aps.org/doi/10.1103/PhysRevB.13.694 (2 Jan. 1976).

40. Kang, J. S., Li, M., Wu, H., Nguyen, H. & Hu, Y. Experimental observation of high thermal conductivity in boron arsenide. *Science* **361.** https://science.sciencemag.org/content/361/6402/575, 575–578. ISSN: 0036-8075 (2018).

41. Li, S. *et al.* High thermal conductivity in cubic boron arsenide crystals. *Science* **361.** https://science.sciencemag.org/content/361/6402/579, 579–581. ISSN: 0036-8075 (2018).

42. Tian, F. *et al.* Unusual high thermal conductivity in boron arsenide bulk crystals. *Science* **361.** https://science.sciencemag.org/content/361/6402/582, 582–585. ISSN: 0036-8075 (2018).

43. Zhang, A. P. *et al.* Correlation of device performance and defects in AlGaN/GaN high-electron mobility transistors. *J. Electron. Mater.* **32,** 388–394 (2003).

44. Veeraraghavan, S. & Fossum, J. Short-channel effects in SOI MOSFETs. *IEEE Transactions on Electron Devices* **36,** 522–528 (1989).

45. Hua, C., Chen, X., Ravichandran, N. K. & Minnich, A. J. Experimental metrology to obtain thermal phonon transmission coefficients at solid interfaces. *Phys. Rev. B* **95.** https://link.aps.org/doi/10.1103/PhysRevB.95.205423, 205423 (20 May 2017).

46. Pospieszalski, M. W. Modeling of noise parameters of MESFETs and MODFETs and their frequency and temperature dependence. *IEEE Transactions on Microwave Theory and Techniques* **37.** https://ieeexplore.ieee.org/document/32217, 1340–1350 (1989).

47. Bryerton, E. W., Morgan, M. & Pospieszalski, M. W. *Ultra low noise cryogenic amplifiers for radio astronomy* in *2013 IEEE Radio and Wireless Symposium* https://ieeexplore.ieee.org/document/6486740 (IEEE, 2013), 358–360.

48. Pospieszalski, M. W. Extremely low-noise amplification with cryogenic FETs and HFETs: 1970-2004. *IEEE Microwave Magazine* **6.** https://ieeexplore.ieee.org/document/1511915, 62–75 (2005).

49. Krantz, P. *et al.* A quantum engineer's guide to superconducting qubits. *Applied Physics Reviews* **6.** https://doi.org/10.1063/1.5089550, 021318. eprint: https://doi.org/10.1063/1.5089550 (2019).

50. Hornibrook, J. M. *et al.* Cryogenic Control Architecture for Large-Scale Quantum Computing. *Phys. Rev. Applied* **3.** https://link.aps.org/doi/10.1103/PhysRevApplied.3.024010, 024010 (2 Feb. 2015).

51. Chow, J. *et al.* Implementing a strand of a scalable fault-tolerant quantum computing fabric. **5.** https://www.nature.com/articles/ncomms5015 (2014).

52. Cha, E. *et al. A 300-μW Cryogenic HEMT LNA for Quantum Computing* in *2020 IEEE/MTT-S International Microwave Symposium (IMS)* https://ieeexplore.ieee.org/document/9223865 (IEEE, 2020), 1299–1302.

53. Arute, F. *et al.* Quantum supremacy using a programmable superconducting processor. *Nature* **574.** https://doi.org/10.1038/s41586-019-1666-5, 505–510 (Oct. 2019).

54. Caves, C. M. Quantum limits on noise in linear amplifiers. *Phys. Rev. D* **26,** 1817–1839. https://link.aps.org/doi/10.1103/PhysRevD.26.1817 (8 Oct. 1982).

55. Cha, E. *et al.* 0.3–14 and 16–GHz Wide-Bandwidth Cryogenic MMIC Low-Noise Amplifiers. *IEEE Transactions on Microwave Theory and Techniques* **66.** https://ieeexplore.ieee.org/document/8500350, 4860–4869 (2018).

56. Schleeh, J., Wadefalk, N., Nilsson, P., Starski, J. P. & Grahn, J. Cryogenic Broadband Ultra-Low-Noise MMIC LNAs for Radio Astronomy Applications. *IEEE Transactions on Microwave Theory and Techniques* **61.** https://ieeexplore.ieee.org/document/6403592, 871–877 (2013).

57. Tang, Y., Wadefalk, N., Morgan, M. A. & Weinreb, S. *Full Ka-band High Performance InP MMIC LNA module* in *2006 IEEE MTT-S International Microwave Symposium Digest* https://ieeexplore.ieee.org/document/4014824 (2006), 81–84.

58. Pospieszalski, M. W. *et al. Millimeter-wave, cryogenically-coolable amplifiers using AlInAs/GaInAs/InP HEMTs* in *1993 IEEE MTT-S International Microwave Symposium Digest* (1993), 515–518 vol.2.

59. Bryerton, E. W. *et al. A W-band low-noise amplifier with 22K noise temperature* in *2009 IEEE MTT-S International Microwave Symposium Digest* (2009), 681–684.

60. Varonen, M. *et al.* A 75-116-GHz LNA with 23-K noise temperature at 108 GHz. *Jet Propulsion Laboratory Technical Report.* https://trs.jpl.nasa.gov/handle/2014/43236 (2013).

61. Blundell, R. *et al.* A wideband fixed-tuned SIS receiver for 200-GHz operation. *IEEE Transactions on Microwave Theory and Techniques* **43,** 933–937 (1995).

62. Reck, T. J., Deal, W. & Chattopadhyay, G. *Cryogenic performance of HEMT amplifiers at 340GHz and 670GHz* in *2014 IEEE MTT-S International Microwave Symposium (IMS2014)* (2014), 1–3.

63. Kooi, J. W. *et al.* A Low Noise NbTiN-Based 850 GHz SIS Receiver for the Caltech Submillimeter Observatory. *International Journal of Infrared and Millimeter Waves* **21,** 1357–1373 (Sept. 2000).

64. Schleeh, J. *et al. Passivation of InGaAs/InAlAs/InP HEMTs using Al2O3 atomic layer deposition* in *IPRM 2011 - 23rd International Conference on Indium Phosphide and Related Materials* (2011), 1–4.

65. Lefebvre, E. *et al.* Gate-Recess Technology for InAs/AlSb HEMTs. *IEEE Transactions on Electron Devices* **56,** 1904–1911 (2009).

66. Malmkvist, M., Wang, S. & Grahn, J. V. Epitaxial Optimization of 130-nm Gate-Length InGaAs/InAlAs/InP HEMTs for High-Frequency Applications. *IEEE Transactions on Electron Devices* **55,** 268–275 (2008).

67. Heinz, F., Thome, F., Leuther, A. & Ambacher, O. *Noise Performance of Sub-100-nm Metamorphic HEMT Technologies* in *2020 IEEE/MTT-S International Microwave Symposium (IMS)* https://ieeexplore.ieee.org/abstract/document/9223783 (IEEE, 2020), 293–296.

68. Akgiray, A. H. *et al.* Noise Measurements of Discrete HEMT Transistors and Application to Wideband Very Low-Noise Amplifiers. *IEEE Transactions on Microwave Theory and Techniques* **61.** https://ieeexplore.ieee.org/document/6566114/footnotes, 3285–3297 (2013).

69. Cuadrado-Calle, D. *et al.* Broadband MMIC LNAs for ALMA Band 2+3 With Noise Temperature Below 28 K. *IEEE Transactions on Microwave Theory and Techniques* **65,** 1589–1597 (2017).

70. Chiong, C.-C., Wang, Y., Chang, K.-C. & Wang, H. Low-Noise Amplifier for Next-Generation Radio Astronomy Telescopes: Review of the State-of-the-Art Cryogenic LNAs in the Most Challenging Applications. *IEEE Microwave Magazine* **23,** 31–47 (2022).

71. Schleeh, J., Rodilla, H., Wadefalk, N., Nilsson, P. & Grahn, J. Characterization and Modeling of Cryogenic Ultralow-Noise InP HEMTs. *IEEE Transactions on Electron Devices* **60,** 206–212 (2013).

72. Schleeh, J. *et al.* Phonon black-body radiation limit for heat dissipation in electronics. *Nature Mater* **14.** https://www.nature.com/articles/nmat4126, 187–192 (2014).

73. Duh, K. H. G. *et al.* 32-GHz cryogenically cooled HEMT low-noise amplifiers. *IEEE Transactions on Electron Devices* **36.** https://ieeexplore.ieee.org/document/30966, 1528–1535 (1989).

74. McCulloch, M. A. *et al.* Dependence of noise temperature on physical temperature for cryogenic low-noise amplifiers. *J. of Astronomical Telescopes, Instruments, and Systems* **3.** https://doi.org/10.1117/1.JATIS.3.1.014003, 1–4 (2017).

75. Bautista, J. & Long, E. *Physical Temperature of the Active Region in Cryogenically Cooled Indium Phosphide High-Electron Mobility Transistors* in *IPN Progress Report* **42-170.** https://tmo.jpl.nasa.gov/progress_report/42-170/170D.pdf (2007).

76. Pospieszalski, M. W. *On the limits of noise performance of field effect transistors* in *2017 IEEE MTT-S International Microwave Symposium (IMS)* https://ieeexplore.ieee.org/abstract/document/8059045 (IEEE, 2017), 1953–1956.

77. Weinreb, S. Low-Noise Cooled GASFET Amplifiers. *IEEE Transactions on Microwave Theory and Techniques* **28.** https://ieeexplore.ieee.org/document/1130223, 1041–1054 (1980).

78. Mittereder, J. A., Roussos, J. A., Anderson, W. T. & Ioannou, D. E. Quantitative measurement of channel temperature of GaAs devices for reliable life-time prediction. *IEEE Transactions on Reliability* **51.** https://ieeexplore.ieee.org/stamp/stamp.jsp?tp=&arnumber=1044347, 482–485 (2002).

79. Farzaneh, M. *et al.* CCD-based thermoreflectance microscopy: principles and applications. *J. Phys. D: Appl. Phys* **42.** https://doi.org/10.1088/0022-3727/42/14/143001, 143001 (June 2009).

80. Kuball, M. *et al.* Measurement of temperature distribution in multifinger AlGaN/GaN heterostructure field-effect transistors using micro-Raman spectroscopy. *Applied Physics Letters* **82.** https://doi.org/10.1063/1.1534935, 124–126. eprint: https://doi.org/10.1063/1.1534935 (2003).

81. Choi, S., Heller, E. R., Dorsey, D., Vetury, R. & Graham, S. Thermometry of AlGaN/GaN HEMTs Using Multispectral Raman Features. *IEEE Transactions on Electron Devices* **60.** https://ieeexplore.ieee.org/document/6507260, 1898–1904 (2013).

82. Beechem, T., Graham, S., Kearney, S. P., Phinney, L. M. & Serrano, J. R. Invited Article: Simultaneous mapping of temperature and stress in microdevices using micro-Raman spectroscopy. *Review of Scientific Instruments* **78.** https://doi.org/10.1063/1.2738946, 061301. eprint: https://doi.org/10.1063/1.2738946 (2007).

83. Jeong Park, Moo Whan Shin & Lee, C. C. Thermal modeling and measurement of GaN-based HFET devices. *IEEE Electron Device Letters* **24.** https://ieeexplore.ieee.org/document/1217285, 424–426 (2003).

84. Ziman, J. *Electrons and Phonons: The Theory of Transport Phenomena in Solids* (Oxford University Press, Oxford, 1960).

85. Ferry, D. *Semiconductor Transport* (CRC Press, London, 2000).

86. Lundstrom, M. *Fundamentals of Carrier Transport* (Cambridge University Press, Cambridge, 2000).

87. Conwell, E. *High Field Transport in Semiconductors* (Academic Press, 1967).

88. Liao, B., Zhou, J., Qiu, B., Dresselhaus, M. S. & Chen, G. Ab initio study of electron-phonon interaction in phosphorene. *Phys. Rev. B* **91.** https://link.aps.org/doi/10.1103/PhysRevB.91.235419, 235419 (23 June 2015).

89. Bernardi, M., Vigil-Fowler, D., Lischner, J., Neaton, J. B. & Louie, S. G. Ab Initio Study of Hot Carriers in the First Picosecond after Sunlight Absorption in Silicon. *Phys. Rev. Lett.* **112.** https://link.aps.org/doi/10.1103/PhysRevLett.112.257402, 257402 (25 June 2014).

90. Poncé, S., Margine, E. R. & Giustino, F. Towards predictive many-body calculations of phonon-limited carrier mobilities in semiconductors. *Phys. Rev. B* **97.** https://link.aps.org/doi/10.1103/PhysRevB.97.121201, 121201 (12 Mar. 2018).

91. Fiorentini, M. & Bonini, N. Thermoelectric coefficients of *n*-doped silicon from first principles via the solution of the Boltzmann transport equation. *Phys. Rev. B* **94.** https://link.aps.org/doi/10.1103/PhysRevB.94.085204, 085204 (8 Aug. 2016).

92. Zhou, J.-J. & Bernardi, M. Ab initio electron mobility and polar phonon scattering in GaAs. *Phys. Rev. B* **94.** https://link.aps.org/doi/10.1103/PhysRevB.94.201201, 201201 (20 Nov. 2016).

93. Lee, N., Zhou, J., Chen, H. & Bernardi, M. Ab initio electron-two-phonon scattering in GaAs from next-to-leading order perturbation theory. *Nat Commun* **11.** https://www.nature.com/articles/s41467-020-15339-0 (2020).

94. Jhalani, V., Zhou, J. & Bernardi, M. Ultrafast hot carrier dynamics in GaN and its impact on the efficiency droop. *Nano Letters* **17.** https://pubs.acs.org/doi/abs/10.1021/acs.nanolett.7b02212 (2017).

95. Ma, J., Nissimagoudar, A. S. & Li, W. First-principles study of electron and hole mobilities of Si and GaAs. *Phys. Rev. B* **97.** https://link.aps.org/doi/10.1103/PhysRevB.97.045201, 045201 (4 Jan. 2018).

96. Sun, J., Shi, H., Siegrist, T. & Singh, D. J. Electronic, transport, and optical properties of bulk and mono-layer PdSe2. *Applied Physics Letters* **107.** https://doi.org/10.1063/1.4933302, 153902 (2015).

97. Liu, T.-H. *et al.* Simultaneously high electron and hole mobilities in cubic boron-V compounds: BP, BAs, and BSb. *Phys. Rev. B* **98,** 081203. https://link.aps.org/doi/10.1103/PhysRevB.98.081203 (8 Aug. 2018).

98. Bareikis, V. & Katilius, R. *Noise in Physical Systems and 1/f Fluctuations* https://www.worldscientific.com/doi/abs/10.1142/2764 (WORLD SCIENTIFIC, 1995).

99. Bryerton, E. W., Morgan, M. & Pospieszalski, M. W. *Ultra low noise cryogenic amplifiers for radio astronomy* in *2013 IEEE Radio and Wireless Symposium* https://ieeexplore.ieee.org/document/6486740 (IEEE, 2013), 358–360.

100. Callen, H. B. & Greene, R. F. On a Theorem of Irreversible Thermodynamics. *Phys. Rev.* **86.** https://link.aps.org/doi/10.1103/PhysRev.86.702, 702–710 (5 June 1952).

101. Dörfel, G. The early history of thermal noise: The long way to paradigm change. *Annalen der Physik* **524,** 117–121 (2012).

102. Leontovich, M. Fundamental equations of the kinetic theory of gases from the point of view of the theory of random processes. *Zh. Eksp. Teor. Fiz (JETP)* **5** (1935).

103. Wannier, G. H. Motion of Gaseous Ions in a Strong Electric Field. II. *Phys. Rev.* **87.** https://link.aps.org/doi/10.1103/PhysRev.87.795, 795–798 (5 Sept. 1952).

104. Hashitsume, N. Statistical theory of nonlinear dissipative systems. *Progress of Theoretical Physics* **15.** https://academic.oup.com/ptp/article/8/4/461/1857479 (1956).

105. Kadomotsev, B. Fundamental equations of the kinetic theory of gases from the point of view of the theory of random processes. *Sov. Phys. JETP* **5** (1957).

106. Lax, M. Fluctuations from the Nonequilibrium Steady State. *Rev. Mod. Phys.* **32.** https://link.aps.org/doi/10.1103/RevModPhys.32.25, 25–64 (1 Jan. 1960).

107. Gantsevich, S., Gurevich, V. & Katilius, R. Fluctuations in semiconductors in a strong electric field and the scattering of light by "hot" electrons. *Sov. Phys. JETP* **22.** http://www.jetp.ac.ru/cgi-bin/e/index/e/30/2/p276?a=list (1970).

108. Kogan, S. & Shul'man, A. Theory of Fluctuations in a Nonequilibrium Electron Gas. *Sov. Phys. JETP* **29** (1969).

109. Lax, M. Quantum Noise. IV. Quantum Theory of Noise Sources. *Phys. Rev.* **145.** https://link.aps.org/doi/10.1103/PhysRev.145.110, 110–129 (1 May 1966).

110. Van Vliet, K. & Fasset, J. in *Fluctuation Phenomena in Solids* (ed Burgess, R.) chap. 7 (Academic, New York, 1965).

111. Kogan, S. & Shul'man, A. Extraneous random forces and equations for correlation functions in the theory of nonequilibrium fluctuations. *Sov. Phys. Solid State* **12,** 467 (1970).

112. Jacoboni, C. & Reggiani, L. The Monte Carlo method for the solution of charge transport in semiconductors with applications to covalent materials. *Rev. Mod. Phys.* **55.** https://link.aps.org/doi/10.1103/RevModPhys.55.645, 645–705 (3 July 1983).

113. Reggiani, L., Starikov, E., Shiktorov, P., Gruzinskis, V. & Varani, L. Modelling of small-signal response and electronic noise in semiconductor high-field transport. *Semicond. Sci. Technol.* **12.** https://iopscience.iop.org/article/10.1088/0268-1242/12/2/001, 141–156. ISSN: 0268-1242. (2020) (Feb. 1997).

114. Stanton, C. J. & Wilkins, J. W. Nonequilibrium current fluctuations in semiconductors: A Boltzmann-equation–Green-function approach. *Phys. Rev. B* **35.** https://link.aps.org/doi/10.1103/PhysRevB.35.9722, 9722–9734 (18 June 1987).

115. Stanton, C. J. & Wilkins, J. W. Hot-electron noise in two-valley semiconductors: An analytic model. *Phys. Rev. B* **36.** https://link.aps.org/doi/10.1103/PhysRevB.36.1686, 1686–1695 (3 July 1987).

116. Gherardi, L., Pellacani, A. & Jacoboni, C. Velocity autocorrelation and low temperature mobility of electrons in silicon. *Lett. Nuovo Cimento* **14,** 225–232 (1975).

117. Fauquembergue, R., Zimmermann, J., Kaszynski, A., Constant, E. & Microondes, G. Diffusion and the power spectral density and correlation function of velocity fluctuation for electrons in Si and GaAs by Monte Carlo methods. *Journal of Applied Physics* **51.** https://doi.org/10.1063/1.327713, 1065–1071 (1980).

118. Ferry, D. K. & Barker, J. R. Generalized diffusion, mobility, and the velocity autocorrelation function for high-field transport in semiconductors. *Journal of Applied Physics* **52.** https://doi.org/10.1063/1.328421, 818–824 (1981).

119. Kuhn, T., Reggiani, L., Varani, L. & Mitin, V. Monte Carlo method for the simulation of electronic noise in semiconductors. *Phys. Rev. B* **42.** https://link.aps.org/doi/10.1103/PhysRevB.42.5702, 5702–5713 (9 Sept. 1990).

120. Varani, L., Reggiani, L., Kuhn, T., Gonzalez, T. & Pardo, D. Microscopic simulation of electronic noise in semiconductor materials and devices. *IEEE Transactions on Electron Devices* **41.** https://ieeexplore.ieee.org/document/333807, 1916–1925 (1994).

121. Fawcett, W. & Rees, H. Calculation of the hot electron diffusion rate for GaAs. *Physics Letters A* **29.** http://www.sciencedirect.com/science/article/pii/0375960169911037, 578–579. ISSN: 0375-9601 (1969).

122. Bosi, S. & Jacoboni, C. Monte Carlo high-field transport in degenerate GaAs. *J. Phys. C: Solid State Phys.* **9.** https://iopscience.iop.org/article/10.1088/0022-3719/9/2/017/pdf, 315–319 (Jan. 1976).

123. Hill, G., Robson, P. N. & Fawcett, W. Diffusion and the power spectral density of velocity fluctuations for electrons in InP by Monte Carlo methods. *Journal of Applied Physics* **50.** https://doi.org/10.1063/1.325670, 356–360 (1979).

124. Wang, S., Liu, H., Gao, B. & Cai, H. Monte Carlo calculation of electron diffusion coefficient in wurtzite indium nitride. *Applied Physics Letters* **100.** https://doi.org/10.1063/1.3700720, 142105 (2012).

125. Starikov, E. *et al.* Monte Carlo calculations of hot-electron transport and diffusion noise in GaN and InN. *Semicond. Sci. Technol.* **20.** https://iopscience.iop.org/article/10.1088/0268-1242/20/3/004, 279–285 (Feb. 2005).

126. Rengel, R. & Martín, M. J. Diffusion coefficient, correlation function, and power spectral density of velocity fluctuations in monolayer graphene. *Journal of Applied Physics* **114.** https://doi.org/10.1063/1.4824182, 143702 (2013).

127. Xing, D. Y., Liu, M., Hu, P. & Ting, C. S. Diffusion of hot carriers in two-valley semiconductors. *J. Phys. C: Solid State Phys.* **21.** https://iopscience.iop.org/article/10.1088/0022-3719/21/15/020, 2881–2898 (May 1988).

128. Xing, D. Y., Liu, M. & Ting, C. S. Analytical approach to diffusion of hot carriers in n-type GaAs with Γ-L-X band structure. *Phys. Rev. B* **37.** https://link.aps.org/doi/10.1103/PhysRevB.37.10283, 10283–10294 (17 June 1988).

129. Iñiguez–de-la-Torre, I., Mateos, J., Pardo, D. & González, T. Monte Carlo analysis of noise spectra in self-switching nanodiodes. *Journal of Applied Physics* **103.** https://doi.org/10.1063/1.2832505, 024502 (2008).

130. Rodilla, H., González, T., Pardo, D. & Mateos, J. High-mobility heterostructures based on InAs and InSb: A Monte Carlo study. *Journal of Applied Physics* **105.** https://doi.org/10.1063/1.3132863, 113705 (2009).

131. Karishy, S. *et al. Monte Carlo calculation of In0.53Ga0.47As and InAs noise parameters* in *2017 International Conference on Noise and Fluctuations (ICNF)* https://ieeexplore.ieee.org/document/7985941 ('IEEE', 2017), 1–4.

132. Kubo, R., Toda, M. & Hashitsume, N. *Statistical physics II: nonequilibrium statistical mechanics* (Springer, 1998).

133. Liboff, R. L. *Kinetic Theory: Classical, Quantum and Relativistic Descriptions* (Springer, 2011).

134. Mostofi, A. A. *et al.* wannier90: A tool for obtaining maximally-localised Wannier functions. *Computer Physics Communications* **178.** http://www.sciencedirect.com/science/article/pii/S0010465507004936, 685–699. ISSN: 0010-4655 (2008).

135. Pizzi, G. *et al.* Wannier90 as a community code: new features and applications. *J. Phys.: Condens. Matter* **32.** https://doi.org/10.1088/1361-648x/ab51ff, 165902 (Jan. 2020).

136. Fowler, R. *Statistical Mechanics* (Cambridge University Press, London, 1936).

137. Giannozzi, P. *et al.* Advanced capabilities for materials modelling with Quantum ESPRESSO. *J. Phys.: Condens. Matter* **29.** https://iopscience.iop.org/article/10.1088/1361-648X/aa8f79/meta, 465901 (Oct. 2017).

138. Sjakste, J., Vast, N., Calandra, M. & Mauri, F. Wannier interpolation of the electron-phonon matrix elements in polar semiconductors: Polar-optical coupling in GaAs. *Phys. Rev. B* **92.** https://link.aps.org/doi/10.1103/PhysRevB.92.054307, 054307 (5 Aug. 2015).

139. Maliyov, I., Park, J. & Bernardi, M. Ab initio electron dynamics in high electric fields: Accurate prediction of velocity-field curves. *Phys. Rev. B* **104,** L100303. https://link.aps.org/doi/10.1103/PhysRevB.104.L100303 (10 Sept. 2021).

140. Virtanen, P. *et al.* SciPy 1.0: Fundamental Algorithms for Scientific Computing in Python. *Nat Methods* **17.** https://doi.org/10.1038/s41592-019-0686-2, 261–272 (2020).

141. Jhalani, V. A., Zhou, J.-J., Park, J., Dreyer, C. E. & Bernardi, M. Piezoelectric Electron-Phonon Interaction from Ab Initio Dynamical Quadrupoles: Impact on Charge Transport in Wurtzite GaN. *Phys. Rev. Lett.* **125.** https://link.aps.org/doi/10.1103/PhysRevLett.125.136602, 136602 (13 Sept. 2020).

142. Brunin, G. *et al.* Electron-Phonon beyond Fröhlich: Dynamical Quadrupoles in Polar and Covalent Solids. *Phys. Rev. Letters* **125.** https://link.aps.org/doi/10.1103/PhysRevLett.125.136601, 136601 (13 Sept. 2020).

143. Park, J., Zhou, J.-J., Jhalani, V. A., Dreyer, C. E. & Bernardi, M. Long-range quadrupole electron-phonon interaction from first principles. *Phys. Rev. B* **102,** 125203. https://link.aps.org/doi/10.1103/PhysRevB.102.125203 (12 Sept. 2020).

144. Jain, A. *et al.* The Materials Project: A materials genome approach to accelerating materials innovation. *APL Materials* **1,** 011002. ISSN: 2166532X. http://link.aip.org/link/AMPADS/v1/i1/p011002/s1%5C&Agg=doi (2013).

145. Aspnes, D. E., Olson, C. G. & Lynch, D. W. Ordering and Absolute Energies of the ${L_6}^c$ and ${X_6}^c$ Conduction Band Minima in GaAs. *Phys. Rev. Lett.* **37,** 766–769. https://link.aps.org/doi/10.1103/PhysRevLett.37.766 (12 Sept. 1976).

146. Bareikis, V. *et al. Velocity Overshoot and Suppression of Diffusivity and Microwave Noise in Short n+-n-n+ Structures of GaAs* in *High-Speed Electronics* (eds Källbäck, B. & Beneking, H.) https://link.springer.com/chapter/10.1007/978-3-642-82979-6_5 (Springer Berlin Heidelberg, Berlin, Heidelberg, 1986), 28–31. ISBN: 978-3-642-82979-6.

147. Ruch, J. G. & Kino, G. S. Transport Properties of GaAs. *Phys. Rev.* **174.** https://link.aps.org/doi/10.1103/PhysRev.174.921, 921–931 (3 Oct. 1968).

148. Teitel, S. & Wilkins, J. W. Small-signal ac conductivity and velocity overshoot in semiconductor materials. *Journal of Applied Physics* **53.** https://doi.org/10.1063/1.331376, 5006–5012 (1982).

149. Bareikis, V., Liberis, J., Matulioniene, I., Matulionis, A. & Sakalas, P. Experiments on hot electron noise in semiconductor materials for high-speed devices. *IEEE Transactions on Electron Devices* **41.** https://ieeexplore.ieee.org/document/333822, 2050–2060 (1994).

150. Bareikis, V., Viktoravicius, V., Galdikas, A. & Miliusyte, R. Microwave Noise and Constant of the Coupling Between the Valleys Gamma and L in a Three-Valley Model of GaAs. *Sov. Phys.-Semiconductors* **14,** 847–849 (1980).

151. Conwell, E. M. & Vassell, M. O. High-Field Transport in- Type GaAs. *Phys. Rev.* **166.** https://link.aps.org/doi/10.1103/{PhysRev}.166.797, 797–821. ISSN: 0031-899X (Feb. 1968).

152. Davydov, B. On the theory of electron motion in gases and semiconductors. *Zh. Eksp. Teor. Fiz.* **8,** 1069 (7 1937).

153. Uribe, F. J. & Velasco, R. M. Einstein Relation for Electrons in an Electric Field. *J Stat Phys* **162,** 242–266 (2015).

154. Skullerud, H. R. Longitudinal diffusion of electrons in electrostatic fields in gases. *J. Phys. B: Atom. Mol. Phys.* **2.** https://iopscience.iop.org/article/10.1088/0022-3700/2/6/309, 696–705 (June 1969).

155. Gurevich, V. & Katilius, R. Contribution to the Theory of Hot Electrons in an Anisotropic Semiconductor. *Sov. Phys. JETP* **22.** http://www.jetp.ac.ru/cgi-bin/e/index/e/22/4/p796?a=list, 796 (Apr. 1966).

156. Schlup, W. Definition of noise temperatures θ in three dimensions and the conjecture $\theta \geq T$ in nonequilibrium systems. *Physica* **69,** 485–498. ISSN: 0031-8914 (1973).

157. Aninkevičius, V., Bareikis, V., Liberis, J., Matulionis, A. & Sakalas, P. Comparative analysis of microwave noise in GaAs and AlGaAs/GaAs channels. *Solid-State Electronics* **36,** 1339–1343. ISSN: 0038-1101 (1993).

158. Chaput, L. Direct Solution to the Linearized Phonon Boltzmann Equation. *Phys. Rev. Lett.* **110.** https://link.aps.org/doi/10.1103/PhysRevLett.110.265506, 265506 (26 June 2013).

159. Rabinovich, R. On galvanomagnetic phenomena under hot-electron energy scattering on optical phonons. *Sov. Phys. - Semiconductors* **3,** 839 (1969).

160. Shibuya, M. Hot Electron Problem in Semiconductors with Spheroidal Energy Surfaces. *Phys. Rev.* **99,** 1189–1191. https://link.aps.org/doi/10.1103/PhysRev.99.1189 (4 Aug. 1955).

161. Canali, C., Ottaviani, G. & Alberigi Quaranta, A. Drift velocity of electrons and holes and associated anisotropic effects in silicon. *Journal of Physics and Chemistry of Solids* **32,** 1707–1720. ISSN: 0022-3697. https://www.sciencedirect.com/science/article/pii/S0022369771801373 (1971).

162. Schmidt-Tiedemann, K. J. Symmetry Properties of Warm Electron Effects in Cubic Semiconductors. *Phys. Rev.* **123,** 1999–2000. https://link.aps.org/doi/10.1103/PhysRev.123.1999 (6 Sept. 1961).

163. Schmidt-Tiedemann, K. J. Tensor Theory of the Conductivity of Warm Electrons in Cubic Semiconductors. *Philips Research Reports* **18,** 338–360 (Feb. 1963).

164. Gibbs, W. Conductivity anisotropy and hot electron temperature in silicon. *Journal of Physics and Chemistry of Solids* **25,** 247–251. ISSN: 0022-3697. https://www.sciencedirect.com/science/article/pii/002236976490085X (1964).

165. Sasaki, W., Shibuya, M. & Mizuguchi, K. Anisotropy of Hot Electrons in n-type Germanium. *J. Phys. Soc. Jpn.* **13,** 456–460. eprint: https://doi.org/10.1143/JPSJ.13.456. https://doi.org/10.1143/JPSJ.13.456 (1958).

166. Hamaguchi, C. & Inuishi, Y. Conductivity anisotropy of hot electrons in n-type silicon heated by microwave fields. *Journal of Physics and Chemistry of Solids* **27,** 1511–1518. ISSN: 0022-3697. https://www.sciencedirect.com/science/article/pii/0022369766901466 (1966).

167. Brunetti, R. *et al.* Diffusion coefficient of electrons in silicon. *Journal of Applied Physics* **52,** 6713–6722. eprint: https://doi.org/10.1063/1.328622. https://doi.org/10.1063/1.328622 (1981).

168. Liu, C. *et al.* Characteristics of electric quadrupole and magnetic quadrupole coupling in a symmetric silicon structure. **22,** 023018. https://doi.org/10.1088/1367-2630/ab6cde (Feb. 2020).

169. Basu, P. K. & Nag, B. R. Infrared Free-Carrier Absorption in n-Type Silicon. *Phys. Stat. Sol. (b)* **53,** K61–K64. eprint: https://onlinelibrary.wiley.com/doi/pdf/10.1002/pssb.2220530158. https://onlinelibrary.wiley.com/doi/abs/10.1002/pssb.2220530158 (1972).

170. Kubakaddi, S. S. & Krishnamurthy, B. S. Infrared Free-Carrier Absorption in non-polar semiconductor; scattering by two-short wavelength phonons. *Indian Journal of Physics A* **53,** 127–135 (1979).

171. Renucci, J. B., Tyte, R. N. & Cardona, M. Resonant Raman scattering in silicon. *Phys. Rev. B* **11,** 3885–3895. https://link.aps.org/doi/10.1103/PhysRevB.11.3885 (10 May 1975).

172. Temple, P. A. & Hathaway, C. E. Multiphonon Raman Spectrum of Silicon. *Phys. Rev. B* **7,** 3685–3697. https://link.aps.org/doi/10.1103/PhysRevB.7.3685 (8 Apr. 1973).

173. Hamaguchi, C. & Mori, N. Magnetophonon resonance in semiconductors. *Physica B: Condensed Matter* **164,** 85–96. ISSN: 0921-4526. https://www.sciencedirect.com/science/article/pii/0921452690900653 (1990).

174. Kubakaddi, S. S. & Krishnamurthy, B. S. The Electron-Two Short-Wavelength Phonon Scattering in Non-Polar Semiconductors. *Phys. Stat. Sol. (b)* **80,** 603–609 (1977).

175. Alldredge, G. P. & Blatt, F. On the role of two-phonon processes in the energy relaxation of a heated-electron distribution. *Annals of Physics* **45,** 191–231. ISSN: 0003-4916. https://www.sciencedirect.com/science/article/pii/0003491667901236 (1967).

176. Costato, M., Fontanesi, S. & Reggiani, L. Competitive rate of energy loss mechanisms evidenced in high-field electron drift velocity in Si at 30 °K. *Lett. Nuovo Cimento* **1,** 946–951 (1969).

177. Fischetti, M. V., Yoder, P. D., Khatami, M. M., Gaddemane, G. & Van de Put, M. L. "Hot electrons in Si lose energy mostly to optical phonons": Truth or myth? *Applied Physics Letters* **114,** 222104. eprint: https://doi.org/10.1063/1.5099914. https://doi.org/10.1063/1.5099914 (2019).

178. Rodilla, H. *et al.* Cryogenic Performance of Low-Noise InP HEMTs: A Monte Carlo Study. *IEEE Transactions on Electron Devices* **60.** https://ieeexplore.ieee.org/document/6497570, 1625–1631 (2013).

179. Bautista, J. *et al. Cryogenic, X-band and Ka-band InP HEMT based LNAs for the Deep Space Network* in *2001 IEEE Aerospace Conference Proceedings (Cat. No.01TH8542)* **2.** https://ieeexplore.ieee.org/document/931264 (IEEE, 2001), 2/829–2/842 vol.2.

180. Swartz, E. T. & Pohl, R. O. Thermal boundary resistance. *Rev. Mod. Phys.* **61.** https://link.aps.org/doi/10.1103/RevModPhys.61.605, 605–668 (3 July 1989).

181. Takacs, D. & Trager, J. *Temperature Increase by Self-Heating in VLSI CMOS* in *ESSDERC '87: 17th European Solid State Device Research Conference* https://ieeexplore.ieee.org/abstract/document/5436746/ (IEEE, 1987), 729–732.

182. Sesnic, S. S. & Craig, G. R. Thermal effects in JFET and MOSFET devices at cryogenic temperatures. *IEEE Transactions on Electron Devices* **19.** https://ieeexplore.ieee.org/document/1476993, 933–942 (1972).

183. Foty, D. P. & Titcomb, S. L. Thermal effects in n-channel enhancement MOSFETs operated at cryogenic temperatures. *IEEE Transactions on Electron Devices* **34.** https://ieeexplore.ieee.org/document/1486603, 107–113 (1987).

184. Foty, D. Thermal effects in p-channel MOSFETs at low temperatures. *IEEE Transactions on Electron Devices* **36.** https://ieeexplore.ieee.org/document/30968, 1542–1544 (1989).

185. Tenbroek, B. M., Lee, M. S. L., Redman-White, W., Bunyan, J. T. & Uren, M. J. Self-heating effects in SOI MOSFETs and their measurement by small signal conductance techniques. *IEEE Transactions on Electron Devices* **43.** https://ieeexplore.ieee.org/document/544417, 2240–2248 (1996).

186. Triantopoulos, K. *et al.* Self-Heating Effect in FDSOI Transistors Down to Cryogenic Operation at 4.2 K. *IEEE Transactions on Electron Devices* **66.** https://ieeexplore.ieee.org/document/8741185, 3498–3505 (2019).

187. Garcıa-Sánchez, S. *et al.* Non-linear thermal resistance model for the simulation of high power GaN-based devices. *Semicond. Sci. Technol.* **36.** https://iopscience.iop.org/article/10.1088/1361-6641/abeb83, 055002. https://doi.org/10.1088/1361-6641/abeb83 (Mar. 2021).

188. Darwish, A. M., Bayba, A. J. & Hung, H. A. Utilizing Diode Characteristics for GaN HEMT Channel Temperature Prediction. *IEEE Transactions on Microwave Theory and Techniques* **56.** https://ieeexplore.ieee.org/abstract/document/4682665, 3188–3192 (2008).

189. Wu, M. *et al.* Accurate Measurement of Channel Temperature for AlGaN/GaN HEMTs. *IEEE Transactions on Electron Devices* **65.** https://ieeexplore.ieee.org/document/8466809, 4792–4799 (2018).

190. Mottet, B. *Zuverlässigkeitsstudien an Höchstfrequenzbauelementen mit gepulsten Techniken (TLP-Methode)* PhD thesis (Technische Universität, 2005).

191. Norde, H. A modified forward I-V plot for Schottky diodes with high series resistance. *Journal of Applied Physics* **50.** https://doi.org/10.1063/1.325607, 5052–5053. eprint: https://doi.org/10.1063/1.325607 (1979).

192. Aazou, S. & Assaid, E. M. *Schottky diode parameters extraction using two different methods* in *2009 International Conference on Microelectronics - ICM* (2009), 240–243.

193. Cheung, S. K. & Cheung, N. W. Extraction of Schottky diode parameters from forward current-voltage characteristics. *Applied Physics Letters* **49.** https://doi.org/10.1063/1.97359, 85–87. eprint: https://doi.org/10.1063/1.97359 (1986).

194. Kiuru, T., Mallat, J., Raisanen, A. V. & Narhi, T. Schottky Diode Series Resistance and Thermal Resistance Extraction From *S* -Parameter and Temperature Controlled I–V Measurements. *IEEE Transactions on Microwave Theory and Techniques* **59.** https://ieeexplore.ieee.org/document/5773463, 2108–2116 (2011).

195. Crowell, C. & Rideout, V. Normalized thermionic-field (T-F) emission in metal-semiconductor (Schottky) barriers. *Solid-State Electronics* **12,** 89–105. ISSN: 0038-1101. https://www.sciencedirect.com/science/article/pii/0038110169901178 (1969).

196. Padovani, F. & Stratton, R. Field and thermionic-field emission in Schottky barriers. *Solid-State Electronics* **9,** 695–707. ISSN: 0038-1101. https://www.sciencedirect.com/science/article/pii/0038110166900979 (1966).

197. Sze, S. & Ng, K. *Physics of Semiconductor Devices"* (John Wiley and Sons, Hoboken, NJ, 2006).

198. Akgiray, A. *New Technologies Driving Decade-Bandwidth Radio Astronomy: Quad-Ridged Flared Horn and Compound-Semiconductor LNAs* PhD thesis (California Institute of Technology, Pasadena, CA, 2013).

199. Russell, D., Cleary, K. & Reeves, R. Cryogenic probe station for on-wafer characterization of electrical devices. *Review of Scientific Instruments* **83.** https://doi.org/10.1063/1.3700213, 044703. eprint: https://doi.org/10.1063/1.3700213 (2012).

200. Cibils, R. M. & Buitrago, R. H. Forward I-V plot for nonideal Schottky diodes with high series resistance. *Journal of Applied Physics* **58.** https://doi.org/10.1063/1.336222, 1075–1077. eprint: https://doi.org/10.1063/1.336222 (1985).

201. Van der Rotten, R. B. A. *A limited memory Broyden method to solve high-dimensional systems of nonlinear equations.* PhD thesis (Universiteit Leiden, 2003).

202. Blakemore, J. S. Semiconducting and other major properties of Gallium Arsenide. *Journal of Applied Physics* **53.** https://doi.org/10.1063/1.331665, R123–R181. eprint: https://doi.org/10.1063/1.331665 (1982).

203. Stoner, R. J. & Maris, H. J. Kapitza conductance and heat flow between solids at temperatures from 50 to 300 K. *Phys. Rev. B* **48.** https://link.aps.org/doi/10.1103/PhysRevB.48.16373, 16373–16387 (22 Dec. 1993).

204. Cha, E. *InP High Electron Mobility Transistors for Cryogenic Low-Noise and Low-Power Amplifiers.* PhD thesis (Chalmers University of Technology, Gothenburg, Sweden, 2020).

205. Hopkins, P. Thermal Transport across Solid Interfaces with Nanoscale Imperfections: Effects of Roughness, Disorder, Dislocations, and Bonding on Thermal Boundary Conductance. *International Scholarly Research Notices* **2013.** https://www.hindawi.com/journals/isrn/2013/682586/ (2013).

206. Swartz, E. T. & Pohl, R. O. Thermal boundary resistance. *Rev. Mod. Phys.* **61.** https://link.aps.org/doi/10.1103/RevModPhys.61.605, 605–668 (3 July 1989).

207. Little, W. A. The Transport of Heat between Dissimilar Solids at Low Temperatures. *Canadian Journal of Physics* **37,** 334–349. eprint: https://doi.org/10.1139/p59-037. https://doi.org/10.1139/p59-037 (1959).

208. Lienhard IV, J. H. & Lienhard V, J. H. *A Heat Transfer Textbook* 5th, 72. 784 pp. ISBN: 9780486837352. http://ahtt.mit.edu (Dover Publications, Mineola, NY, Dec. 2019).

209. Mills, A. *Heat Transfer* ISBN: 9780256076424 (Irwin, 1992).

210. Van Sciver, W. *Helium cryogenics* (Springer New York, 2012).

211. Lu, I.-T., Zhou, J.-J. & Bernardi, M. Efficient ab initio calculations of electron-defect scattering and defect-limited carrier mobility. *Phys. Rev. Materials* **3,** 033804. https://link.aps.org/doi/10.1103/PhysRevMaterials.3.033804 (3 Mar. 2019).

212. Lu, I.-T., Zhou, J.-J., Park, J. & Bernardi, M. *First-principles ionized-impurity scattering and charge transport in doped materials* 2021. arXiv: 2110.04920 [cond-mat.mtrl-sci].

213. Shah, J. Hot electrons and phonons under high intensity photoexcitation of semiconductors. *Solid-State Electronics* **21,** 43–50. ISSN: 0038-1101. https://www.sciencedirect.com/science/article/pii/0038110178901132 (1978).

214. Shah, J. Hot carriers in quasi-2-D polar semiconductors. *IEEE Journal of Quantum Electronics* **22,** 1728–1743 (1986).

215. Sadasivam, S., Chan, M. K. Y. & Darancet, P. Theory of Thermal Relaxation of Electrons in Semiconductors. *Phys. Rev. Lett.* **119,** 136602. https://link.aps.org/doi/10.1103/PhysRevLett.119.136602 (13 Sept. 2017).

216. Protik, N. H., Li, C., Pruneda, M., Broido, D. & Ordejón, P. *Elphbolt: An ab initio solver for the coupled electron-phonon Boltzmann transport equations* 2021. arXiv: 2109.08547 [cond-mat.mtrl-sci].

217. Deacon, R. S., Chuang, K.-C., Nicholas, R. J., Novoselov, K. S. & Geim, A. K. Cyclotron resonance study of the electron and hole velocity in graphene monolayers. *Phys. Rev. B* **76,** 081406. https://link.aps.org/doi/10.1103/PhysRevB.76.081406 (8 Aug. 2007).

218. Chauhan, J. & Guo, J. High-field transport and velocity saturation in graphene. *Applied Physics Letters* **95,** 023120. eprint: https://doi.org/10.1063/1.3182740. https://doi.org/10.1063/1.3182740 (2009).

219. Rustagi, A. & Stanton, C. J. Hot-electron noise properties of graphene-like systems. *Phys. Rev. B* **90,** 245424. https://link.aps.org/doi/10.1103/PhysRevB.90.245424 (24 Dec. 2014).

220. Tong, X. & Bernardi, M. Toward precise simulations of the coupled ultrafast dynamics of electrons and atomic vibrations in materials. *Phys. Rev. Research* **3.** ISSN: 2643-1564. http://dx.doi.org/10.1103/PhysRevResearch.3.023072 (Apr. 2021).